

2022

# Non-stationarity in extratropical north pacific atmospheric forcing of ENSO and its oscillatory behavior

---

<https://hdl.handle.net/2144/45525>

*Boston University*

BOSTON UNIVERSITY  
GRADUATE SCHOOL OF ARTS AND SCIENCES

Dissertation

**NON-STATIONARITY IN EXTRATROPICAL NORTH PACIFIC  
ATMOSPHERIC FORCING OF ENSO AND ITS OSCILLATORY BEHAVIOR**

by

**VALENTINA PIVOTTI**

B.A., Università degli studi di Padova, 2011  
M.A., Lund University, 2017

Submitted in partial fulfillment of the  
requirements for the degree of  
Doctor of Philosophy

2022



Approved by

First Reader

---

Bruce T. Anderson, Ph.D.  
Professor of Earth and Environment

Second Reader

---

Annalisa Cherchi, Ph.D.  
Senior scientist  
ISAC-CNR

Third Reader

---

Guido Salvucci, Ph.D.  
Professor of Earth and Environment

Fourth Reader

---

Sarah Larson, Ph.D.  
Associate Professor of Marine, Earth and Atmospheric Sciences  
North Carolina State University

## **DEDICATION**

To the loving memory of Marcella Cargnelutti, my grandma.

“La smetterai ben di studiare prima o poi...”

## ACKNOWLEDGMENTS

It is hard to put down in words how grateful I am to all the amazing people that have walked portions of this path with me, but I will give it my best try.

First, I want to thank Professor Bruce Anderson for believing in me from the beginning. You read the application of a mathematician who wished to become an environmental scientist and you helped make it happen. You guided me through these years, often by distance before it was mainstream, allowing me to make my mistakes, there to help me when I got lost in them.

Thank you to my fellow students at BU, Luca, Sam, Ana, Sarah, Anthony, Linda, Drew, Erin, Claudia, Betsy, Chris, Alia, you are all awesome. You made me feel at home in a new city and a new country, I am forever grateful for the memories I had the privilege of creating with you, and forever regretful the time we spent together was so short. At E&E, I want to thank Professors Anne Short, Diane Thompson and Sucharita Gopal for their willingness and enthusiasm to discuss concepts and ideas with me when I was still landing in this new field, and the late Professor Tony Janetos for the inspiring conversations and for the care he showed us all. Finally, my PhD would not have been possible without the constant assistance of the administrative staff that had to put up with my endless complications, thank you (and I'm sorry) Matt Dicintio and Alissa Beideck Landry.

During my second year, I had the opportunity to be a guest at the Euro-Mediterranean Center for Climate Change in Bologna under the guidance of Annalisa Cherchi and Alessio Bellucci. Thank you for the opportunity and for everything you taught me. I also

want to thank the entire CMCC team for welcoming me, and special thanks go to Daniele and Marianna, the best office mates I could have wished for.

And now, on a more personal note, I want to acknowledge my amazing mother, Laura, who taught me early on the value of knowledge and hard work. None of this would have happened without your daily encouragement and example, “Mi raccomando, attenta e concentrata”, yes mum! And with her, I want to express my deepest love and gratitude to the entire Pivotti clan, my roots and strength, vi voglio bene. A heartfelt thank you goes to Markus, you pushed me to believe in myself, my path and my dreams, every time I think you have shown me all your support and encouragement, you find new ways to be by my side. Tonia, my beloved, I will not thank you dear because, if anything, you made this harder, I madly love you, but no. There is then the family one choses, and, not to brag, but I have chosen the best people. I want to thank my dearest Sara, our 20 years long friendship is one of the things I am most proud of, thank you for being there, always, and for being you. And thank you to my friends for being the bestest, warmest and funniest people I know. Bea, Gdufr, Enrico, Beatrice, Melody, Luca, Sonia, Nicola, Jerker, Amadio, Zahra, Stefano, Niccolò, Picc, Vittorio, James, I am so privileged to have you all in my life.

**NON-STATIONARITY IN EXTRATROPICAL NORTH PACIFIC  
ATMOSPHERIC FORCING OF ENSO AND ITS OSCILLATORY BEHAVIOR**

**VALENTINA PIVOTTI**

Boston University Graduate School of Arts and Sciences, 2022

Major Professor: Bruce T. Anderson, Professor of Earth and Environment

**ABSTRACT**

As the largest mode of coupled climate variability, the El Niño Southern Oscillation (ENSO) carries consequences for weather patterns worldwide. In turn, communities that live in areas affected by ENSO variability would benefit from reliable and timely information on the occurrence of such events. To address this need, there has been an on-going effort within the scientific community to investigate and characterize the mechanisms that give rise to ENSO events. One of the greatest impediments to this effort, however, is that the ENSO system can behave both as a self-sustained, deterministic oscillation, and as a response to stochastic forcing. In this dissertation, we uncover a key determinant of these two types of ENSO behavior – namely North Pacific Oscillation (NPO)-induced variations in the northeasterly trade winds – and analyze how the variations in these trade winds influence ENSO variability historically and into the future.

The first Chapter of this dissertation provides a thorough review of previous efforts to understand the initiation, onset, and evolution of ENSO events with a particular



focus on the relationship between ENSO events and two NPO-related precursors, namely the Trade Wind Charging and the Northern Pacific Meridional Mode (TWC/NPMM).

In Chapter 2 (Pivotti and Anderson 2021), we study the TWC/NPMM-ENSO relation over 140 years and uncover that there has been a multi-decadal modulation in the strength of TWC/NPMM's influence upon ENSO events. Further, as a consequence of this modulation, ENSO behavior shifted between a stochastically forced interannual mode of variability to a multi-annual, quasi-regular one with a self-sustained oscillation and back again over the course of the last 140 years.

In Chapter 3, we assess how the TWC/NPMM-ENSO relationship is reconstructed in state of the art coupled climate models. We find that across the ensemble the TWC/NPMM is reconstructed by all models as the leading ENSO precursor. Further, a subset of better-performing models confirms that during those periods when the TWC/NPMM-ENSO coupling is weak, ENSO oscillates regularly with constant periodicity, whereas when the coupling is strong, ENSO shows a more stochastic behavior.

In Chapter 4, we introduce experiments with increasing anthropogenic radiative forcings from the same ensemble of coupled climate models evaluated in Chapter 3. We find that ENSO events initiated by TWC/NPMM are consistently stronger than standard ENSO events, independent of the presence/absence of increasing external forcings, however neither TWC/NPMM-induced ENSO events nor standard events show any systematic change in intensity in the presence of increasing atmospheric forcings. Further, there is no systematic change in TWC/NPMM-ENSO coupling in the presence

of increasing external forcing and hence no systematic change in the oscillatory (or stochastic) behavior of the ENSO system.

Finally, Chapter 5 of this dissertation includes a concluding summary and suggestions for future work. In summary, this dissertation shows for the first time that the ENSO system can behave both as a self-sustained oscillation and as a response to stochastic forcing, that the modulation of this behavior is linked to the strength of TWC/NPMM-ENSO coupling, and that the strength of this coupling is the result of multi-decadal internal climate variability and not human-induced climate change.

## TABLE OF CONTENTS

DEDICATION .....	iv
ACKNOWLEDGMENTS .....	v
ABSTRACT .....	vii
TABLE OF CONTENTS.....	x
LIST OF TABLES .....	xii
LIST OF FIGURES .....	xiii
CHAPTER ONE .....	1
Background.....	1
Scientific Questions and Findings .....	7
Data and Methods .....	9
CHAPTER TWO .....	12
Introduction.....	12
Data and Method.....	17
<i>Data</i> .....	17
<i>Method</i> .....	18
Results.....	21
Summary and Conclusion.....	35
CHAPTER THREE .....	40
Introduction.....	40
Data and Method.....	43
<i>Data</i> .....	43

<i>Method</i> .....	46
Results.....	48
Summary and Discussion.....	65
CHAPTER FOUR .....	69
Introduction.....	69
Data and Method.....	70
<i>Data</i> .....	70
<i>Method</i> .....	72
Results.....	74
Summary and Conclusion.....	90
CONCLUSION .....	92
CURRICULUM VITAE.....	105

## LIST OF TABLES

### Chapter 3

Table 1. .... 45

Table 2. .... 57

### Chapter 4

Table 3. .... 72

Table 4. .... 87

## LIST OF FIGURES

Chapter 2		
Figure 1.	.....	22
Figure 2.	.....	24
Figure 3.	.....	25
Figure 4.	.....	27
Figure 5.	.....	28
Figure 6.	.....	29
Figure 7.	.....	31
Figure 8.	.....	32
Figure 9.	.....	33
Figure 10.	.....	34
Chapter 3		
Figure 11.	.....	50
Figure 12.	.....	51
Figure 13.	.....	52
Figure 14.	.....	53
Figure 15.	.....	59
Figure 16.	.....	62
Figure 17.	.....	63
Figure 18.	.....	64
Chapter 4		

Figure 19.	.....	75
Figure 20.	.....	79
Figure 21.	.....	80
Figure 22.	.....	81
Figure 23.	.....	82
Figure 24.	.....	83
Figure 25.	.....	85
Figure 26.	.....	86
Figure 27.	.....	89

## CHAPTER ONE

### Background

The El Niño Southern Oscillation (ENSO) is the largest mode of coupled oceanic-atmospheric variability. Situated in the Tropical Pacific, it is characterized by atmospheric as well as oceanic anomalies that oscillate between two states of opposite sign, called El Niño and La Niña, over a period that varies between 2 and 7 years (Wang, Deser, et al. 2017). The neutral condition of the Tropical Pacific can be described through the features of the Walker circulation: relative warmer water in the western portion of the basin and colder water in the eastern portion sustain a cell of rising air in the west, and respectively subsiding in the east, with easterly winds at the surface and westerlies aloft. Among the consequences of the pressure patterns of the Walker circulation, we see wetter conditions off of the coast of Australia and South-East Asia, and dryer conditions along the western South American coast. Similarly, at the subsurface, downwelling in the western portion of the basin is a consequence of the build-up of warm surface water due to trade wind-induced Ekman transport, while the opposite is true for the upwelling in the East. In the event of a La Niña, we record a strengthening of the Hadley cell, with all the aforementioned features increasing in intensity. In the event of an El Niño, instead, the atmospheric as well as oceanic anomalies have an opposite sign with respect to the neutral state. The sea surface temperature off of the coast of Australia and South East Asia is colder than the mean state, while the opposite is true for the waters in the eastern portion of the basin. These anomalies affect the Walker circulation that weakens while, at depth, the thermocline is less steep than in the neutral state.



Importantly, the different stages of ENSO affect weather patterns, not only in the regions surrounding the Tropical Pacific (Taschetto, et al. 2020), (Cai, et al. 2011), but also over areas outside the tropics at higher latitudes (Liu, et al. 2016), (Alexander, et al. 2002), (Dai and Wigley 2000), and tropical regions beyond the Pacific Ocean (Ummenhofer, et al. 2012), (Ashok, et al. 2004). These climatic impacts - including more abundant precipitation, extended dry spells, changes in temperature, as well as more extreme hazards like floods and wildfires - vary in intensity according to the sign, the size and the location of the ENSO event that is causing them. For instance, El Niño and La Niña events have opposite effects on the precipitation patterns over the western coast of South America causing an increase or a reduction in precipitation respectively (Taschetto, et al. 2020). Similarly, the intensity of a specific ENSO event, particularly in the case of what is called an “extreme ENSO”, dictates the magnitude of its global impacts (Santoso, Mcphaden and Cai 2017). Further, the longitudinal location of the sea surface temperature (SST) anomalies, particularly in the case of El Niño, where the different types of El Niño have been named Eastern Pacific (EP) or Central Pacific (CP) El Niño, has also been shown to affect the teleconnections and thus the subsequent weather patterns (Feng, Chen and Li 2017). Due to all of these reasons, communities that live in areas affected by ENSO variability see their safety and livelihoods at risk and would benefit from reliable and timely information on the occurrence of such events. If provided with such knowledge, communities and stakeholders would be able to prepare themselves in due time and plan resilience efforts to better handle the climatic consequences of

ENSO events. Indeed, one of the on-going efforts of the scientific community has been to investigate and characterize the mechanisms that precede and are responsible for the initiation of ENSO events (Amaya 2019), (Anderson 2003) and (Wang 2001). The better we reconstruct what drives ENSO events, the better we might be able to monitor their development and thus share this knowledge with those that might benefit from it.

One of the greatest impediments to this effort, however, is that the ENSO system can behave both as a self-sustained, deterministic oscillation, and as a response to stochastic forcing (Kirtman and Schopf 1998; Wang, Deser, et al. 2017). For instance, because of positive feedbacks in the coupled ocean-atmosphere system of the equatorial Pacific, small anomalies in the equatorial SST or in the trade winds can readily and rapidly initiate the development of mature El Niños or La Niñas. At the same time, there are multiple processes that can break down this positive feedback and allow the system to oscillate between positive and negative phases. These processes are currently interpreted as four realizations of a common conceptual framework called the unified oscillator (Wang 2001). In the first hypothesis, called the delayed oscillator (Suarez and Schopf 1988), weaker trades during an El Niño reduce the build-up of warm water in the off-equatorial portion of the Pacific basin, initiating a baroclinic Rossby wave along the thermocline, which propagates westward. Once the wave reaches the continent it reflects back as an equatorial Kelvin wave and travels eastward, shoaling the thermocline in the eastern equatorial Pacific, decreasing the positive SST anomalies, which reverses the state of ENSO. The second mechanism, the western Pacific oscillator (Weisberg and Wang 1997), also traces the ENSO oscillation back to thermocline waves. In this case the

Kelvin wave that reverses the ENSO oscillation originates not from westward propagating Rossby waves, but from off-equatorial changes in thermocline depth in the western portion of the basin triggered by off-equatorial cyclones/anti-cyclones induced in response to the equatorial SST variations. The third mechanism, termed the recharge-discharge oscillator (Jin 1997), invokes zonal mean changes of the thermocline depth along the Equator, resulting in either a “charged” (deeper thermocline) or “discharged” (shallower) state. In particular during a mature El Niño (La Niña), Sverdrup transport of warm water poleward (equatorward) induced by off-equatorial changes in the trade winds transitions the system towards the opposite state by discharging (recharging) the Equator, resulting in a zonal mean thermocline depth that is lower (greater) than the average value. Finally, the fourth mechanism, the advective–reflective oscillator (Picaut, Masia and du Penhoat 1997), hypothesizes that during an El Niño event, while the western Pacific warm water pool (WPWP) moves eastward, the accompanying westerly wind anomalies not only force upwelling off-equatorial Rossby waves to propagate westward, they also induce downwelling Kelvin waves that propagate eastward. Once the respective waves reach the continental barriers on either side of the Pacific, they reflect and travel back as upwelling Kelvin waves and downwelling Rossby waves, respectively. The westward zonal currents associated with the two waves subsequently augment one another in the central Pacific and push the WPWP back to the western side of the equatorial Pacific, reversing the ENSO system.

In the alternative framework, ENSO is seen as the coupled response to atmospheric white noise. While in the case of a self-sustained oscillation the ENSO

system evolves with its own dynamics, in the alternative framework the stochastic atmospheric forcings that initiate the onset of ENSO events are not part of the ENSO system itself. Examples of these stochastic triggering mechanisms are the Westerly Wind Bursts (WWB), the Madden-Julian Oscillation (MJO), and the North Pacific Oscillation (NPO)-related sea-level pressure (SLP) anomalies. The WWB, as the name suggests, are short events of westerly wind anomalies in the western portion of the tropical Pacific which have been shown to consistently precede positive ENSO events (Puy, et al. 2019). Their hypothesized mechanism is that by weakening the trade winds in the western Pacific these WWBs allow the WPWP to move eastward. This, in turn, initiates downwelling thermocline Kelvin waves that propagate eastward and increase the SST in the eastern tropical Pacific. A recent study from (Lian, Chen and Tang 2014) argues that the WWB can influence the occurrence of either EP or CP El Niño depending on when they happen in relation to the stage the ENSO oscillation finds itself in. By comparison, the MJO is an intraseasonal mode of variability that carries SLP and convective anomalies eastward through the Indian and Pacific Oceans. The MJO has been shown to affect ENSO positively when the convective portion of the MJO reaches the western Equator during boreal spring (Hendon and Wheeler 2007). At that point, the MJO anomaly causes westerly anomalies in the trade winds in the far-western portion of the tropical Pacific that can either initiate a downwelling Kelvin wave or induce the SST anomalies of the WPWP to move eastward, providing the initial conditions for the development of an El Niño (Kapur and Zhang 2012), (Tang and Yu 2008).

Finally, anomalous SLP patterns in the subtropical North Pacific, related to the North Pacific Oscillation (NPO), can give rise to either positive or negative ENSO events depending on the sign of the SLP variations. For instance during a positive NPO phase, its SLP anomalies weaken the subtropical high thus reducing the strength of the Northern off-equatorial trade winds. These tropical westerly anomalies have a direct dynamic impact, referred to as the Trade Wind Charging (TWC), and an indirect thermodynamic effect due to the warmer SST anomalies underlying the weakened winds called the Northern Pacific Meridional Mode (NPMM). Three potential mechanisms have been hypothesized to connect NPMM to the onset of ENSO. They all link, in different ways, the NPMM to equatorial Kelvin waves that propagate along the thermocline and initiate El Niño events. First, the warm extratropical SST anomalies expand south-westward due to the positive wind-evaporation-SST (WES) feedback. Once the warm anomalies reach the western equator, the anomalous westerly winds that accompany them can excite equatorial Kelvin waves (Liu and Xie 1994). Secondly, the westerly wind anomalies associated with NPMM can excite off-equatorial Rossby waves in the spring which propagate westward and reflect as equatorial Kelvin waves (Alexander, et al., 2010). Third, the extratropical anomalous warm SST can cause the intertropical convergence zone to shift northward, inducing a weakening in the equatorial trade winds that can excite equatorial Kelvin waves (Amaya, Kosaka, et al. 2019). At the same time, the weakened off-equatorial trade winds have a dynamic impact by establishing off-equatorial, anti-cyclonic wind stress curl that in turn induces vertically-integrated meridional mass transport into the central portion of the Equator. The convergence of

warm water in the subsurface gives rise to a “charged” equatorial Pacific, which initiates the onset of El Niño events (Anderson and Perez 2015).

### **Scientific Questions and Findings**

Given this background, the goal of this particular research project is to investigate the relationship between ENSO and the NPO-related precursor, including the dynamics of the TWC (Anderson, Perez and Karspeck 2013) as well as the thermodynamics of the NPMM (Larson and Kirtman 2013). Their combined influence on ENSO is henceforth referred to as TWC/NPMM forcing.

The motivating question for the initial chapter of this research project is: how robust is the TWC/NPMM-ENSO relationship and has this relationship shown any internal variability in the past?

The analysis shows that the relation between ENSO and the TWC/NPMM driver has been strong from 1870 until 1920, then weakened during the following four decades, before regaining strength from 1960 onward. The TWC/NPMM signal is active during the entirety of 1870-2011, and that it is only the coupling with ENSO that weakens between 1920 and 1960. Furthermore, a combination of composite analysis of the months leading up to and following a positive ENSO event, and spectral analysis shows that the internal variability of ENSO differs between the periods of strong and weak TWC/NPMM-ENSO relationship. In particular, during 1920-1960, the ENSO signal has a constant 6 years long periodicity, and the system’s oscillations between opposite states are distinct. During the intervals of 1960-2011 and 1870-1920, instead, the power of the ENSO signal is spread over a diverse range of periodicities. This led to the hypothesis

that the change in the oscillatory behavior of ENSO results from a change in its driving mechanism. During both the first and the third periods, ENSO is responding to stochastic forcing, hence the diverse range of oscillatory periods. Between 1920 and 1960 instead, ENSO appears to behave like a self-sustained oscillation.

These findings on the nature of the TWC/NPMM-ENSO raise the second set of questions, namely, how do state of the art coupled climate models simulate the TWC/NPMM-ENSO relationship? First, do they recreate the TWC/NPMM precursor? If so, do they capture the internal variability of the TWC/NPMM-ENSO relationship and the concurrent internal variability of ENSO oscillatory behavior? And, in conclusion, how does this ensemble reconstruct the TWC/NPMM-ENSO relationship in the presence of increasing external forcings?

Despite clear variations across the ensemble, the TWC/NPMM is reconstructed by all models as an ENSO precursors. Then, after isolating periods when the behavior of the ENSO changed from oscillatory to stochastic, I revealed that ENSO is preceded by TWC/NPMM when the periodicity is stochastic, but not during periods when it is oscillatory. The models thus reproduce the same features of ENSO internal variability, which are mirrored by changes in the TWC/NPMM-ENSO relationship as it was identified in the reanalysis data. As I include increasing external forcings in the analysis, I show that TWC/NPMM-related ENSO events are consistently stronger than the former events, and that this relation holds true both with constant and increasing external forcings. Further, the ensemble predicts a shift towards larger ENSO events whose center of heat moves consequently westwards, in the presence of increasing external forcings.

When studying the ENSO signal, I find that in the majority of models there is an increase of the overall power of ENSO during the years 1950-2050. However, this power trend is not connected to specific changes in how the ENSO system oscillates. In particular, we see no clear trends in the rate at which ENSO oscillates, nor in its stochasticity. This final result, together with the fact that we see no shift in the strength of the TWC/NPMM-ENSO relationship, agrees with previous findings of this thesis.

In conclusion, as ENSO's driving mechanisms all rely on interactions between the ocean, both at the surface as well as along the thermocline, and the overlying winds and pressure fields, the horizontal resolution of the models could play a fundamental role in how accurately those interactions and, consequently, the TWC/NPMM-ENSO relationship are represented in the model. Therefore, I utilize an ensemble of state of the art models (further details below) that is specifically designed to systematically investigate the impacts of increasing horizontal resolution to an eddy-permitting level. I thus test one corollary question: does horizontal resolution have an impact on a model's ability to reconstruct the TWC/NPMM-ENSO relationship and its variability?

The results both with constant and increasing atmospheric forcings suggest that the horizontal resolution does not play a consistent role in the models' ability to isolate either ENSO or TWC/NPMM, or the internal variability of their relationship.

### **Data and Methods**

The variables for this analysis are winter-seasonal means of SST (NDJ) and  $\tau_x$  (NDJF) anomalies, constrained in the region of ENSO dynamics [20S-20N, 120E-70W]. The  $\tau_x$  is the chosen variable to capture the westerly wind anomalies that characterize the



TWC/NPMM, while SST is the chosen variable to capture ENSO variability, 1 year later. For the first study, the ocean variable (SST) is retrieved from the latest version of the Simple Ocean Data Assimilation reanalysis with sparse observation input (SODAsi.3), and the atmospheric variable ( $\tau_x$ ) is retrieved from the 20th Century Reanalysis Version v2c, between 1870-2011. In the second set of studies, I retrieved those same variables from the High Resolution Model Intercomparison Project (HighResMIP) which is a protocol-driven ensemble part of the CMIP6. I specifically focus on three sets of HighResMIP experiments: (1) control-1950, a 100 years long simulation with constant 1950's radiative forcing levels which correspond to a global radiative forcing of  $\sim 0.5$  W/m<sup>2</sup> (Myhre, et al. 2013); (2) hist-1950, an experiment with prescribed radiative forcings from 1950 to 2014; and (3) highres-future, a simulation that continues from where hist-1950 ends until 2050, with increasing external forcings prescribed to follow the RCP8.5 scenario from the fifth IPCC. In this pathway no mitigation efforts are implemented (Pachauri and Alle 2014) and radiative forcing reaches 8.5 W/m<sup>2</sup> by 2100 (Riahi, et al. 2011). In particular, the third chapter focuses on the control experiments, while the fourth carries out a comparison between control and historical+future experiments.

Given that my focus was on the changing nature of the TWC/NPMM-ENSO relationship, I employed a method that could capture the time correlation between the two modes. Namely, I applied a variant of the Canonical Correlation Analysis (CCA), which is thoroughly discussed in (Bretherton, Smith and Wallace 1992) where it is referred to as “CCA in the basis of Principal Components” and is an established tool for analyzing

coupled climate variables (Graham, Michaelsen and Barnett 1987) (Anderson 2003). This method differs from the classic CCA because the inputs do not comprise the entire fields of interest, but a subset of Principal Components obtained by first applying the Empirical Orthogonal Functions (EOF) on both variables. This intermediate step is of particular importance because it significantly reduces part of the noise (Bretherton, Smith and Wallace 1992). The CCA then returns pairs of time series, sorted such that the first one represents the pair of modes having the highest correlation.

In the third chapter, I combine the CCA in the basis of PC's with techniques that are specifically designed for multi-model inter-comparisons. To start, I reconstruct the most highly correlated fields of SST and preceding zonal wind stress for each experiment. The ensemble performance is then quantitatively assessed with the help of Taylor diagrams and pattern correlation analyses, by comparing the  $\tau_x$  fields obtained in the reanalysis data against those of the model ensemble. In the fourth chapter, I turn to the Center of Heat Index (CHI) (Giese and Ray 2011) to carry out the spatial characterization of the TWC/NPMM-ENSO relationship as well as to develop CHI-analogous indices to study how the power of ENSO spreads across different periodicities.

## CHAPTER TWO

### Introduction

The El Niño Southern Oscillation (ENSO), the largest mode of coupled atmosphere-oceanic variability in the tropical Pacific Ocean, has attracted the attention of the scientific community because of the widespread influence it has on large-scale atmospheric circulations beyond the tropical Pacific (Rasmusson & Carpenter, 1982) and the consequences it carries for weather patterns worldwide (Alexander, et al., 2002).

ENSO is a natural oscillation in the tropical Pacific comprising a mean state and two anomalous ones: El Niño and La Niña. The neutral state consists of colder sea surface temperatures (SSTs) off of the Peruvian coast and warmer water by Australia and South-East Asia. This dipole gives rise to a gradient in sea level pressure (SLP) that sustains the Pacific Walker circulation: convective, wet conditions in the West and dry, high pressure conditions in the East, with easterly trade winds along the Equator. During La Niña, cooling of the SSTs in the east (and warming in the west) enhance the mean SST and SLP gradient, thus intensifying the features of the Walker circulation. By contrast, during El Niño, anomalous warming of the SSTs in the east (and cooling in the west) generate SST and SLP anomalies that are of opposite sign with respect to the neutral state. This causes a weakening of the mean state; in addition the convective branch of the Walker circulation is shifted eastwards over the Ocean (Sarachik & Cane, 2010).

The impacts of ENSO's seesaw are felt at a global scale. The most direct effects are changes in precipitation and pressure patterns over Northwestern South America, Australia and the Indo-Pacific region as a consequence of the shift in the Walker

circulation (Dai & Wigley, 2000; Cai et al., 2011). More indirectly, impacts are registered in the extratropical Pacific: along the western North Pacific, for instance, ENSO modulates the intraseasonal oscillation during the months of May-October (Liu et al., 2016). Other basins are also affected by the oscillation of ENSO. In the Indian Ocean, alternate phases of the Pacific mode have been shown to affect the internal dynamics of the basin and the Indian Ocean Dipole (Ummenhofer et al., 2012); similarly, the Summer Indian Monsoon precipitation can be strongly dampened by the occurrence of El Niño events (Ashok et al., 2004). Such events significantly affect natural ecosystems and human settlements alike. In order to predict, and prepare for, such events and thereby improve the resilience of affected communities and ecosystems, it is critical to examine more closely the dynamics of ENSO.

A large body of literature has explored the complex mechanisms that trigger, enhance and maintain the coupled atmosphere-oceanic dynamics of ENSO. The positive feedback, first described in research by (Bjerknes, 1969), is known to enhance SST anomalies in the Tropical Pacific, until they develop into mature ENSO events. This cannot however explain the oscillatory behavior of the system: after full-grown El Niños and La Niñas the ocean returns to its mean state or oscillates to one of opposite sign. This oscillatory feature has been explained through four main hypotheses. They all characterize ENSO as a self-sustained system where SST-related feedbacks and tropical ocean dynamics force the dipole to oscillate; these four hypotheses are now seen as special cases of the unified oscillator (Wang et al., 2017). Although these theories are able to capture an important aspect of ENSO's behavior, they do not provide a sufficient

explanation for ENSO's non-stationarity, which has been ascribed to tropical stochastic mechanisms such as the Madden Julian Oscillation (Kaplan & Zhang, 2012) and Westerly Wind Bursts (Puy, et al., 2019). These mechanisms have been shown to alter the mean state of the Tropical Pacific, triggering anomalies that, through aforementioned positive feedbacks such as the Bjerknes feedback, can modulate the system and alter the oscillation.

Most stochastic “triggering” mechanisms identified so far reside in the Tropical Pacific. However many results suggest an extratropical influence on the ENSO onset. Among these mechanisms, the boreal spring Arctic Oscillation has been shown to have a significant impact, particularly on the onset of positive ENSO events (Chen, Chen and Yu 2014); additionally both strong and weak Aleutian low conditions have been found to impact La Niña and El Niño respectively (Chen, Chen and Wu, et al. 2020). Further, anomalous atmospheric conditions over the central North Pacific, related to the North Pacific Oscillation (NPO), have been shown to consistently precede ENSO events by 9-10 months (Anderson, 2003; Vimont et al., 2001 and Pierce et al., 2000). During this time, NPO-induced winter-time SLP anomalies cause anomalous zonal winds that weaken the off-equatorial trades. Weakened trade winds have both a thermodynamic and dynamic impact on the tropical Pacific. Thermodynamically, these anomalous winds reduce latent heat flux from the underlying ocean, resulting in positive SST anomalies (SSTAs) in the northern extratropics during the spring. This chain of events gives rise to the North Pacific Meridional Mode (NPMM) and its signature meridional gradient of SSTAs: warm SSTAs in the extratropics and cold SSTAs in the eastern Equator (Amaya,

2019). Three potential mechanisms subsequently connect the NPMM to the onset of ENSO. First, through the wind evaporation SST (WES) feedback, the positive extratropical SSTAs migrate south-westward towards the western portion of the Pacific Equator. Anomalous westerly winds follow the SSTAs equatorward and there can excite equatorial Kelvin waves that then initiate the onset of ENSO (Liu & Xie, 1994). Secondly, NPMM-associated wind anomalies can excite Rossby waves in the spring which then reflect as equatorial Kelvin waves as well (Alexander, et al., 2010). Third, the extratropical SSTAs can shift the intertropical convergence zone (ITCZ) northward, thus causing a weakening of equatorial trade winds that can also excite equatorial Kelvin waves (Amaya, et al., 2019).

Dynamically, the NPO-induced wind-stress anomalies in the northern extratropics not only influence the underlying SST fields (as discussed above) but also induce substantial equatorial and off-equatorial subsurface temperature anomalies via meridional and vertical circulations respectively. In particular, the NPO-induced weakening of the trades results in an off-equatorial wind stress curl that produces significant vertically-integrated meridional mass transport into the equatorial region. The convergence of meridional mass transport along the equator in turn generates extensive subsurface heat content changes representative of a “charged” equatorial Pacific, which serves as an influential initiator of mature El Niño events (Anderson & Perez, 2015). For this reason, this dynamic mechanism is called Trade Wind Charging (TWC henceforth). Given that NPO-induced off-equatorial trade wind anomalies have both a thermodynamic (NPMM) and dynamic (TWC) influence on the tropical Pacific and subsequent onset of

ENSO events, following the lead of Anderson and Perez (2015) we will refer to the influence of these trade wind variations as TWC/NPMM forcing of ENSO variability. As discussed in a recent review (Pegion and Selman 2017) several independent results conclude that extratropical ENSO-precursors, such as the NPMM and the NPO, are subject to multi-decadal internal variability. Furthermore, a recent paper by Zhao and Di Lorenzo (2020) shows that a significant portion of the tropical Pacific low-frequency variability can be traced back to extratropical ENSO-precursors. In their conclusion, Pegion and Selman (2017) highlight the need for further investigations to address this specific issue, particularly in light of possible future changes due to increased greenhouse gases concentration. In order to contribute to this endeavour, this paper investigates the evolving relationship between TWC/NPMM forcing and the development of mature ENSO events the following Boreal winter. In particular, thanks to the extended length of recently developed, multi-century ocean reanalyses, the chapter shows how the relevance of TWC/NPMM forcing as a leading mechanism has its own oscillatory behavior. Interestingly, analysis of those years when ENSO is not subject to the TWC/NPMM forcing indicates that no other driver prevails either, but that ENSO has a self-sustained oscillation. Furthermore, the mode's periodicity has a much narrower frequency band, and we see most notably that unforced ENSO events oscillate more regularly and slower than in the intervals when the TWC/NPMM forcing is present. These results put those of Yu and Fang (2018) - which indicate that the seasonal footprinting (SF) mechanism (equivalent to the TWC/NPMM here) contributes to a more stochastic evolution of ENSO, while the recharge-discharge mechanism gives rise to a more regular oscillation -

in a larger historical context while also isolating the characteristic oscillatory behavior in the observed system.

The Data and Method section provides an overview of the reanalysis dataset, the variables included, and the methodology utilized to isolate the coupling between ENSO and TWC/NPMM forcing. The Results section explores the time evolution of the co-variability between the two modes and identifies those time intervals when TWC/NPMM forcing is the leading precursor and those when it is not, with a particular focus on the interval when TWC/NPMM-ENSO relationship is weaker. In the Conclusion, we then summarize these findings and discuss them in the context of previous investigations into the nature of ENSO variability.

## **Data and Method**

### *Data*

The variables for this analysis are retrieved from the latest version of the Simple Ocean Data Assimilation reanalysis with sparse observation input, called SODAsi.3. We provide here an overview of the dataset, which is thoroughly presented in Giese, et al. (2016).

This latest version contains several improvements, introduced to solve biases that had emerged in previous reanalysis dataset. First, the only variable from oceanic observations assimilated in the reanalysis is SST. This was done to compensate for bias caused by the inhomogeneous amount of available variables, particularly in the subsurface before and after the 1950's. The observations are retrieved from the International Comprehensive Ocean-Atmosphere Dataset, version 2.5, and are assimilated following a 10-day long update cycle through a loosely coupled set of iterations between the SODAsi system for



oceanic data and atmospheric boundaries from the 20th Century Reanalysis (20CRv2c). The loosely coupled iteration is meant to improve the mutual consistency between atmospheric and oceanic data, which is very important for a reanalysis that extends deep into the 19th century when ocean observations are extremely sparse, and the need is to rely on atmospheric data. Finally, SODAsi.3 is forced with individual ensemble member data from 20CRv2c, instead of using the ensemble mean as had been done in previous versions. This adjustment is also done in order to reduce the large biases that averaging in times of sparse observations can carry.

The variables utilized in the analysis are SST from SODAsi.3 and horizontal wind stress ( $\tau_x$  and  $\tau_y$ ) from 20CRv2c, taken from all eight ensemble members. Time wise, the interval is cut to 1871-2011, from the original 1815-2011, since a higher number of observations is included in the assimilation after 1871, making the data more robust. Furthermore, in order to assess that our results are not data-dependent, we repeated several steps of our analysis using other reanalysis datasets that cover similar extended, centennial timeframes: ersst.v5 for SST and ERA-20C for wind stress. The results confirm the robustness of our analysis (not shown).

### *Method*

First, the variables for the analysis (SST and  $\tau_x$ ) are spatially constrained in the region of interest for ENSO dynamics: between latitudes 20S and 20N and longitudes 120E and 70W similar to the one used in Anderson and Perez (2015) and in Larson and Kirtman (2013). Secondly, since both ENSO and NPO-induced wind-stress forcing have their most active seasons during Boreal Winter, the variables are averaged over November-

January for SST (Trenberth, 1997) and November-February for  $\tau_x$  (Anderson & Perez, 2015). Since the focus of this paper is the internal variability of ENSO and its drivers, the seasonal means are de-trended, in order to remove externally-induced low-frequency alterations. Finally, since NPO-induced TWC/NPMM activity occurs one year before mature ENSO events, the seasonal time series of SST and  $\tau_x$  are arranged in order to have a one year lag between them. This data aggregation is performed separately for each of the eight SODAsi.3 ensemble members. For both fields, the eight ensemble members are concatenated along the time dimension, resulting in an aggregate of 1112 (139x8) years of data at each grid point. This approach constrains the results, making them less sensitive to the noise one single member might be carrying, while keeping potentially important internal variability.

Next, we seek to identify winter modes of wind-stress variability that precede large-scale changes in SST anomalies the following year. This is carried out by adopting an already established variant of the Canonical Correlation Analysis (CCA) (Anderson, 2003). Applying a technique used in previous analyses (Graham, et al., 1987), we first isolate large-scale modes of variability with the help of Empirical Orthogonal Functions (EOF). EOF analysis is a tool that has been widely utilized to reconstruct climate modes (Dai, et al., 2015; Kessler, 2001), because of its ability to isolate modes of high variability from space-time matrices. In this study, EOF is used on space-time matrices of both SST and  $\tau_x$  and we will refer to them as S and T respectively. In particular, we are interested in the Principal Components (PC's) of the covariance matrix of both variables which are obtained by calculating a Single Value Decomposition (SVD) on S and T. The

SVD returns PC'S as vectors in decreasing order of variability, ensuring that a large fraction of the variability of both SST and  $\tau_X$  can be isolated by simply extracting the first PC's. These vectors of high variability are then used as inputs for the CCA.

While the EOF analysis returns modes of variability for each field separately, the CCA between two variables captures modes having the highest co-relation, expressed in pairs of times series: the Canonical Variables (CV). In this case, the co-relation is investigated between high variability subfields of SST and  $\tau_X$  constructed through PC's. The number of PC's included in the CCA is decided recursively by maximizing the correlation between the first pair of CV's with the trade-off of an 85% threshold on the total included variability for each variable. This variant of the CCA is thoroughly discussed in Bretherton, et al. (1992) where it is referred to as "CCA in the basis of Principal Components" and is regarded as one of the two best options to isolate coupled modes. Furthermore, since the aim is to isolate the TWC/NPMM forcing mode, and since wind signals concurrent with ENSO can interfere with the TWC/NPMM reconstruction, the former are removed following the lead of (Larson & Kirtman, 2014). This is done excluding the first PC of  $\tau_X$  which captures the time evolution of ENSO. As a robustness test, ENSO was also linearly removed from zonal winds using the concurrent Niño 3.4 index, and the final results were identical. The CCA analysis returns paired canonical variables, one for SST ( $CV^k_{SST}(t)$ ) and the other for  $\tau_X$  ( $CV^k_{\tau_X}(t-1)$ ), where k is the index of the pair. The pairs are sorted such that the first one ( $CV^1_{SST}(t), CV^1_{\tau_X}(t-1)$ ) represents the pair of modes having the highest correlation.

## Results

To start, CCA is first applied to the SST and wind stress anomalies during the interval between 1960 and 2011. This interval is selected for two reasons: (1) data from these latter decades are more robust because of a larger number of available observations and because of their widespread distribution over the globe; (2) the second half of the 20th century has been the object of multiple, previous analyses of the ENSO-NPO relationship and therefore allows us to test our method and data against these previous results (e.g. Anderson, 2003; Anderson & Perez, 2015 and Larson & Kirtman, 2014). Following the steps described in the Method section, we first isolate the time series for the leading pair of coupled modes of SST and preceding wind stress anomalies:  $CV^1_{SST}(t)$  and  $CV^1_{\tau_X(t-1)}$ , respectively. As expected, the time series are highly correlated ( $\rho = 0.76$  - Figure 1a). In addition, the time evolution of the SST mode  $CV^1_{SST}(t)$  is highly correlated with the concurrent seasonal (NDJ) Niño3.4 index ( $\rho = 0.8$ ). The corresponding zonal wind-stress pattern (Figure 1b) indicates large, positive zonal wind-stress anomalies in the central tropical North Pacific, with weaker negative (positive) zonal wind stress anomalies along the central (western) equatorial Pacific, while the SST pattern (Figure 1c) one year later indicates large, positive SST anomalies across the tropical Pacific. To expand our view, we regress  $CV^1_{SST}(t)$  against concurrent SST

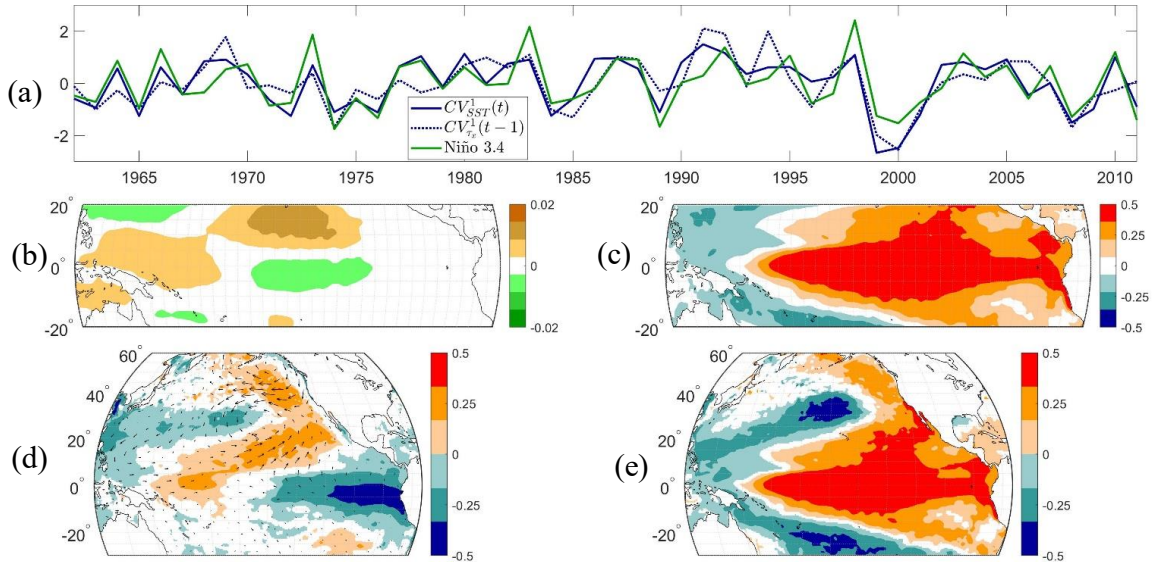


Figure 1 Results from Canonical Correlation Analysis (CCA) of sea surface temperature (SST) anomalies and preceding zonal wind stress ( $\tau_x$ ) anomalies over the interval 1960-2011. (a) Time-series of the first Canonical Variables of seasonal SST (NDJ) and preceding seasonal  $\tau_x$  (NDJF):  $CV^1_{SST}(t)$  (thick blue) and  $CV^1_{\tau_x}(t-1)$ , (dotted blue) respectively. The time series have variance  $\sigma^2 = 1$  and mean  $\mu=0$ . They are plotted together with the normalized Niño3.4 index, concurrent with  $CV^1_{SST}(t)$  (green). Note: the three time series are plotted with respect to January of the seasonal mean of the SST time series, hence  $CV^1_{\tau_x}(t-1)$  is shifted 1 year forward.

(b) Seasonal  $\tau_x$  anomalies regressed against  $CV^1_{\tau_x}(t-1)$  over the CCA region. Magnitude of  $\tau_x$  anomalies ( $N/m^2$ ) given by color bar on the r.h.s of the panel. (c) Seasonal SST anomalies regressed against  $CV^1_{SST}(t)$  over the CCA region. Magnitude of SST anomalies (K) given by color bar on the r.h.s of the panel.

(d) Seasonal SST (NDJ) and  $\tau_x$  (NDJF) anomaly fields regressed against  $CV^1_{\tau_x}(t-1)$ . (e) Seasonal SST (NDJ) anomaly fields regressed against  $CV^1_{SST}(t)$ . In both panels, the plots are created by regressing anomaly fields concurrent with the corresponding CV, thus the left panel precedes the right one by 1 year. Magnitude of SST anomalies (K) given by color bar on the r.h.s of the panels. Only results significant at  $\alpha=0.95$  are shown.

anomalies (Figure 1e) which not surprisingly reveals the characteristic features of a

positive El Niño: positive SST anomalies along the Central and Eastern Equator

extending in the extra-tropics along the Western coast of the North American continent,

alongside negative anomalies in the Western portion of the Equator. Further, regressing

$CV^1_{\tau_X}(t-1)$  against concurrent SST and wind stress fields reveals underlying SST anomalies characteristic of the Meridional Mode (Figure 1d). In addition, the concurrent wind stress anomalies contain a cyclonic circulation centered on the Hawaiian Islands - characteristic of an anomalous weakening of the southern lobe of the NPO—with a corresponding weakening of the off-equatorial Northeast trades over the central and eastern Pacific. As such, during the period 1960-2011, our analysis indicates that the leading mode of wind-stress variability preceding mature ENSO events is the TWC/NPMM forcing mode, which agrees well with previous research (Vimont, et al., 2001; Anderson, et al., 2013 and Anderson & Perez, 2015).

Having confirmed the use of the method and data outlined in the respective section, we now turn our attention to analyzing the full time period 1871-2011, and possible changes in the relationship between ENSO and the TWC/NPMM forcing. To start, we apply the same CCA method on 56 subintervals of the full 1871-2011 time period. These subintervals are obtained by splitting 1871-2011 into 31-year periods offset by 2 years, e.g., 1871-1901, 1873-1903, and so forth (note – results are insensitive to the exact offset length). For each subinterval  $j$ , CCA returns the leading pair of coupled time series,  $CV^{1,j}_{SST}(t)$  and  $CV^{1,j}_{\tau_X}(t-1)$ . We then regress  $CV^{1,j}_{\tau_X}(t-1)$  against the concurrent zonal wind stress anomalies at each grid point, to obtain the corresponding maps  $T^j_X$ , for each subinterval  $j$  (as was done in Figure 1b). Once we have obtained the 56 maps of wind stress variability,  $T^1_X, \dots, T^{56}_X$ , we want to isolate the most common pattern that they share and how that pattern manifests across subintervals. In order to do so, we treat  $T^j_X$  as vectors of a space-time matrix  $T_X$ , where each subinterval  $j$  represents a time point.

We then perform an EOF analysis on  $T_X$  itself. Importantly, we do not remove the temporal mean from the matrix, following the examples of Wang, et al., 2010, and Chamail -Jammes, Fritz and Murindagomo, 2006. As such, the first EOF ( $EOF_1$ ) isolates the most common pattern across subintervals, while the first PC ( $PC_1(t)$ ) captures how strongly that pattern manifests itself within a given wind stress anomaly map  $T_X^j$ . The results can be seen in Figure 2. In Figure 2a a sample of the  $T_X^1, \dots, T_X^{56}$  maps upon which the EOF analysis is applied. The panel in Figure 2b shows the spatial component of the first EOF. In this field, one can clearly identify the strong positive

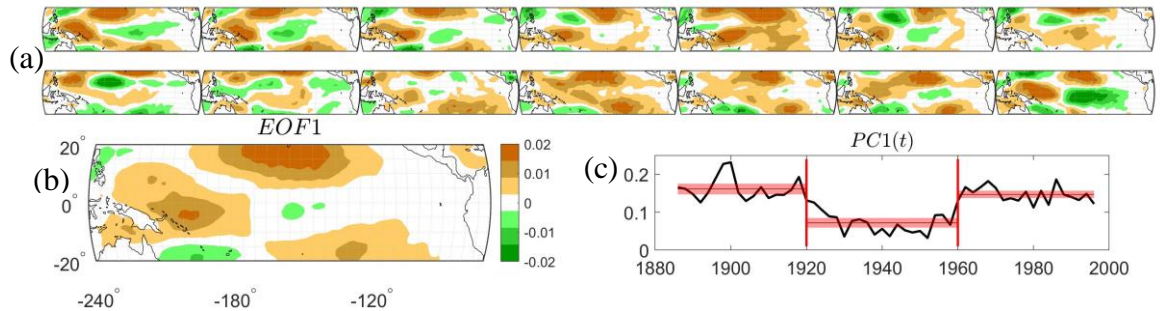


Figure 2 Results from CCA applied to 56 30-year sub-intervals from 1871-2011. (a)  $\tau_X$  anomalies regressed against the concurrent  $CV^1 \tau_X(t-1)$  in the 30-year sub-intervals.  $CV^1 \tau_X(t-1)$  for each sub-interval is obtained using CCA as described in the text. The regression maps for all 30-year sub-intervals comprise the reconstructed zonal wind stress fields  $T_X^1, \dots, T_X^{56}$ . Here only every fourth map is included for visualization purposes. Positive (negative) values are shaded brown (green). The spatial extension of the maps is the same as in (b). (b) Spatial component of the first EOF ( $EOF_1$ ) derived by applying an EOF analysis to the reconstructed zonal wind stress fields  $T_X^1, \dots, T_X^{56}$  – see text for details. Magnitude of zonal wind anomalies ( $N/m^2$ ) given by color bar on the r.h.s of the panel. (c) Time series of the first Principal Component ( $PC_1(t)$ ), plotted at each 30-year sub-interval’s mid-point. For each subinterval, the horizontal red bars indicate the  $\alpha=0.95$  confidence interval around the mean value calculated over their respective time points.

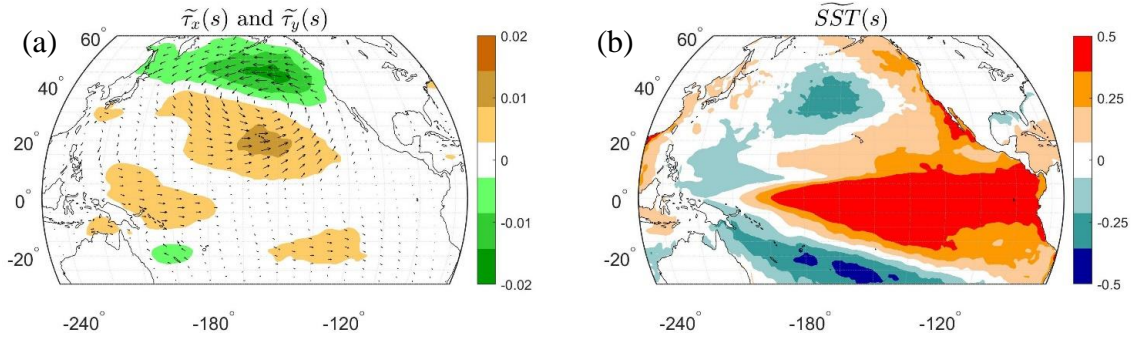


Figure 3 Weighted mean  $\tau_x$  and SST fields associated with  $PC_1(t)$  plotted in Figure 2c. The anomalies are weighted based on the values of the vector  $PC_1(t) / \|PC_1(t)\|_1$ , where  $\|PC_1(t)\|_1$  is its 1-norm.

(a) Weighted mean seasonal wind stress (NDJF) anomalies (black arrows with zonal component in colored shading) using  $PC_1(t) / \|PC_1(t)\|_1$  values at a particular sub-interval to weight the corresponding reconstructed wind stress maps,  $\mathbb{T}_x^1, \dots, \mathbb{T}_x^{56}$  for that sub-interval. Magnitude of zonal wind anomalies ( $N/m^2$ ) given by color bar on the r.h.s of the panel.

(b) Weighted mean seasonal SST (NDJ) anomalies (in colored shading), using  $PC_1(t) / \|PC_1(t)\|_1$  values at a particular sub-interval to weight the corresponding reconstructed SST maps. The maps are derived by regressing the SST anomalies against the  $CV^1_{SST}(t)$  for each 30-year sub-interval. Here,  $CV^1_{SST}(t)$  for each sub-interval is obtained using CCA as described in the text. By construction  $CV^1_{SST}(t)$  lags  $CV^1_{\tau_x}(t-1)$  by one year for the same sub-interval and hence the right panel lags the left panel by one year. Magnitude of SST anomalies (K) given by color bar on the r.h.s. of the panel.

signature between 10N-20N, corresponding to the westerly anomaly typical of

TWC/NPMM forcing mode. The time series of the first PC is plotted in panel Figure 2c.

$PC_1(t)$  captures the manifestation of  $EOF_1$  throughout the subintervals. Interestingly, it appears that the manifestation of the  $EOF_1$  pattern – i.e. the TWC/NPMM forcing mode – within the leading modes of coupled SST/wind-stress variability (as determined by CCA) is subject to a low-frequency oscillation. In particular, the TWC/NPMM forcing mode manifests strongly during the beginning and the end of the 1871-2011 time interval, but not during the intervening period comprised roughly between 1920 and 1960 (red bars over the plot).



In order to confirm that  $EOF_1$  captures the manifestation of TWC/NPMM forcing of ENSO events, we calculate a weighted mean of the regression maps of zonal winds during each subinterval,  $T^1_x, \dots, T^{56}_x$ , where the weights are provided by the time series  $PC_1(t)$ . Similar weighted mean maps are reconstructed using the regression maps of meridional wind stress during each subinterval, as well as the regression maps of SST anomalies from the following Boreal winter (again, each of the regression maps of SST and meridional wind stress anomalies for a particular subinterval are generated using the  $CV^{1j}_{SST}(t)$  and  $CV^{1j}_{\tau_X}(t-1)$  for that subinterval, respectively). As expected, the larger-scale wind stress anomaly pattern during years with active TWC/NPMM forcing (as determined from the  $PC_1(t)$  weights) contain an anomalous weakening of the southern lobe of the NPO along with a corresponding weakening of the off-equatorial Northeast trades over the central and eastern Pacific (Figure 3a). Further we find the subsequent SST anomalies pattern during the following winter is characteristic of a positive ENSO event (Figure 3b). Based upon the results from both Figure 2 and Figure 3, we conclude that the TWC/NPMM forcing mode is the leading empirical precursor to mature ENSO events across the period 1871-2011, however the influence of the TWC/NPMM forcing mode upon ENSO variability is decadal modulated, as seen in Figure 2c. In order to attest whether the oscillation is due to a change in the coupling with ENSO or in the TWC/NPMM mode itself, we reconstruct the variance of the latter. For each of the 56 subintervals, we compute the pattern correlation between the seasonal zonal wind anomalies and the  $EOF_1$  map shown in Figure 2b. This returns 56 time series, each capturing how the TWC/NPMM mode manifests over its respective subinterval. We then

calculate the variance of these time series, shown in Figure 4. The variance is fairly stationary, which suggests that the TWC/NPMM mode is active throughout the 1871-2011 time interval. The oscillation that we isolated in Figure 2c is therefore a feature only of its role as a forcing mechanism of ENSO.

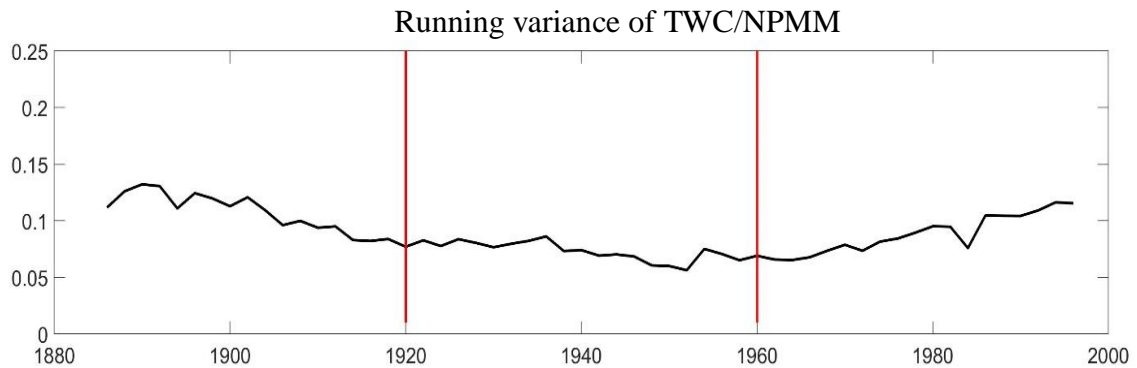


Figure 4 Variance of the TWC/NPMM signal throughout all 30-year sub-intervals. The time series shows the variance of the 30-year time-series generated by performing a pattern correlation between the EOF<sub>1</sub>, in Figure 2b, and seasonal  $\tau_x$  (NDJF) anomalies for each year within the given 30-year sub-interval. The variance of the correlation time series is then computed for each sub-interval and plotted here against the sub-interval's mid-point (unitless).

Based upon these results, the full interval 1871-2011 is split in the three subintervals identified by the red bars in Figure 2c: 1871-1921, 1920-1961, 1960-2011. The third interval is the one that has already been analyzed in the previous subsection; in the next subsections we analyze the other two, with a particular focus on the middle interval when the role of the TWC/NPMM mode, as an ENSO forcing mechanism, appears to be weaker.

The CCA, when applied to the subinterval 1871-1921, returns two fields that are fairly consistent with the ones shown in Figure 1. The correlation between the wind-stress and SST time series is lower than the one for the 1960-2011 period ( $\rho = 0.49$ ), but the correlation between  $CV^1_{SST}(t)$  and Niño3.4 is much higher ( $\rho = 0.99$ ). This latter result

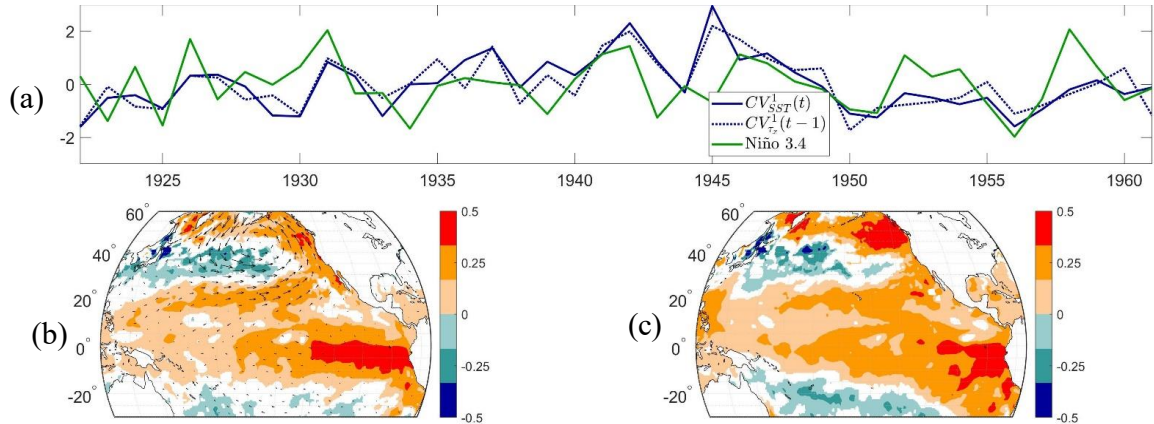


Figure 5. Same as Figure 1, except for the period 1920-1961. (a) as 1.a, (b) as 1.d, (c) as 1.e.

suggests that  $CV^1_{SST}(t)$  is capturing the ENSO evolution, as confirmed by the regression maps of SST anomalies (not shown). Further, the regression of anomalous wind flux against  $CV^1_{\tau_x}(t-1)$  returns wind fields characteristic of the signature weakening of the southern lobe of the NPO, centered North of Hawaii (not shown). As such, we find that during this first interval the strength of TWC/NPMM forcing mode and its relationship with ENSO are fairly similar to what is shown for the 1960-2011 period, which is in accordance with the modulation of  $PC_1(t)$  in Figure 2c.

Our main interest lies with the subinterval from 1920 to 1961, during which time it appears that the TWC/NPMM forcing mode's relationship with subsequent ENSO variability is weaker (since it does not manifest as strongly in the leading CV patterns during this period's subintervals - Figure 2c). Indeed, when we apply CCA to the period 1920-1961 the reconstructed SST and wind stress fields (Figure 5) bear no resemblance to those in Figure 1. Importantly, the leading mode of coupled zonal wind-stress and lagged SST anomalies across the tropics does not correspond to ENSO's evolution (also

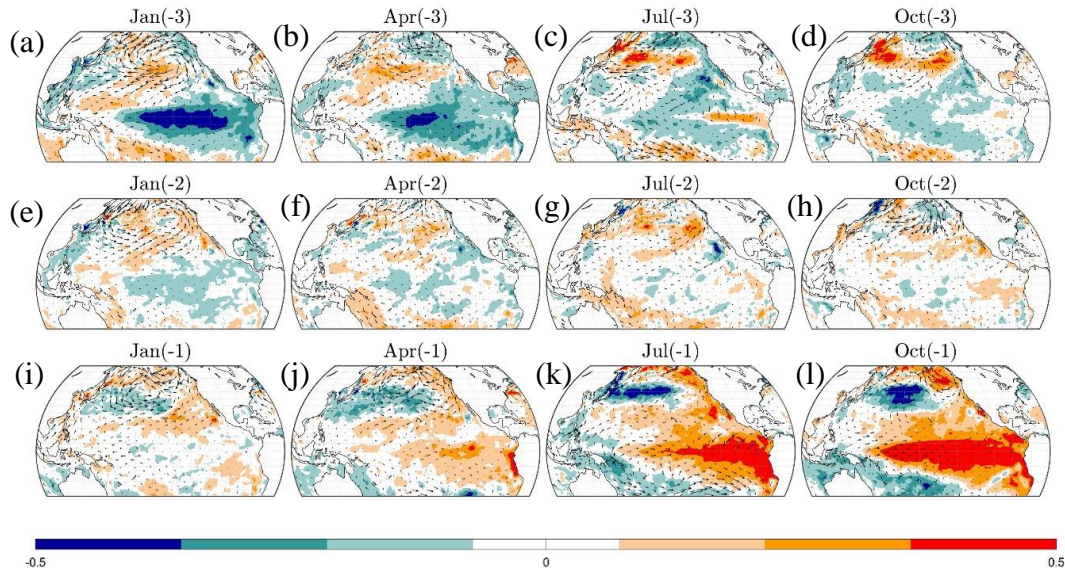


Figure 6. Regression maps of oceanic and atmospheric anomalies preceding positive ENSO events during the 1920-1961 time period. (a) January monthly mean of SST (color shading) and wind stress flux (black arrows) anomaly fields regressed against the normalized seasonal (NDJ) Niño3.4 index 36 months later (i.e. in Year 0). Regression values only calculated over the period 1920-1961. Magnitude of SST anomalies (K) given by color bar at the bottom of the figure. Only results significant at  $\alpha=0.95$  are shown. (b-l) same as (a) except for the monthly SST and wind stress anomaly fields for every 4<sup>th</sup> month up to October one month prior to the NDJ Niño3.4 index.

confirmed by the low correlation between  $CV^1_{SST}(t)$  and Niño3.4,  $\rho = 0.27$ ). This result suggests that not only is TWC/NPMM forcing of ENSO less robust during this period, but that there is no strong coupling between ENSO and any preceding modes of wintertime zonal wind stress anomalies during this 40 years period. Note that the same results holds for the second and the third CVs as well, with neither capturing the ENSO evolution during this period (as represented by their correlation with Niño3.4, which are  $\rho(CV^2_{SST}(t), Niño3.4) = 0.11$  and  $\rho(CV^3_{SST}(t), Niño3.4) = 0.03$ , respectively).

The question at this point becomes: how does ENSO behave during this time interval and does its characteristics differ from those of the other two sub-periods when

TWC/NPMM forcing is active? We return to the winter seasonal (NDJ) Niño3.4 index as the most straight-forward way to isolate ENSO and its evolution. It allows us to study the mode's behavior without making assumptions about that behavior and its couplings with other modes. Firstly, the spatial reconstruction of the SST anomalies against the concurrent Niño3.4 index returns a clear ENSO pattern (not shown), confirming that, albeit having different dynamics, the canonical pattern of ENSO variability is present during these years. To understand how ENSO evolves during this period, we reconstruct the anomalies of the oceanic and atmospheric state during the three years leading up to an El Niño event by performing a lagged regression against the normalized NDJ Niño3.4 index (Figure 6). During the period 1921-1960—in which precursor atmospheric forcing is weak—there is a strong relation between El Niño (Oct(-1)) events (i.e. one month prior to the NDJ Niño3.4 index) and La Niña (Jan(-3)) events three full years earlier. During the intervening months however, there is almost no coherent signal in either the tropical atmospheric or oceanic fields; this holds true even for the prior Boreal winter (Oct(-2)/Jan(-1)), confirming the earlier results from CCA.

To see how this evolution contrasts with the canonical ENSO evolution found during the latter half of the 20th century, we performed the same analysis for the period 1960-2011 (Figure 7). As expected, during this period, there are coherent oceanic and atmospheric signatures in the tropics during Boreal winter (Jan(-1)/Apr(-1) prior to mature El Niño events that qualitatively match those from the earlier CCA results. In addition, there is also a relation between El Niño events and prior La Niña events. However, the transition between La Niña events and El Niño events during this period is

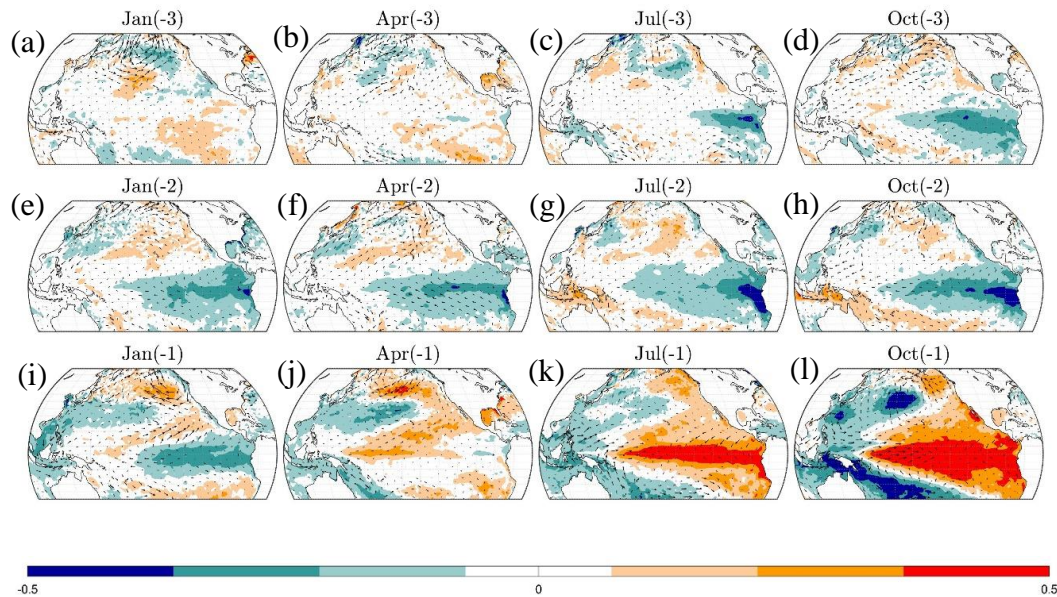


Figure 7. Same as Figure 6 except for the period 1960-2011.

shorter. Further, the persistence of the La Niña state spans a broader period of time (from Oct(-3) to Oct(-2)), suggesting that the length of the transition time is less well defined, ranging from 1 to 2 years. As such, in addition to the changing nature of the precursor fields prior to mature ENSO events, these two figures suggest that the periodicity of the ENSO system may have shifted between the two intervals.

In order to quantitatively test this hypothesis, we calculate the Power Spectral Density (PSD) of the seasonal Niño3.4 index for the two subintervals separately using Thomson's multitaper technique (Figure 8). During 1960-2011 the PSD presents several minor peaks, but generally the spectrum sees a plateau for periods of roughly 2 years up to 5 years. As such, during the period 1960-2011, the ENSO signal is characterized by a diverse range of frequencies with no distinct period of oscillation. This confirms the interpretation of the long-lived transition from La Niña states to El Niño states seen in Figure 7, which in fact captures transitions with different periods being averaged together

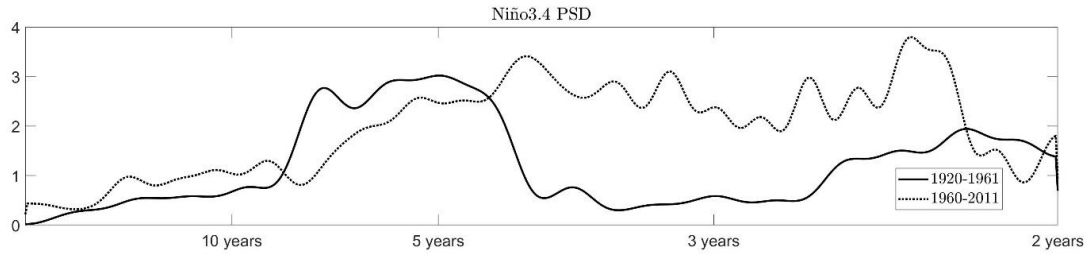


Figure 8. Power Spectral Density (PSD) of the seasonal (NDJ) Niño3.4 index. The PSD is calculated using Thomson’s multitaper method. On the x-axis frequency from low to high (logarithmic scale), with ticks designating the corresponding period; on the y-axis the amplitude ( $K^2/(\text{cycles}/\text{year})$ ). The PSD is calculated and shown for the intervals: 1920-1961 (black thick line), 1960-2011 (dotted line).

in the lag-regression calculation. By contrast, the power spectrum for the 1920-1961 interval shows a narrow band of power at longer periods. The more confined periodicity of ENSO mirrors the well-defined shift between La Niña and El Niño seen in Figure 6. Further, the longer periods—roughly between 4 and 8 years—correspond with the slower, 3-year transition from La Niña events to El Niño events (equivalent to a 6-year period) of the lag-regression fields in Figure 6.

As a final check of the strongly oscillatory nature of the ENSO evolution during the period 1920-1960, we performed an analysis similar to that in Figure 6 but for the 36 months following the NDJ Niño3.4 index (Figure 9). In agreement with Figure 6, the



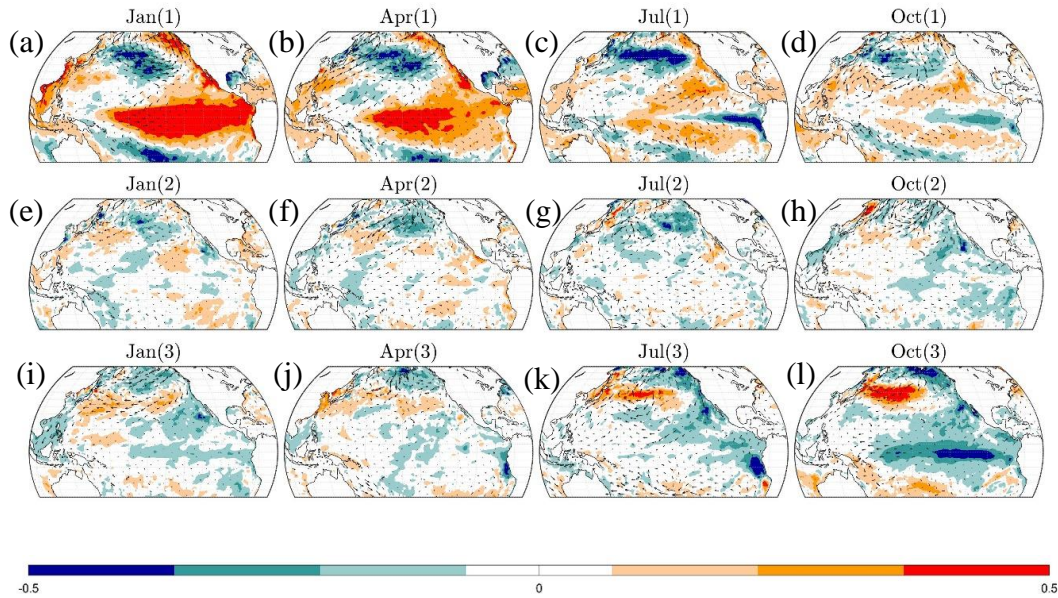


Figure 9. Same as Figure 6 except for the 36 months following the normalized, seasonal (NDJ) Niño3.4 index.

transition between opposite ENSO states takes 3 years and there is no significant oceanic or atmospheric anomalies during the intervening months (with the exception of a weak La Niña-like pattern the year following a mature El Niño, which corresponds with the minor 2-year peak in the power spectrum in Figure 8).

To summarize this suite of results discussed above we use the Morse wavelet transform on the Niño3.4 index to study the changing evolution of the spectrum of the ENSO signal over the full interval (Figure 10). It is clear that during the first and last intervals (1870-1920 and 1960-2011, respectively) during which the TWC/NPMM-ENSO relation is robust, the Niño3.4 evolution tends to have shorter periodicity centered on the 2-4 year range; during the last interval the range of periodicity becomes even broader and extends into the 4-6 year range, as seen in Figure 8. By contrast, in the middle interval in which the TWC/NPMM-ENSO relation is absent, the power of the



signal is concentrated over a much narrower band of longer range periodicities, between 5-7 years with a local maximum at around 6 years, again in agreement with Figure 8 (as well as the lead/lag regression maps shown in Figure 6 and Figure 9 respectively).

Further, during this period in which the TWC/NPMM forcing (or any other wind-stress forcing for that matter) is absent there is also an almost complete absence of power at the shorter 2-4 year periods that is predominant during the other two intervals when TWC/NPMM forcing is more robust. These results highlight that the decadal modulation of coupling between ENSO and preceding zonal wind stress anomalies (whether NPO-related or not) align with decadal changes in ENSO's periodicity and suggest that the

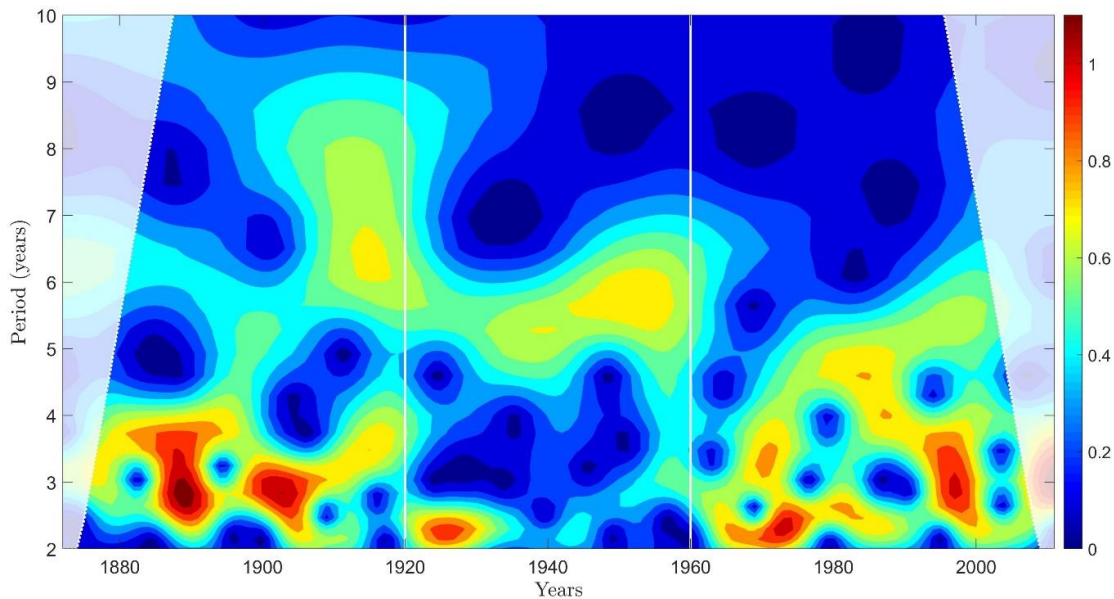


Figure 10 Continuous Morse wavelet transform (CWT) of the seasonal (NDJ) Niño3.4 index for the full 1870-2011 time interval. On the x-axis is the year, on the y-axis is the period (in years). The white dashed lines set the boundary of the cone of influence, which is shaded in white. The white vertical lines, at 1920 and 1960, divide the full time period into the 3 sub-intervals identified by PC1(t) in Figure 2c. Magnitude of spectral power ( $K^2$ ) at a given year/period is designated by the color bar on the r.h.s of the figure.

nature of ENSO variability may change based upon the efficacy of forcing mechanisms during particular periods (to be discussed further below).

### **Summary and Conclusion**

In this paper we analyze the empirical relation between mature ENSO events and preceding wind-stress variability using a newly updated multi-century ocean reanalysis, namely the SODAsi.3 dataset. An initial analysis of the last 50 years of the SODAsi.3 dataset (1960-2011) confirms there is a strong coupling between mature ENSO events and the strength of the trade winds in the tropical North Pacific. This wind-stress variability in the northern trades is known to both generate a Trade-Wind Charging (TWC) of the equatorial subsurface temperatures and to establish the North Pacific Meridional Mode (NPMM) tropical sea-surface temperatures. As such, here we refer to this precursor pattern as the TWC/NPMM forcing mode of wind-stress variability. We then extend the analysis to cover the entire interval from 1871 to 2011. Over the longer time interval, our analysis shows a non-stationarity in the efficacy of the TWC/NPMM forcing of the ENSO system. In particular, the intervals of roughly 1871-1920 and 1960-2011 show similar results: the NPO-related TWC/NPMM forcing mode consistently precedes ENSO by a full year. However, for the interval between 1920 and 1960 the TWC/NPMM forcing mode does not represent a robust precursor to mature ENSO events a year later. Moreover, our analysis reveals that, during this intervening interval, in fact no mode of wind-stress variability is found to significantly precede ENSO events.

Equally important, this non-stationarity in the TWC/NPMM forcing mechanism is mirrored by a shift in the characteristics of ENSO itself. Namely, during both the first and

the last sub-interval, the power of the Niño3.4 index is distributed over a wide range of relatively high frequencies, having periods from roughly 2 up to 5 years. In contrast, for the interval 1920-1960, the power of the signal is concentrated in a narrower band of lower frequencies centered on periods of 6-7 years. In addition, during this interval, there is a distinct lack of power in the 2-5 year range that predominates during the other two intervals. This result refines earlier findings on the frequency ranges of the Southern Oscillation (SO). In particular, (Yiou, et al., 2000) identified a shift in the frequency of the SO Index between 1961 and 1962. While (Wang and Wang 1996), using data extending to 1872, reported two changes: in the 1910's and 1960's.

We argue here that these results suggest that the spectral change is a sign that the dynamics of the ENSO system itself is non-stationary. As argued by (Wang, et al., 2017), ENSO can be interpreted within two theoretical frameworks: either as a self-sustained oscillation, or as a mode triggered by stochastic forcing. Our results suggest that, during the last 140 years, ENSO has shifted between these two underlying dynamics. In particular, the diverse range of frequencies that we see during those phases in which TWC/NPMM forcing is an active precursor—i.e. 1871-1920 and 1960-2011—would imply that the system is responding to stochastic forcing. During the phase in which there is no apparent atmospheric precursor present—i.e. 1920-1960—the ENSO power of the signal is concentrated in a narrow, low-frequency band which implies that the ENSO system is behaving as an un-triggered, self-sustained oscillation. As previously mentioned, this interpretation of our results confirms previous findings from Yu and Fang (2018). Their study argues that the SF mechanism - equivalent to TWC/NPMM

characterized in this chapter - is responsible for a stochastic evolution of the ENSO system, while the recharge-discharge mechanism drives a more regular oscillation. Furthermore, their analysis, which focuses on the interval 1958-2014, identifies an enhanced influence of the TWC/NPMM upon ENSO, consistent with the latter period identified here. That said, our results put their results in larger historical context and suggest that such multi-decadal modulation of the influence of TWC/NPMM upon ENSO has been on-going over much longer, centennial timescales.

Further, our analysis reveals the intrinsic frequency of the observed oscillatory ENSO mode. While Yu and Fang (2018) are able to only analyze one such mechanism for generating this intrinsic oscillation - the recharge-discharge mechanism - the self-sustained ENSO that we identify during the interval 1920-1960 could actually be described by one of the four different conceptual mechanisms comprising the unified oscillator: the delayed oscillator, the western Pacific oscillator, the recharge-discharge oscillator, and the advective-reflective oscillator (Wang, 2001). However, as we show in this paper, the oscillation between 1920 and 1960 is slow, with a period of 6-7 years of length. This means that, among the aforementioned mechanisms, three are unlikely to provide a comprehensive description of the dominant observed oscillatory mode because the oscillations they explain are much faster. The western Pacific oscillator has, in fact, a period of around 4 years (Weisberg and Wang 1997); the recharge-discharge oscillator is described to have a robust period of about 3-5 years (Jin (1997); Yu and Fang (2018)), and the delayed oscillator generates ENSO cycles of 2-4 years of length (Suarez and Schopf 1988). The advective-reflective oscillator, however, gives rise to ENSO cycles

having periods as long as 6 years (Picaut, et al., 1997), and it could therefore provide a framework to contextualize the signal during the 40-year interval when ENSO shows the most robust oscillatory behavior.

To conclude, different characteristics of ENSO diversity have been studied throughout the years. Examples include the geographic structure of ENSO events as captured by the duality between Central Pacific (CP) and Eastern Pacific (EP) ENSO, as reviewed by Timmermann, et al. (2018). The diversity of ENSO's time evolution has also been the subject of previous studies. For instance An & Wang (2000) argue that from the 1960's to the 1990's ENSO variability shifted from a 2-4 year periodicity to a 4-6 year periodicity. In addition, Atwood, et al. (2017) identified multi-decadal changes in the frequency of the ENSO signal within very long (4000 years) runs of GFDL's coupled climate model. Here, thanks to the length of the SODAsi.3 dataset, we have unveiled another aspect of ENSO: a slow, multi-decadal change in ENSO frequency characteristics that implies an underlying change in ENSO dynamics from one triggered by stochastic forcing to one maintained by self-sustained oscillations. Both the possible causes and the implications of this shift in underlying dynamics need to be further investigated. It is important to analyze which multidecadal changes might be modulating the TWC/NPMM-ENSO relationship. A starting point may be recent articles by Chen et al. (2019) and Chen, et al. (2013) arguing respectively that the Atlantic Multidecadal Oscillation and the Arctic Oscillation modulate the strength of the NPO influence on ENSO. Understanding how the dynamical changes came about around 1920 and 1960 could help us predict if similar shifts could occur again in the future. Further, by isolating this period and

identifying the mechanism(s) underlying the self-sustained oscillation, we can determine whether and how such mechanisms are affected by other factors, including climate change, thereby gaining a deeper understanding of how ENSO may vary in the future.

## CHAPTER THREE

### Introduction

The El Niño Southern Oscillation (ENSO), as one of the most impactful modes of interannual climate variability, is responsible for significant variations in temperature, precipitation and pressure patterns across many regions of the world. ENSO has been found to impact large-scale circulations in the Tropics (Rasmusson and Carpenter 1982) and to carry consequences for weather patterns reaching far beyond the Tropical Pacific (Alexander, et al. 2002; Dai and Wigley 2000; Ummenhofer, Kulüke and Tierney 2018). The mechanisms characterizing this climate mode have been the focus of a large body of literature and many aspects are still under investigation.

Among the different features of ENSO that are still being investigated, of particular interest are its potential driving mechanisms. The reason behind this interest lies in the possibility to predict the occurrence of ENSO events in a timely manner by tracking the behavior of such drivers. This type of information is particularly important for those regions and communities where the impacts of ENSO are more strongly felt. In this work, we focus on a specific set of drivers for ENSO, i.e. the atmospheric circulation anomalies related to the North Pacific Oscillation (NPO) (Anderson 2003; Chang, et al. 2007). During a positive NPO phase, sea-level pressure (SLP) anomalies weaken the subtropical high in the northern portion of the Pacific Ocean, thus reducing the strength of the off-equatorial easterly trade winds. These westerly anomalies carry both a dynamic and thermodynamic impact. In the former case, the dynamic impact of the westerly anomalies is a direct consequence of the wind stress that causes vertically-integrated

meridional mass transport into the central portion of the Equator. The convergence of warm water in the subsurface puts the equatorial Pacific in a “charged” state which is an established initiator of El Niño events (Anderson and Perez 2015). This process is referred to as Trade Wind Charging (TWC). In the latter case, the weakened trades reduce the loss of latent heat due to evaporation in the underlying waters, inducing warm sea surface temperature (SST) anomalies in the extra-tropics. This anomaly is referred to as the Pacific Meridional Mode (and we will refer to it as the Northern Pacific Meridional Mode or NPMM) (Chiang and Vimont 2004; Amaya 2019). Three hypothesized mechanisms connect the NPMM to the onset of ENSO through the formation of equatorial Kelvin waves that propagate along the thermocline and initiate El Niño events (Amaya, Kosaka, et al. 2019; Liu and Xie 1994; Alexander, et al. 2010; Thomas and Vimont 2016). Since the TWC and NPMM consistently precede ENSO events by 9-10 months (Anderson 2003; Vimont, Battisti and Hirst 2001), variations in these two drivers will be treated in concert and will be referred to as TWC/NPMM henceforth. That said, recent analysis of the observed relationship between ENSO and the TWC/NPMM precursor showed that it is non-stationary (Pivotti and Anderson 2021) such that during particular multi-decadal periods the coupling is robust, however during others it weakens considerably. Further, during the periods of weak TWC/NPMM-ENSO coupling, the oscillatory nature of ENSO variability becomes stronger, while during periods of robust coupling ENSO acts more like a stochastic process (Pivotti and Anderson 2021).

Given these variations in the robustness of the TWC/NPMM-ENSO coupling and its apparent influence on ENSO characteristics in historical data, we want to investigate



whether similar behaviors are seen in state-of-the-art coupled climate models. Over the years, models have refined their ability to simulate climate processes and modes, including ENSO and its precursors. For example, in (Bellenger, et al. 2014), the authors compare the third and fifth generation of the Coupled Model Intercomparison Project (CMIP) on their general ability to reconstruct ENSO, its characteristics and the physical processes that enable its cycle. The paper shows general, ensemble-wise, improvements between generations, with wide intra-ensemble variations and suggestions for further improvements (Bellenger, et al. 2014). A recent paper by (Planton, et al. 2021) compares CMIP6 and CMIP5 performance in reconstructing ENSO over a series of 24 metrics from the CLIVAR 2020 ENSO protocol, and documents significant improvements in a third of such indicators. In particular, CMIP6 showed reduced biases both in the tropical Pacific mean, as well as the seasonal cycle, plus it showed improvements in the reconstruction of ENSO patterns, its diversity, and remote teleconnections.

In this study, we join this common effort and evaluate the ability of a CMIP6 ensemble to recreate specific features of the relationship between ENSO and its TWC/NPMM precursor. In particular, we use a model ensemble from the latest CMIP6 framework (Eyring, et al. 2016), which is specifically designed to systematically investigate the role of increased horizontal resolution on model performance, called High Resolution MIP (HighResMIP (Haarsma, et al. 2016)). In particular, previous studies have shown either a consistent reduction of biases when the horizontal resolution increases (Liu, et al. 2018; Wengel, et al. 2021) while others indicate that effects are not homogeneous, for instance across latitudes (Roberts, et al. 2020).. The question on the

impacts of a resolution increase is still open because it results from intervening factors. For instance, an increase in horizontal resolution could improve the simulation of the dynamics of a mode directly; provide a more faithful reconstruction of the background state, thus reducing systematic and long-standing models' biases (Roberts, et al. 2019; Kinter III, et al. 2013); or determine whether SSTs are driven by air/sea interactions or ocean dynamics (Small, et al. 2020). This last factor in particular could mean that horizontal resolution might play a role in the variability of the TWC/NPMM-ENSO relationship. For this reason, we include models with both standard and enhanced resolution from the HighResMIP ensemble to investigate the relationship between ENSO and its NPO-related drivers..

The study is organized as follows. First, we seek to understand whether the TWC/NPMM is reconstructed as a driving mechanism for ENSO across the models. Then, we evaluate how the members of the ensemble reconstruct the characteristic features of the TWC/NPMM. Secondly, we study the relationship between these two modes, and their respective and coupled internal variability. This step will mirror a recent study based on a long ocean reanalysis (Pivotti and Anderson 2021). Across the study, we are going to monitor whether and how changes in horizontal resolution might affect model performance in the context of the TWC/NPMM-ENSO relationship.

## **Data and Method**

### *Data*

The variables used in this analysis are sea surface temperature (SST) and horizontal wind stress ( $\tau_X$  and  $\tau_Y$ ). They are obtained from the control runs of 6 models

taking part in the High Resolution Model Intercomparison Project (HighResMIP) within the CMIP6 protocol, which is described in details in Haarsma, et al. (2016). The experiments we utilize, called control-1950, are simulations of about 100 years length, with prescribed constant radiative forcing conditions, at the average levels of the 1950's, corresponding to a global radiative forcing of  $\sim 0.5 \text{ W/m}^2$  (Myhre, et al. 2013). In this common HighResMIP protocol, each model runs at least two experiments with different horizontal resolutions, where either the oceanic or the atmospheric (or in some cases both) resolution changes. One of the institutions included in this study also provides an intermediate resolution configuration. The details of the models, the institutions running the experiments and their specific resolutions are shown in Table 1. There one can see that both the changes and coarseness of the resolutions vary widely across the ensemble. For example, the lower oceanic resolution of a model (CMCC LR, 25km) can be finer than the high resolution of another (MPI HR, 40km). Therefore, we do not group experiments as low resolution and high resolution ones, but we keep the comparisons between resolutions of the same institution. To simplify visual comparisons, we thus name the experiments as “name of the institution + relative resolution”, where the relative resolution is either LR, MR or HR.

The model ensemble is checked against the latest version of the Simple Ocean Data Assimilation reanalysis with sparse observation input: SODAsi.3 (Giese, et al. 2016; hereinafter SODA). In this version: (1) the only oceanic observations assimilated are SSTs; (2) the assimilation follows a 10-day long update cycle through a loosely coupled set of iterations between the SODA system for oceanic data and atmospheric boundary

conditions from the 20th Century Reanalysis (20CRv2c); and (3) SODA is forced with individual ensemble members from 20CRv2c. Time wise, we consider the interval 1960-2011, in order to compare the model ensemble against the years when the TWC/NPMM mechanism is known to be active (Anderson and Perez 2015; Larson and Kirtman 2014).

Institution	Model ID	Ocean Res (km)	Atm Res (km)	Name	Reference
CMCC	CMCC-CM2-HR4	25	100	CMCC LR	(Scoccimarro, Bellucci and Peano 2018)
	CMCC-CM2-VHR4	25	25	CMCC HR	(Scoccimarro, Bellucci and Peano 2018)
CERFACS	CNRM-CM6-1	100	100	CNRM LR	(Voldoire 2019)
	CNRM-CM6-1-HR	25	50	CNRM HR	(Voldoire 2019)
MPI	MPI-ESM1.2-HR	40	100	MPI LR	(von Storch, Putrasahan, et al. 2018)
	MPI-ESM1.2-XR	40	50	MPI HR	(von Storch, Putrasahan, et al. 2018)
ECMWF	ECMWF-IFS-LR	100	50	ECMWF LR	(Roberts, Senan, et al. 2018)
	ECMWF-IFS-MR	25	50	ECMWF MR	(Roberts, Senan, et al. 2018)
	ECMWF-IFS-HR	25	25	ECMWF HR	(Roberts, Senan, et al. 2017)
EC-Earth	EC-Earth3P	100	80	EC-Earth LR	(EC-Earth Consortium 2019)
	EC-Earth3P-HR	25	40	EC-Earth HR	(EC-Earth Consortium 2018)
MOHC	HadGEM3-GC31-LL	100	250	HadGEM3 LR	(M. Roberts 2017)
	HadGEM3-GC31-HM	25	50	HadGEM3 HR	(M. Roberts 2017)

Table 1 Details of the HighResMIP ensemble

### *Method*

For this analysis, we combine a method that has been used before to isolate correlated modes of climate variability (Anderson 2003) with techniques specifically designed for multi-model inter-comparisons.

First, for each experiment, SST and  $\tau_x$ , are constrained spatially and temporally. Since the area of interest is the Tropical Pacific where ENSO is active, we focus on the portion of ocean between latitudes 20S and 20N and longitudes 120E and 70W, similarly to what was done in (Anderson and Perez 2015; Larson and Kirtman 2013). Temporally, the variables are detrended and averaged over the months when ENSO and TWC/NPMM are respectively most active: November-January for SST (Trenberth 1997) and November-February for  $\tau_x$  (Anderson and Perez 2015). As ENSO and TWC/NPMM have a 1-year lag (Anderson 2003), the space-time matrices of the two variables are lagged accordingly.

Then, we apply the Canonical Correlation Analysis (CCA) in the basis of Principal Components (PC's) (Bretherton, Smith and Wallace 1992) to extract highly correlated modes of variability from the variables. The first step consists of an Empirical Orthogonal Function analysis, applied to the lagged seasonal means. Through this method, which has been widely used in climate research (Dai, et al. 2015; Kessler 2001), we are able to identify and extract the modes that carry the highest winter variability for each variable. These modes are returned, in decreasing order of variance, in time series called Principal Components (PC's). At this point, we apply the CCA on such PC's (the basis of PC's), one subset for each variable. The CCA returns pairs of time series called

Canonical Variables (CV's), in this case one for SST and one for  $\tau_x$ , that are sorted in a way such that the first pair represents the  $\tau_x$  and SST modes having the highest (lagged) correlation. The amount of PC's included in the CCA are selected recursively for each experiment, by maximizing the correlation between the leading CV's. The selection is done with the trade-off of including not more than 85% of each variable's variance, following the guidelines of (Bretherton, Smith and Wallace 1992). Furthermore, we exclude the zonal wind stress PC that is most highly correlated to ENSO. In doing so we ensure that the wind mode isolated by the corresponding first CV is independent from ENSO (Larson and Kirtman 2014). The PC of  $\tau_x$  that captures the ENSO signal is identified as the time series that has the highest correlation with the concurrent Niño3.4 index; in some models this corresponds to the first PC, in other models to the second.

The methods described here are outlined in a recent paper that used them to reconstruct the TWC/NPMM wind fields in SODA as a way to model their influence on ENSO variability (Chakravorty, et al. 2020). They are also described in another paper (Pivotti and Anderson 2021) which uses them to analyze in depth the observed relationship between ENSO and the TWC/NPMM precursor over the last 140+ years.

Once the CCA in the basis of PC's returns the leading CV's, we use these time series to reconstruct the corresponding maps of SST and  $\tau_x$ . In order to gather an initial understanding of model performance we analyze such maps with a tool designed for model ensemble analyses: the Taylor diagram. This method, thoroughly described in (Taylor 2001), is meant to provide a comprehensive picture of the spread of an ensemble, with respect to a reference point. In particular, the Taylor diagram is designed to show:

(1) the deviations of model results from the observations in the metric of the root mean squared difference (RMSD), and (2) whether such low (high) value for the RMSD are due to high (low) correlation or to a small (large) difference in their respective standard deviations. In our case, we apply this technique to the reconstructed maps of the ensemble members, against the same map created with observationally-based SODA reanalysis. Since all these quantities are calculated on spatial domains, the 2-d maps are first converted to vectors before calculating the standard deviation across all the grid points in the domain.

## Results

The CCA in the basis of PC's is applied to all 13 experiments. As described in the previous section, the analysis returns pairs of time series (named canonical variables CVs), one for SST and one for  $\tau_X$ . Among them, we select the first pair:  $CV^1_{\tau_X}(t-1)$  and  $CV^1_{SST}(t)$ . It is important to remember that these coupled time series are by definition the most highly correlated, and by construction they have a one year lag.  $CV^1_{\tau_X}(t-1)$  and  $CV^1_{SST}(t)$  are then used to reconstruct their corresponding spatial patterns, shown respectively in Figure 11 and Figure 12, together with the same reconstruction carried out on the SODA reanalysis. We reconstruct the maps by regressing each time series against the space-time matrices of their respective concurrent variable anomalies that were previously normalized by their standard deviation at each grid-point. In Figure 11,  $CV^1_{\tau_X}(t-1)$  is utilized to reconstruct the maps of  $\tau_X$  anomalies. These maps, by construction, precede by one year the SST maps of Figure 12, where the regression is carried out against  $CV^1_{SST}(t)$ . Starting with the observational results obtained for SODA,

we see the positive, westerly anomaly in the northern extra-tropics (Figure 11a) that is the signature of the TWC/NPMM preceding a clear positive ENSO with strong positive SST anomalies in the central and eastern portion of the tropical Pacific (Figure 12a). From the maps reconstructed for the 13 experiments it is clear that our method captures the same modes as in SODA across the ensemble: in Figure 11(b-n) they all show, with some variations, the westerly anomaly of the TWC/NPMM and in Figure 12(b-n) positive SST anomalies that can be ascribed to a positive ENSO event. The TWC/NPMM-ENSO is therefore the strongest lagged coupling between winter modes of SST and wind stress variability across the ensemble. The reconstructions of the state of the ocean one year prior to El-Nino event, identified by regressing  $CV^1\tau_x(t-1)$  against both components of horizontal wind stress and SST indicate a south-westerly direction in the off-equatorial wind anomaly over the North Pacific, and positive SST anomalies underneath it (not shown), signatures of the TWC and the NPMM component respectively in both the HighResMIP models and in the SODA reanalysis.



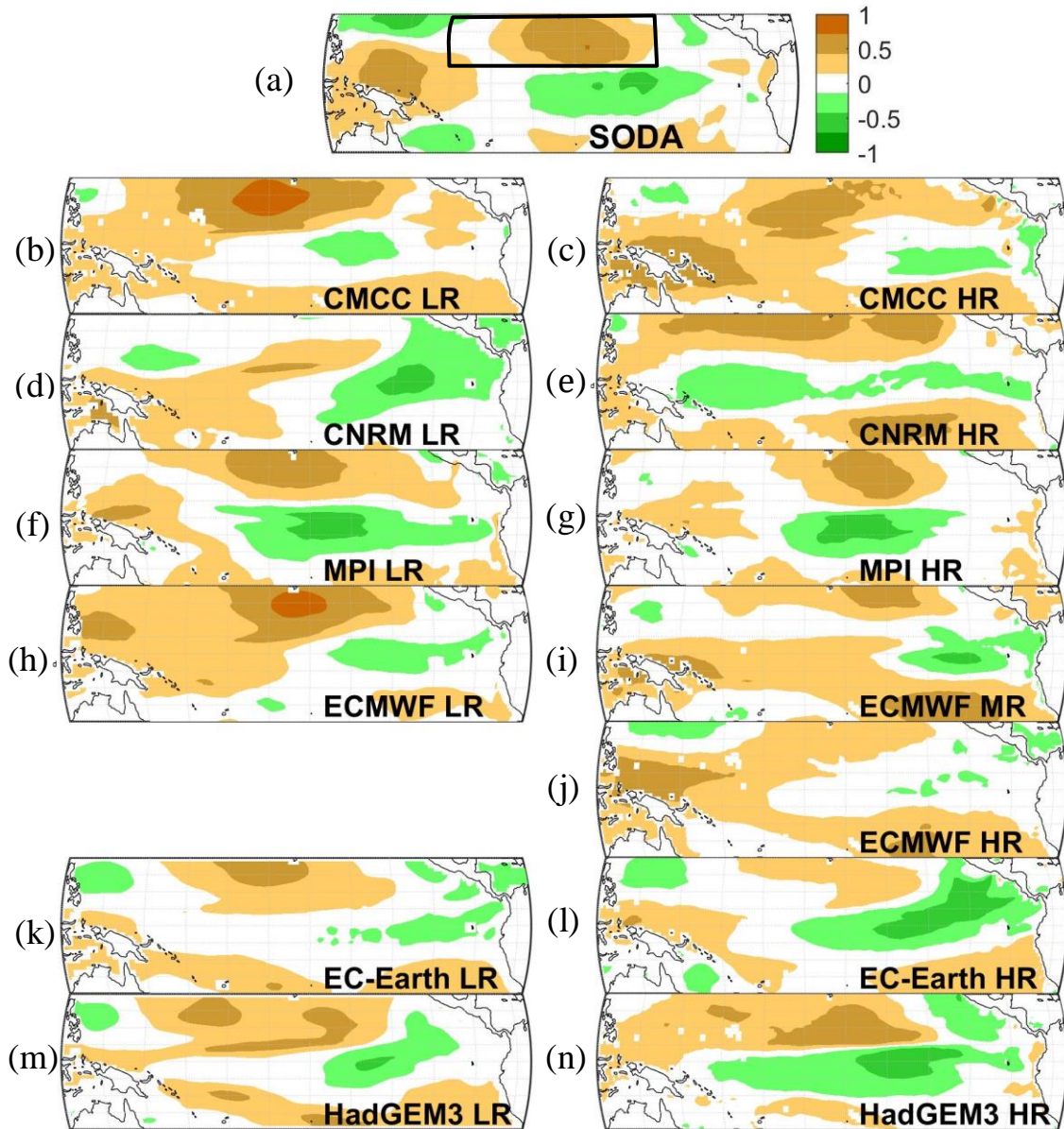


Figure 11 Maps of normalized zonal wind stress ( $\tau_x$ ) anomalies regressed against the first Canonical Variable of  $\tau_x$ :  $CV^1\tau_x(t-1)$ .

(a) results obtained on the SODA reanalysis data,  $\tau_x$ TWC in black.

(b-n) results for the ensemble, where each experiment is referred to by the acronym in Table 1. Positive (negative) values are shaded in brown (green). Magnitude of normalized  $\tau_x$  (unitless) are given by the color bar on the r.h.s of panel (a)

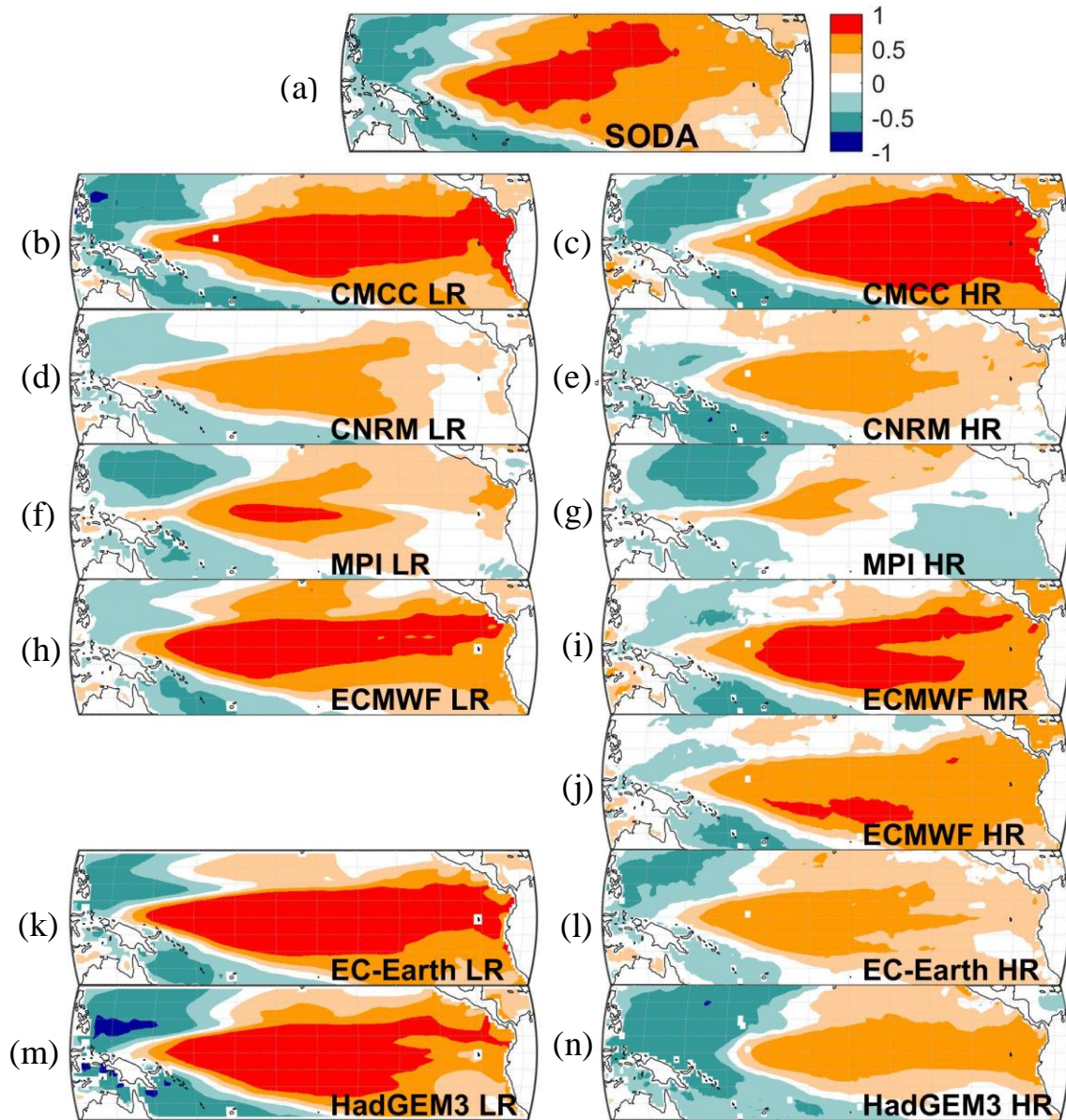


Figure 12 Maps of normalized SST anomalies regressed against the first Canonical Variable of SST:  $CV^1_{SST}(t)$ .

(a) results obtained on the SODA reanalysis data

(b-n) results for the ensemble, where each experiment is referred to by the acronym in Table 1. Positive (negative) values are shaded in red (blue). Magnitude of normalized SST (unitless) are given by the color bar on the r.h.s of panel (a)

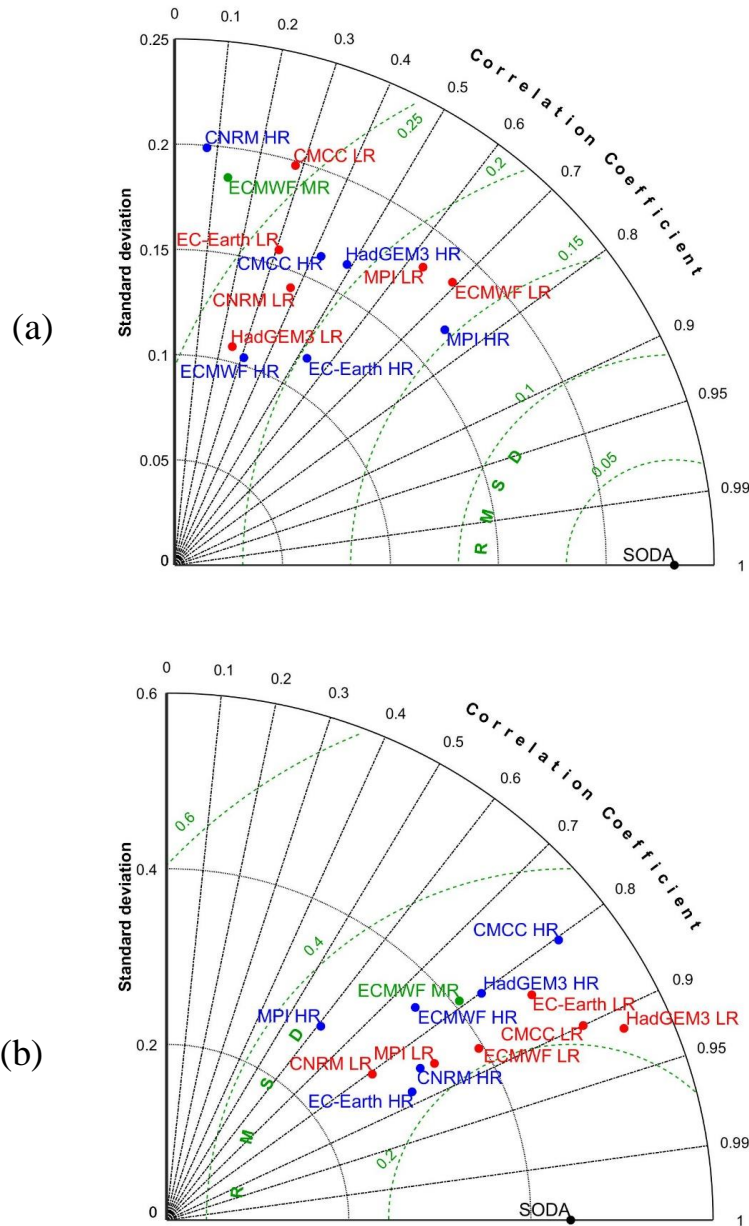


Figure 13 Taylor Diagram comparing the ensemble members against SODA (black dot). The correlation coefficients, standard deviations and root mean squared differences (RMSD green dashed lines) are calculated over (a) the 5N - 20N, 165E - 240E domain of zonal wind stress anomaly maps  $\tau_x TWC$  as shown in Figure 11a; (b) the sea surface temperature anomaly maps shown in Figure 12. In red the experiments at low resolution (LR), in green mid-resolution (MR), and in blue high resolution (HR). Correlation values below 0.15 are not significant at 95% confidence.



Figure 11 and Figure 12 provide us with a first overview of how the model simulations are isolating ENSO and preceding winter wind stress modes. At this point, we analyze these results with the help of a Taylor diagram to gain a deeper insight into how the reconstructions differ, with respect to the SODA reanalysis data and between different resolutions of the same model. Among the three variables that characterize the TWC/NPMM mode (SST,  $\tau_X$  and  $\tau_Y$ ), we select  $\tau_X$  for the Taylor Diagram because its positive anomaly represents the characteristic signature of the mechanism. Furthermore, since the zonal wind anomaly is generally found in the central portion of the northern extra-tropics, we isolate the domain 5N - 20N, 165E - 240E (shown as a black square in

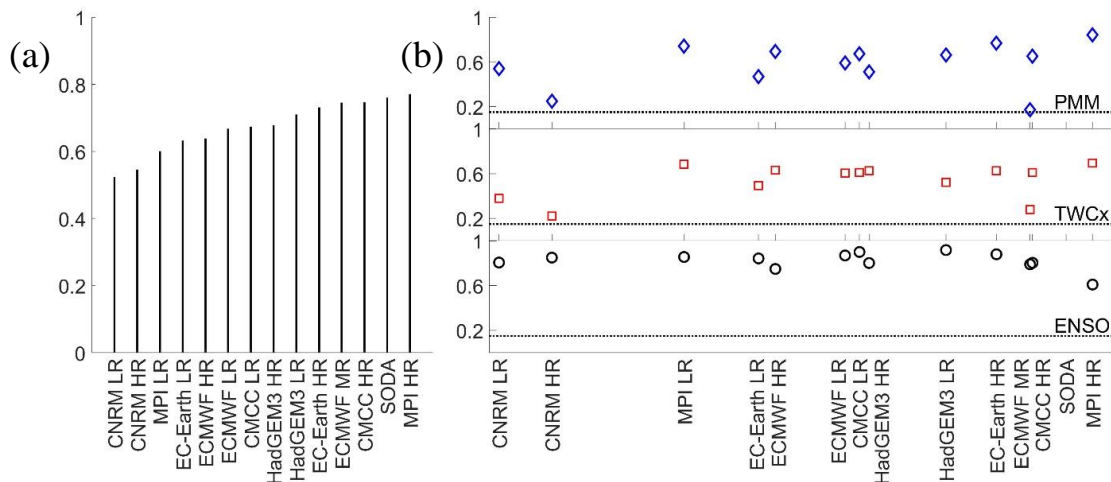


Figure 14

(a) Correlation values between the first pair of canonical variables  $CV^1_{SST}(t)$  and  $CV^1_{\tau_X}(t-1)$ . The experiments (+ SODA) are sorted along the x-axis in increasing order of correlation value.

(b) Scatter plot. On the x-axis the correlation values between  $CV^1_{SST}(t)$  and  $CV^1_{\tau_X}(t-1)$  from panel (a) with the name of their respective experiments, on the y-axis values of pattern correlation ( $\rho$ ) between each ensemble member and SODA.

The features analyzed are, in order: PMM (blue), maps of normalized SST anomalies regressed against  $CV^1_{\tau_X}(t-1)$  (not shown); TWC<sub>x</sub> (red), maps of normalized  $\tau_x$  anomalies regressed against  $CV^1_{\tau_X}(t-1)$  from Figure 11; ENSO (black), maps of normalized SST anomalies regressed against  $CV^1_{SST}(t)$  from Figure 12.

Interval of 95% confidence at  $\rho = \pm 0.15$  (dashed lines at 0.15).

Figure 11a) in the maps of zonal wind stress from Figure 11 . These new maps, that we call henceforth  $\tau_x$ TWC, are then used to calculate the Taylor diagram, which is shown in Figure 13a.

The position of the SODA results, in the bottom-right portion of the plot, indicates a perfect representation of the observed pattern. One can see how the results of the ensemble spread across the quadrant, by following the increasing values of RMSD along the green circles and the decreasing values of correlation coefficients counterclockwise following the black lines. In particular, we can see the experiment situated closer to SODA, namely MPI HR, has the highest correlation and lowest RMSD - and from there, follow how the experiments are distributed. The way to interpret this diagram is by observing how the experiments are positioned according to the three indicators, among which the main indicator to monitor is the RMSD. The color coding, red for low resolutions, blue for high and green for mid-resolution, makes the results easier to interpret. From this first evaluation, it appears that the resolution does not have a consistent impact on the models' ability to reconstruct the TWC/NPMM mechanism. For 4 out of 6 models, the experiment at high resolution performs better than the one at low resolution: MPI HR has lower RMSD and higher correlation coefficient than MPI LR, and similar differences hold true in the cases of EC\_Earth, HadGEM3 and CMCC. The opposite is instead true for the remaining 2 models (CNRM and ECMWF). Analogously, when we analyze the ENSO patterns from Figure 12 with a Taylor diagram (Figure 13b) we notice that the resolution does not play a consistent role in this case either. Here, 4 out of 6 models perform better at a lower resolution, specifically: MPI, ECMWF, HadGEM3

and CMCC. To better assess the impact of resolution we binned simulations together in different ways. In particular, we looked at the change in resolution in three ways: (1) comparing between regular and increased resolutions of each institution; (2) separating between the models where the increase happens in the ocean and/or atmosphere; (3) looking across the ensemble at models with similar resolutions. However, across all these groupings, the results of our analysis do not show a consistent shift in model performance. Therefore, we decided to keep the simulations grouped according to institution for the rest of the analysis. The ensemble spread for the reconstructions of ENSO is more compact and shows higher correlation values than for the reconstructions of the zonal wind stress anomaly of TWC ( $\tau_X$ TWC). Specifically, the values are within the [0.6, 0.95] and [0, 0.8] intervals respectively. It is important to note that only correlation values  $\rho > 0.15$  are significant at a  $\alpha = 0.95$  level, which means that the correlation values for  $\tau_X$ TWC are not significant in the cases of CNRM HR and ECMWF MR. The values of RMSD are instead on average higher for ENSO than for  $\tau_X$ TWC, within the ranges [0.2, 0.4] and [0.15, 0.3] respectively, due to higher standard deviation values both for the models and for SODA.

The CCA in the basis of PC's shows us the strength of the coupling, recorded by the correlation between the first canonical variables  $CV^1_{\tau_X(t-1)}$  and  $CV^1_{SST(t)}$ . These values are shown in Figure 14a where the experiments are ranked with increasing correlation. Once again, the horizontal resolution does not appear to have a consistent influence on how the experiments perform. This ranking is used to carry out a further check on the spread of the ensemble. Since the TWC/NPMM precursor has two separate

components - the SST and  $\tau_x$  anomalies - in Figure 14b, we show how the ensemble performs in reconstructing the full fields (20S - 20N and 120E - 70W) of: (1) the PMM as the fields of normalized SST anomalies regressed against  $CV^1\tau_x(t-1)$ ; and (2) the maps of normalized zonal wind stress anomalies also regressed against  $CV^1\tau_x(t-1)$  (TWCx in the legend). We also include the reconstruction of normalized SST anomalies regressed against  $CV^1_{SST}(t)$  (ENSO in the legend) to provide a more complete picture of the ensemble spread. Similar to what was done for the Taylor diagram, the experiments are compared to the results obtained from SODA by calculating how their respective reconstructed maps spatially correlate. These values are plotted against the correlation values of Figure 14a on the x-axis. This comparison shows us once again that the reconstruction of the ENSO pattern is consistently good across the ensemble, while the reconstructions of both NPMM and TWCx are better for those experiments that also have a stronger TWC/NPMM-ENSO coupling, hence higher correlation values between  $CV^1\tau_x(t-1)$  and  $CV^1_{SST}(t)$ . Furthermore, as we saw in Figure 13, the correlation values for ENSO are higher and within a fairly narrow interval ([0.61, 0.92]), especially when compared to the spread of the values for both TWCx and NPMM ([0.22, 0.69] and [0.17, 0.84] respectively).

As outcome of this first set of analyses, we select a group of better-performing models and further analyze them below. Since, as we noted before, there is little variation in how well the experiments reconstruct ENSO, we separate the experiments according to their ability to reconstruct the TWC/NPMM precursor. Specifically, we average between the correlation values for TWCx and PMM, against SODA's spatial patterns, and we

select the experiments for which this value is equal to or greater than 0.6 (the average value of these means). There are 7 such better-performing models and they are highlighted in bold in Table 2 where the correlation values with respect to SODA of all models are listed (columns 2-4).

Name	$\rho(\text{Niño}3.4, \text{CV}^1_{\text{SST}})$	TWC <sub>x</sub>	NPMM	Mean
<b>CMCC LR</b>	0.94	0.61	0.67	<b>0.64</b>
<b>CMCC HR</b>	0.90	0.61	0.65	<b>0.63</b>
CNRM LR	0.54	0.38	0.54	0.46
CNRM HR	0.59	0.22	0.25	0.23
<b>MPI LR</b>	0.63	0.68	0.74	<b>0.71</b>
<b>MPI HR</b>	0.25	0.69	0.84	<b>0.77</b>
<b>ECMWF LR</b>	0.78	0.60	0.59	<b>0.60</b>
ECMWF MR	0.78	0.28	0.17	0.22
<b>ECMWF HR</b>	0.70	0.63	0.69	<b>0.66</b>
EC-Earth LR	0.88	0.49	0.47	0.48
<b>EC-Earth HR</b>	0.53	0.63	0.77	<b>0.70</b>
HadGEM3 LR	0.93	0.52	0.66	0.59
HadGEM3 HR	0.64	0.63	0.51	0.57

Table 2 In column 1, are the acronyms of each model, as they are shortened in this text (details in the text). In column 2, are the correlation between the Niño3.4 index and the first canonical variable of SST  $\text{CV}^1_{\text{SST}}(t)$ . In columns 3-5 are their correlation values with respect to the results obtained from the SODAsi.3 reanalysis. In particular column 3 shows the spatial correlation calculated on the zonal component of the TWC, between 5N-20N and 165AE-240E, column 4 the correlation values for the concurrent SST anomalies underlying the TWC, and column 5 the mean between the two values.

At this stage, having established that all of the models, in the experiments we have considered, isolate the TWC/NPMM mechanism and having selected those that perform best, we want to proceed with the analysis of the internal variability of the TWC/NPMM-ENSO relationship. In the SODA reanalysis the TWC/NPMM-ENSO coupling was found to be non stationary across the 20th century (Pivotti and Anderson 2021). In particular, between 1920 and 1960 the relationship between ENSO and its precursor lost strength and, concurrently, the oscillatory behavior of ENSO changed.



During the periods of strong coupling the oscillation was found to behave like a stochastic response to climate noise, while in the intervening period when the coupling was absent, ENSO oscillated in a regular, self-sustained manner. These two behaviors could be detected in the power spectrum of the Niño3.4 index. In the former case, the power was spread over a range of different frequencies, while in the latter, all the power of the signal was concentrated within a narrow band of 6 year long periodicity (Pivotti and Anderson 2021).

In this study, we thus investigate whether the frequency of the reconstructed ENSO system shows any form of internal variability across the better performing ensemble members. In order to do so, we calculate the Continuous Wavelet Transform (CWT) of the yearly winter (NDJ) Niño 3.4 index for the better performing models, to study how ENSO periodicity varies over time. The CWT has been previously used by the authors (Pivotti and Anderson 2021) and it has shown to be able to detect changes in oscillatory behavior. Interestingly, we detect such different oscillatory behaviors within each of the 7 models' experiments listed in bold in Table 2. In particular, in all of these

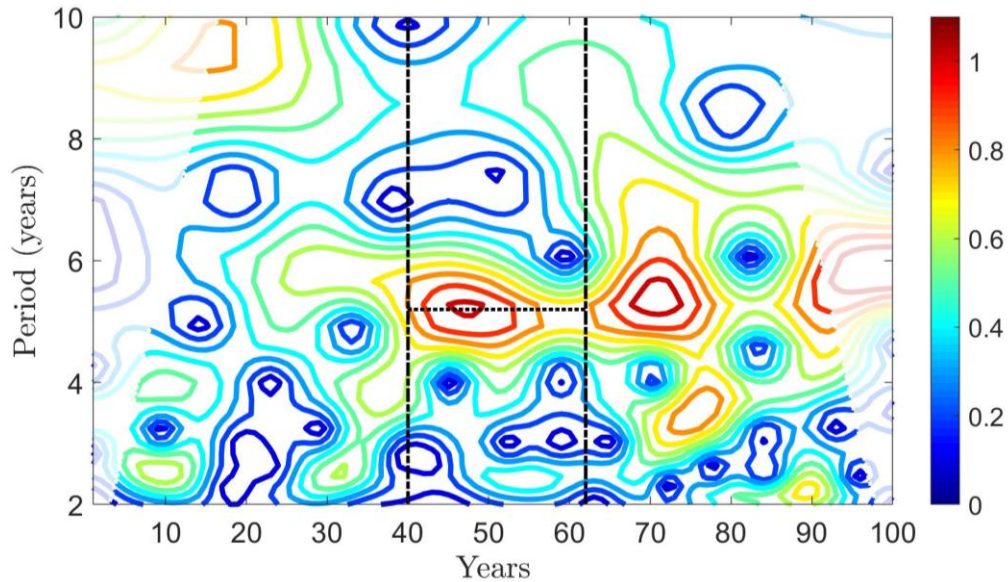
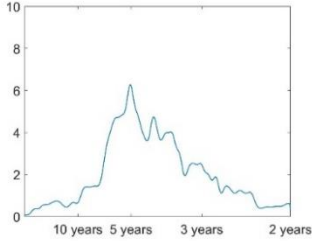
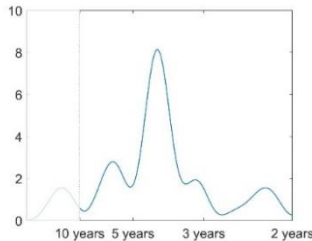
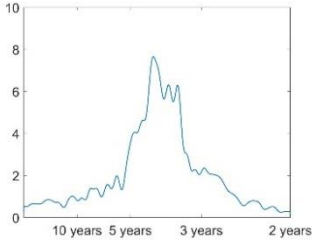
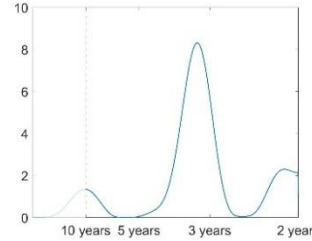
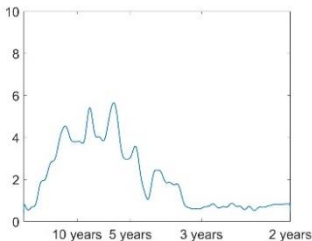
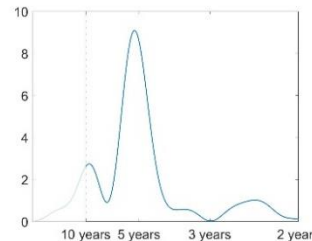


Figure 15 Continuous Morse wavelet transform (CWT) of the seasonal (NDJ) Niño3.4 index for the MPI LR experiment. On the x-axis is the year, on the y-axis is the period (in years). The white dashed lines set the boundary of the cone of influence, which is shaded in white. The black dashed vertical lines, at years 40 and 63, divide the full time period into the 3 sub-intervals. The black dashed horizontal line shows the single periodicity of the mid-interval at  $\sim 5$  years. Magnitude of spectral power ( $K^2$ ) at a given year/period is designated by the color bar on the r.h.s. of the figure.

experiments, we are able to identify sub-intervals during which the power of the signal is distributed over a diversified range of frequencies and sub-intervals during which the power is concentrated within a narrow frequency band. In order to illustrate this fundamental distinction, we show in Figure 15 the CWT of the experiment we abbreviated as MPI LR (acronyms illustrated in Table 1). Over the contours showing the power of the signal we draw two vertical black lines marking when this change in oscillatory behavior happens. Before year 40 and after year 63, we can see how the power of the signal is spread over different periodicities. For instance, around the year 11, the signal has power over 2 different periods, at 2.5 and 4 years; similarly, around the year 91 the power is both at 2 and 5 years. Between year 40 and year 63 however, the power of

the ENSO signal is concentrated solely on a period of around 5 years. This change in frequency means that the ENSO system is oscillating in two different ways. In particular, during the phase with a single frequency (in the case of MPI LR this happens during the intervening subinterval year 40-63) El Niño and La Niña events alternate in a regular way that gives rise to a constant cycle of 5 years of length. During the phases with multiple frequency instead, the system oscillates following cycles of different lengths. As previously mentioned, this specific variation is found in all 7 experiments listed in Figure 16. Two things are important to note: (1) in order to increase the robustness of our results, we take into account only sub-intervals of more than 10 years of length; (2) in those cases when the experiment's full interval is split in more than 2 sub-intervals, we concatenate those showing the same oscillatory behavior (either single or multiple frequency), thus always obtaining 2 sub-intervals from each experiment. The behaviour of these subintervals differ in many aspects such as: the ranges over which the frequencies change, the periodicity of the single-frequency phase, the lengths of such sub-intervals and the ways in which they alternate. We summarize these findings in Figure 16, where we show the Power Spectral Density (PSD) of the seasonal (NDJ) Niño3.4 index for each experiment. We separate the results obtained for multiple- and single-frequency subintervals in columns 2 and 3 of Figure 16 respectively. The resulting PSD is plotted to show how in the multiple-frequency case the power is distributed over a variety of periods, while in the case of a single frequency interval the peaks are clearer and more distinct. Importantly, these plots confirm the robustness of the method we used to identify and create the sub-intervals.

To determine whether this shift in oscillatory behavior within a given model results from a strengthening/weakening of the TWC/NPMM variability itself, for each experiment we carry out the following steps: (1) we split the time series of winter (NDJF) zonal wind stress into shifting sub-intervals of 30-years of length; (2) we reconstruct how the  $\tau_x$  maps shown in Figure 1 manifest themselves across the time-space matrix of  $\tau_x$  for each subinterval; and (3) we calculate the variance of the obtained time series. We find that this estimate of the variance of TWC/NPMM, independent from the coupling with ENSO, varies very little for each experiment, and when variations are found they do not align with the shifts in ENSO oscillatory behavior (not shown).

Name	Multiple	Single
CMCC LR	 1 - 81	 81-101
CMCC HR	 1 - 46 66 - 101	 46 - 66
MPI LR	 1 - 41 63 - 101	 41 - 63

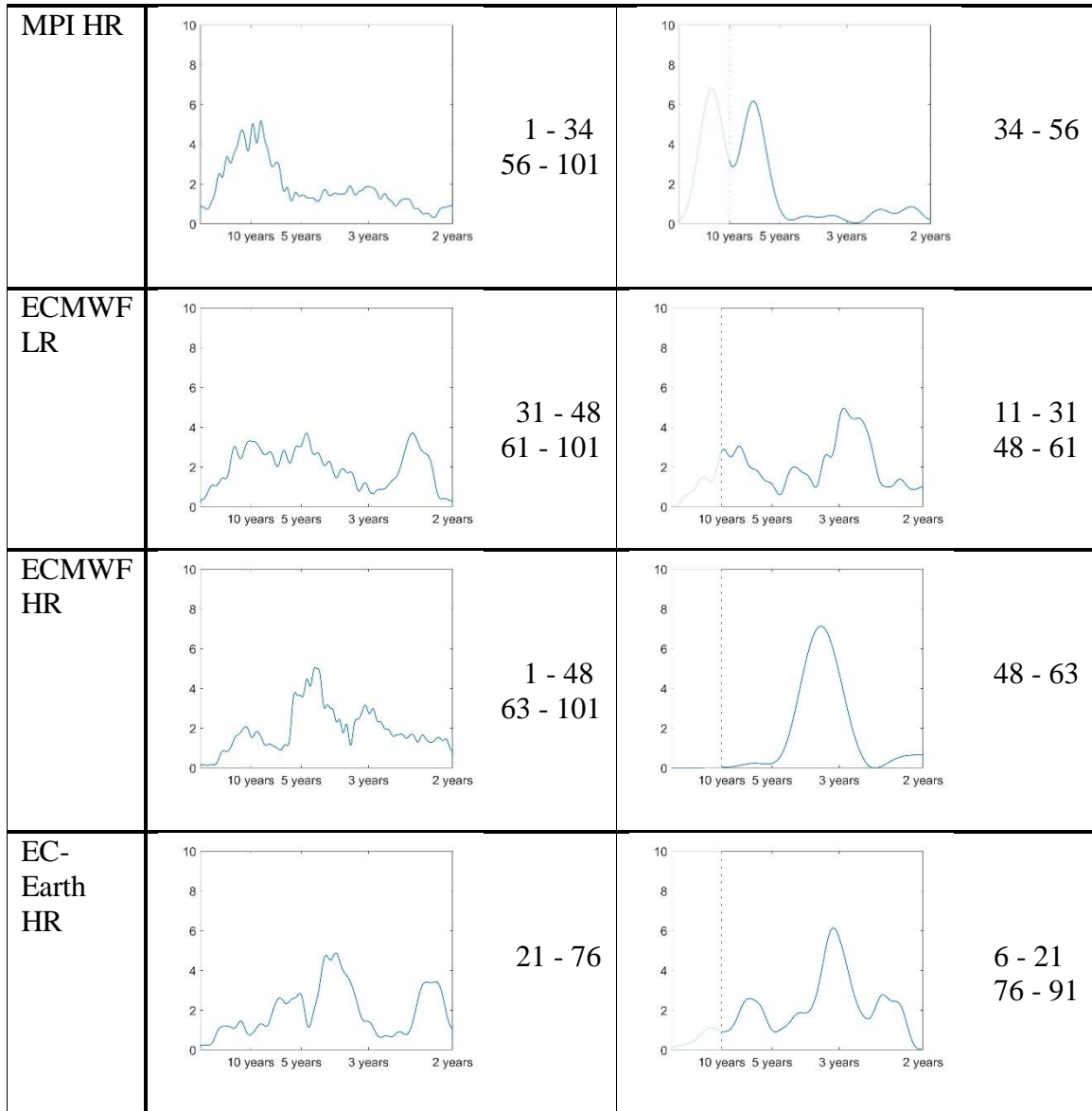


Figure 16 The results from the Continuous Wavelet Transform analysis, as shown in Figure 15, for the experiments of the better-performing models. In column 1 are the acronyms of each model, as they are shortened in this text (details in the text and in Table 1). In column 2 and 3 the power spectrum of the normalized Niño3.4 index calculated using Thomson's multitaper method over the sub-intervals during which the power of the ENSO signal is spread over multiple and single frequency, respectively. The details of how these intervals are selected and merged can be found in the text. The beginning and end years of the intervals are shown on the side of the plots. For each plot, the x-axis shows the frequency from low to high (logarithmic scale), with ticks indicating the corresponding period; the y-axis shows the amplitude ( $K^2/(\text{cycles}/\text{year})$ ). Note: due to the length of the single-frequency subintervals, results for periods longer than 10 years are not significant and therefore shaded in white in the corresponding plots.

Given that TWC/NPMM is consistently present across model simulations, we want to study whether the changes in ENSO oscillatory behavior corresponds to changes in the TWC/NPMM-ENSO coupling strength as it did in the historical reanalysis data. In order to do so, we apply the CCA in the basis of PC's to the two sets of sub-intervals within a given experiment. We now apply the CCA in the basis of PC's and follow the

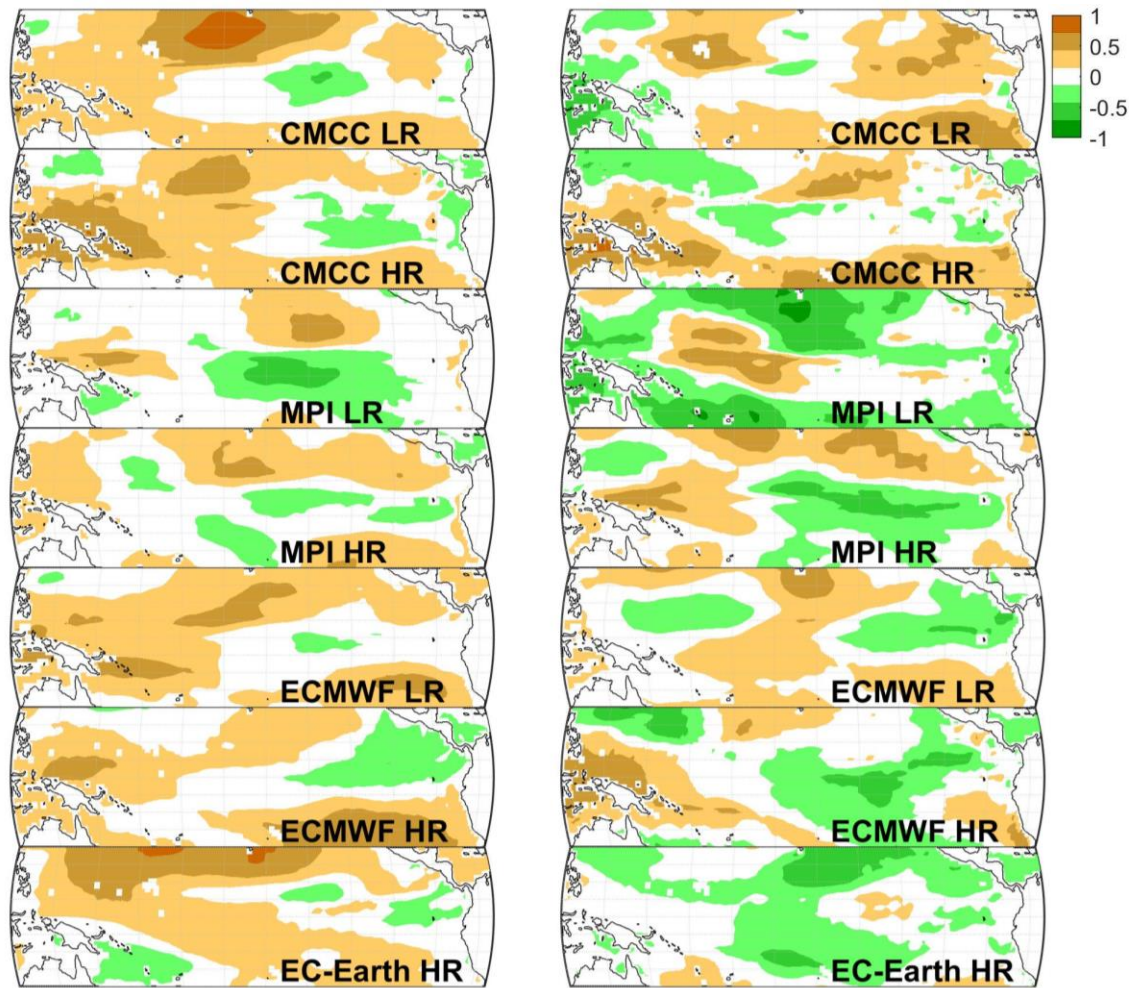


Figure 17 Maps of normalized zonal wind stress  $\tau_x$  anomalies regressed against  $CV^1 \tau_x(t-1)$  calculated for the 7 better performing models that are listed in Figure 16. On the left hand side are the results obtained for the multiple-frequency sub-intervals, on the right hand side for the single-frequency ones. Positive (negative) values are shaded in brown (green). Magnitude of normalized  $\tau_x$  (unitless) are given by the color bar.



same steps described for the analysis over the full intervals. In this way, we obtain, for each experiment, two pairs of highest correlated CV's. We then use these time series to reconstruct their corresponding anomaly maps via regression, as was done to create the maps in Figure 11 and Figure 12. In particular, we regress normalized and concurrent SST anomalies against  $CV^1_{SST}(t)$ ; and normalized and concurrent SST and horizontal wind stress anomalies against  $CV^1_{\tau_X}(t-1)$ . The resulting anomaly maps of  $\tau_X$  are shown for the multiple frequency sub-intervals on the left-hand side of Figure 17 and for the single frequency ones on the right-hand side of Figure 17. Although the maps show inter-model spread in the reconstruction of these modes, it is apparent that the multiple-frequency sub-intervals differ from the single-frequency ones. In particular, the ones having their power spread over multiple frequencies reconstruct a wind mode with positive anomalies in the northern extra tropics, while during the intervals with one single frequency the reconstructed modes vary widely.

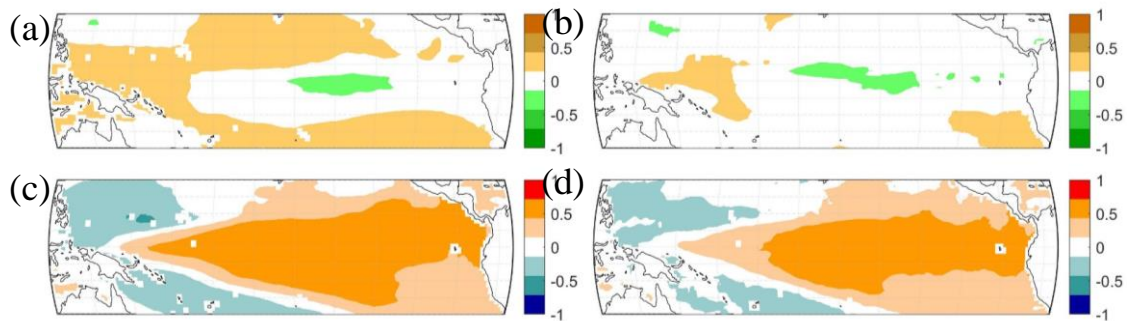


Figure 18 Results from the analysis over multiple-frequency and single-frequency sub-intervals.

(a) Mean of the maps shown on the left-hand side of Figure 17; (b) mean of the maps shown on the right-hand side of Figure 17.

(c) Mean of the maps of normalized SST regressed against the first Canonical Variable of SST calculated for the multiple frequency sub-intervals of the 7 better performing models that are indicated in Figure 16. (d) Same as (c) but calculated for the single frequency sub-intervals.

Finally, in order to get a comprehensive picture, we average these anomaly maps across the 7 better performing models of the ensemble and we keep the results from multiple and single-frequency sub-intervals separate, and show them in Figure 18. It is apparent that Figure 18(c,d) represent a positive ENSO event, thus guaranteeing that, even when restricting ourselves to the sub-intervals, the canonical variable  $CV^1_{SST}(t)$  isolates ENSO. More importantly, Figure 18a highlights that in the case of a multi-frequency oscillatory behavior, the TWC/NPMM is the most highly correlated zonal wind mode preceding ENSO. Further, during periods with highly oscillatory ENSO behavior, there is an absence of any wind-driven precursor pattern (Figure 18b), in agreement from the results obtained using SODA data (Pivotti and Anderson 2021).

### **Summary and Discussion**

In this chapter, we analyze how state-of-the-art models recreate the relationship between ENSO and preceding wind-stress variability. We carry out the analysis using the High Resolution MIP (HighResMIP) ensemble, within the CMIP6 framework. This ensemble is specifically tailored to investigate the effects that increased horizontal resolution may have on model performance, thereby running all experiments at both standard and increased resolution. Since we are interested in the internal variability of the system, for this analysis, we utilize the control runs of present-day climate, where the external forcings are kept constant at 1950's levels.

An initial analysis confirms that in all the models and at all resolutions there is a strong coupling between mature ENSO events and zonal anomalies in the Pacific trade winds, north of the Equator. This wind anomaly is the signature of the mode that, on the



one hand, initiates the Trade-Wind Charging (TWC) of the equatorial subsurface with warm water and, on the other hand, gives rise to the SST anomalies characteristic of the North Pacific Meridional Mode (NPMM). Therefore, we refer to this precursor mechanism as the TWC/NPMM forcing mode. We analyze the ensemble performance by comparing how the models reconstruct fields of ENSO and TWC/NPMM against the corresponding results obtained from SODAsi.3 reanalysis data. We see significant pattern correlations across the ensemble for all fields of interest, which let us conclude that, despite some intra-model variability, the TWC/NPMM mechanism is a well-established ENSO precursor in this state-of-the-art model ensemble. Moreover, all the tests we run to estimate the simulations of these two modes suggest that increasing the horizontal resolution, in this case, does not have a consistent impact on model performance. That said, the HighResMIP ensemble might be too small to consistently discern whether such improvements occur, especially considering the various changes in resolution, as shown in Table 1.

After having assessed the presence of this driving mechanism, we decided to gather a more complete picture of the TWC/NPMM-ENSO coupling by looking at how the experiments recreate the internal variability of the modes on their own, as well as their mutual relationship. In order to do this, we first isolate a subset of experiments by selecting those that best reconstruct the TWC/NPMM fields and focus on them. Our first finding is that in all of these better-performing experiments there are periods during which the ENSO signal oscillates regularly, with constant periodicity and periods during which the oscillation of the signal is noisier, over a diverse range of frequencies. This

finding agrees with similar results obtained from a previous study on SODAsi.3 reanalysis data (Pivotti and Anderson 2021); and with earlier findings on observationally-based datasets (Yiou, et al., 2000; Wang and Wang 1996). Furthermore, once we analyze these different oscillatory phases separately, we uncover that the spectral changes in ENSO are mirrored by variations in the TWC/NPMM-ENSO relationship. In particular, the CCA in the basis of PC's reveals that the TWC/NPMM precursor is strongly coupled with ENSO during the years of stochastic oscillatory behavior, but, despite being present, it does not consistently precede ENSO when the oscillation has a constant periodicity. We argue that this is a consequence solely of the coupling between the modes because the variability of the TWC/NPMM mechanism itself is small in all of the experiments and its variations do not align with the shifts in ENSO periodicity. This last result is also in agreement with previous findings on observationally-based SODAsi.3 (Pivotti and Anderson 2021). As the length of the experiments is of about 100 years and the changes in oscillatory behavior are decades-long, we advise for further studies to investigate this relationship and its internal variability on longer simulations.

As argued by Wang, et al., (2017), the framework to interpret ENSO is dual. The mode can be seen either as a self-sustained oscillation, or as a response to climate noise. Our results suggest that, within the HighResMIP ensemble, once an experiment is able to well simulate the TWC/NPMM mode, it reconstructs ENSO as a signal that shifts between these two underlying dynamics. In particular, during the multiple-frequency phase, when the TWC/NPMM- ENSO coupling is active, we argue that the system is responding to stochastic atmospheric forcing. During the phases when the power is

within a single-frequency band, instead, and no atmospheric mode seems to precede ENSO, we argue that the system behaves as an un-triggered, self-sustained oscillation.

During these phases, ENSO could be described by either of the four conceptual mechanisms comprising the unified oscillator: the delayed oscillator, the western Pacific oscillator, the recharge–discharge oscillator, and the advective–reflective oscillator (Wang 2001). These frameworks have different mechanisms that operate over different amounts of time. Across the 7 models here considered, the power of ENSO’s oscillatory signal is concentrated over different single-frequency bands: we recorded periods of 3, 4, 5 and 6 years of length. We argue that this is a consequence of the fact that the underlying mechanism responsible for these self-sustained phases may differ across models. Hence current and future ENSO characteristics may evolve differently across models over the coming decades depending upon how the underlying mechanism itself evolves within each.

## CHAPTER FOUR

### Introduction

As noted in Chapter 3, the better we understand and characterize ENSO and its occurrence, the easier it becomes for affected communities to prepare in the face of ENSO-related climatic impacts. To contribute to this endeavor, in this study, we focus on a specific set of driving mechanisms, namely NPO-induced Trade Wind Charging (TWC) (Anderson and Perez 2015) and NPO-induced North Pacific Meridional Mode (NPMM) (Amaya 2019), henceforth referred to as TWC/NPMM variations. In previous chapters, the TWC/NPMM-ENSO relationship has been studied in historical data and control model simulations. In this chapter, we study how this relationship behaves in the presence of anthropogenic forcings.

Numerical models have been a fundamental tool to understand how climate modes and their reciprocal relations behave now and will in the future. A recent paper by Yeh, et al. (2018) provides a comprehensive overview of recent findings on ENSO projected changes, from the simulations from the third and fifth Coupled Model Intercomparison Projects - CMIP3 and CMIP5 respectively. The main conclusion is that the impacts of global warming on ENSO are not well constrained, but ever-evolving, and model simulations do not agree on how the teleconnections will change in scale and intensity. The review by Yeh, Kug, et al. (2009), focused on the projections of Eastern vs. Central Pacific ENSO, argues that, according to CMIP3 models, the latter is going to be the dominant flavor of ENSO. Other studies have focused on other characteristics of future ENSO events, such as its amplitude (Wang, et al. 2017), its variability (Collins, et

al. 2010), the occurrence of extreme events (Cai, et al. 2015) and how the characteristics of these different events affect weather patterns differently (Wang, et al. 2017). One important aspect that has not been investigated at length is the frequency of the ENSO signal, both in the range of its periodicities, as well as in the shifts in the type of oscillation. In Timmerman, et al. (1999) the ENSO frequency was predicted to increase because of global warming. However, using historical data, Pivotti and Anderson (2021) showed that even in the absence of anthropogenic forcing the behavior of ENSO can show internal multi-decadal shifts between stochastic and oscillatory phases and that these shifts mirror changes in the strength of the TWC/NPMM-ENSO relationship.

Our objective here, then, is to examine future changes in the characteristics of ENSO in relation to the TWC/NPMM-ENSO coupling under the influence of increased human-induced climate forcings. This is carried out using a state-of-the-art model ensemble called High Resolution Model Intercomparison Project (HighResMIP) which is part of the CMIP6 protocol. In particular, first we describe in details the HighResMIP model ensemble and the experiments we employ, as well as the different methodologies that we utilize in the study. Then, we present the obtained results that we then summarize and discuss in the conclusive section.

## **Data and Method**

### *Data*

The model ensemble for this analysis is the one developed for the High Resolution Model Intercomparison Project (HighResMIP), which is endorsed by CMIP6 and thoroughly described in (Haarsma, et al. 2016). We utilize three experiments for each

model, namely: (1) control-1950, a 100 years long simulation with constant 1950's radiative forcing levels which correspond to a global radiative forcing of  $\sim 0.5 \text{ W/m}^2$  (Myhre, et al. 2013); (2) hist-1950, an experiment with prescribed radiative forcings from 1950 to 2014; and (3) highres-future, a simulation that continues from where hist-1950 ends until 2050, with external forcings prescribed to follow the RCP8.5 scenario from the fifth IPCC. In this pathway no mitigation efforts are implemented (Pachauri and Alle 2014) and radiative forcing reaches  $8.5 \text{ W/m}^2$  by 2100 (Riahi, et al. 2011). For brevity, we will refer to experiment (1) as the control and to the 101 years of combined hist-1950 and highres-future as the transient run henceforth. According to the HighResMIP protocol, each institution runs all experiments at a standard and an enhanced horizontal resolution. The details of the models included, the institutions responsible and their specific resolutions are presented in Table 1.

The variables of interest for this analysis are sea surface temperature SST and zonal wind stress  $\tau_x$ . The first variable is used to capture the variability of ENSO, the latter for TWC/NPMM. We limit our focus to the Tropical Pacific, between latitudes 20S and 20N and longitudes 120E and 70W, where both ENSO and TWC/NPMM are active, following the lead of (Anderson and Perez 2015) and (Larson and Kirtman 2013). Temporally, we calculate anomalous winter means over the months during which ENSO and TWC/NPMM are most active: November-January for ENSO (SST) (Trenberth 1997) and November-February for TWC/NPMM ( $\tau_x$ ) (Anderson and Perez 2015) respectively. Lastly, it is important to note that since we are interested in the  $\tau_x$  mode that precedes ENSO events, the two variables are lagged accordingly by one year.

Institution	Model ID	Ocean Res (km)	Atmosphere Res (km)	Name
CMCC	CMCC-CM2-HR4	25	100	CMCC LR
	CMCC-CM2-VHR4	25	25	CMCC HR
CERFACS	CNRM-CM6-1	100	100	CNRM LR
	CNRM-CM6-1-HR	25	50	CNRM HR
MPI	MPI-ESM1.2-HR	40	100	MPI LR
	MPI-ESM1.2-XR	40	50	MPI HR
EC-Earth	EC-Earth3P	100	80	EC-Earth LR
	EC-Earth3P-HR	25	40	EC-Earth HR
MOHC	HadGEM3-GC31-LL	100	250	HadGEM3 LR
	HadGEM3-GC31-HM	25	50	HadGEM3 HR

Table 3 Details of the HighResMIP ensemble utilized in this study

### *Method*

Across the study we have utilized three main analytical diagnostics. The first is a variation of the classic Canonical Correlation Analysis (CCA) called the CCA in the basis of Principal Components (PC's) (Bretherton, Smith and Wallace 1992). In particular, as in the classic version of the CCA, this method is used to isolate the most highly correlated modes between two variables, in this case the winter means of SST and the winter mean  $\tau_x$  during the prior year. In this version, the CCA is applied not to the full fields, but only to a subset of their respective PC's, obtained through an Empirical Orthogonal Functions (EOF) analysis. Furthermore, we exclude from the CCA the PC of  $\tau_x$  that has the highest correlation with the concurrent Niño3.4 index, as we want to remove the influence from concurrent ENSO events on the zonal wind stress. We use the CCA in the basis of PC's to understand whether and how each ensemble model reconstructs the relationship between ENSO and its extra-tropical precursor

TWC/NPMM. This method is described in further details in previous articles by the authors where we analyzed the relationship between ENSO and the TWC/NPMM precursor in the SODAsi.3 reanalysis dataset (Pivotti and Anderson 2021) and in the control runs of the HighResMIP ensemble (Pivotti et al.1 – in review).

Secondly, we calculate the Center of Heat Index (CHI) of ENSO (Giese and Ray 2011) to better understand its characteristics. The CHI has different components and in this analysis we calculate the amplitude and the longitude, as well the area of each ENSO event. In each of these calculations we include all the years that satisfy the CHI requirement, namely the years in which the area over which the SST anomalies are greater than 0.5 (<-0.5 respectively) is larger than the Niño 3.4 area (5S-5N 170-120W) – details in (Giese and Ray 2011).

Finally, to investigate whether the power and oscillatory behavior of the ENSO signal show trends across the ensemble, we turn to the Continuous Wavelet Transform (CWT) and apply it to the first PC of Tropical SST anomalies (Pivotti and Anderson 2021). To study the resulting time/periodicity maps  $W(p,t)$ , we calculate three indicators that mirror what the CHI components capture for the SST spatial anomaly maps. As a first step, to guarantee significance, we consider only the values that lie within the cone of influence. Then, to reduce noise, we exclude the values whose periodicity is higher than 10 years and whose power is less than  $\text{std}(W(p,t))$ . The first indicator,  $P(t)$ , captures the power of the signal over time. We sum the power across periodicities for each time-point analogous to the calculation of the CHI-amplitude.

$$P(t) = \sum_p W(p,t)$$



As a second indicator,  $C(t)$ , we estimate the “central periodicity” at each time point, similar to the CHI-longitude, and thus calculate the weighted mean of the periodicity.

$$C(t) = \sum_p p \cdot W^*(p,t), \text{ where } W^*(p,t) = W(p,t) / \sum_p W(p,t)$$

Finally, as a third indicator  $S(t)$ , we estimate the spread around this estimated center of periodicity.

$$S^2(t) = [\sum_p (p - C(t))^2 \cdot W^*(p,t)] / \sum_p W^*(p,t) = \sum_p (p - C(t))^2 \cdot W^*(p,t),$$

$$\text{and } S(t) = \sqrt{S^2(t)}$$

## Results

We apply the CCA in the basis of PC's to the winter means of  $\tau_X$  and SST, and obtain pairs of time series called Canonical Variables (CV). These time series are in decreasing order of correlation value, which means that the first pair captures the modes showing the highest correlation. In this case, the pair of CV's has a 1-year lag by construction and represent a mode of  $\tau_X$  ( $CV^1_{\tau_X(t-1)}$ ) and a mode of SST ( $CV^1_{SST(t)}$ ) respectively. In order to illustrate the spatial characteristics of these highly correlated modes, we regress  $CV^1_{\tau_X(t-1)}$  and  $CV^1_{SST(t)}$  against the normalized anomaly fields of

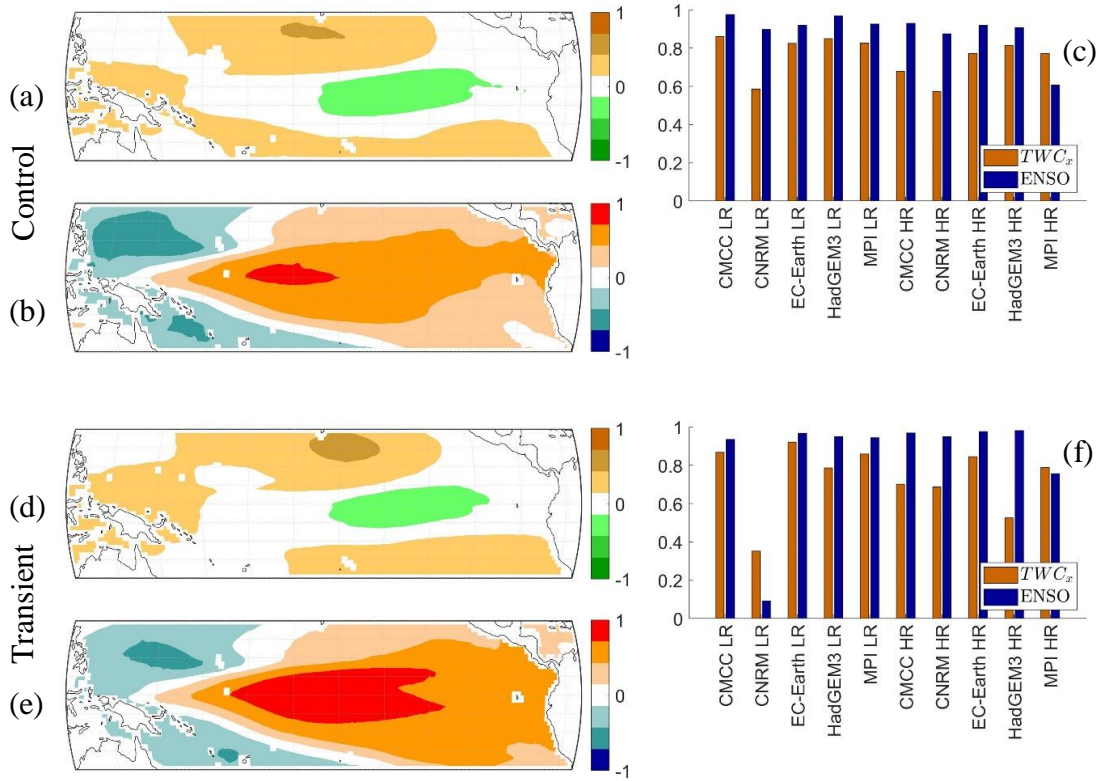


Figure 19 Ensemble mean maps of normalized anomalies of  $\tau_X$  and SST regressed against their respective first Canonical Variable for control (a,b) and transient runs (d,e). (a,d) maps of  $\tau_X$ . Positive (negative) values are shaded in brown (green). Magnitude of normalized  $\tau_X$  (unitless) are given by the color bar on the r.h.s of the panel. (b,e) maps of SST. Positive (negative) values are shaded in red (blue). Magnitude of normalized SST (unitless) are given by the color bar on the r.h.s of the panel. In panels (c,f) the values of spatial correlation between the regression maps from each model and the ensemble mean maps. In brown the values for  $TWC_X$  in blue those for ENSO.

their respective variables and obtain for each experiment two anomaly maps. We do not show here the regressed maps for each experiment, instead we illustrate how the ensemble behaves as a whole, by calculating the ensemble-wide average maps of  $\tau_X$  and SST for control and transient experiments separately. The resulting maps, which we call TX and S are shown in Figure 19, panels (a,b) for the control experiments (TXC,SC) and panels (d,e) for the transient (TXT,ST) respectively. The first interesting result is that

both TXC and TXT capture a positive anomaly in the zonal component of the northern Tropical Pacific trades, while SC and ST reconstruct a positive SST anomaly in the eastern portion of the Equatorial Pacific. This confirms that across the ensemble the most highly correlated modes of lagged  $\tau_x$  and SST are the TWC/NPMM precursor and ENSO in both control and transient experiments, as it is in the historical data (Pivotti and Anderson 2021). Moreover, their spatial characteristics are largely unaltered by the increase in anthropogenic forcings, as indicated by the high spatial correlations between patterns:  $\rho(\text{TXC}, \text{TXT}) = 0.93$  and  $\rho(\text{SC}, \text{ST}) = 0.97$ , respectively. Furthermore, in order to better capture the ensemble behavior, for each set of experiments, we calculate the spatial correlation between the map of each individual model against the corresponding ensemble mean map. The results are presented on the right-hand side of Figure 19, in panels (c,f). These results indicate that the correlation values for the SC and ST maps are higher across the ensemble for both control and transient runs, as compared to the correlation values for the TXC, TXT maps. This suggests a greater inter-model agreement in the reconstruction of ENSO patterns, when compared to TWC/NPMM patterns. Furthermore, models with a standard resolution (LR) and those with an increased resolution (HR) show no significant difference in their correlation values, which leads us to conclude that the difference in horizontal resolution does not affect a model's ability to reconstruct the spatial characteristics of the TWC/NPMM-ENSO relationship, either in the control, or in the transient runs.

Having established that TWC/NPMM is a consistent ENSO precursor in this ensemble, we want to characterize its influence upon ENSO events. We do this by

calculating three components of CHI of ENSO: amplitude, longitude and area (Giese and Ray 2011). We then compare average ENSO events against the ones initiated by TWC/NPMM. We define average ENSO events as those years during which the winter means of SST satisfy the CHI requirement (details in the Data and Method section). These events will be referred to as CHI-ENSO events. Among the CHI-ENSO events, we select those that are preceded by a TWC/NPMM event. We identify these years T as those for which either

$$CV\tau_X(T - 1) > \text{std}(CV\tau_X) \text{ or } CV\tau_X(T - 1) < - \text{std}(CV\tau_X)$$

holds true, and these events will be referred to as TWC/NPMM-related CHI-ENSO.

The results of these calculations are shown in Figure 20, which all have 4 panels. In Figure 20(a,b) we plot, for each experiment, the mean CHI amplitude of all CHI-ENSO events on the x-axis against the mean CHI amplitude of the TWC/NPMM-related CHI-ENSO events on the y-axis. Panel (a) shows the results for the control experiments and panel (b) shows them for the transient ones. In Figure 20 (c,d) instead we still look at the CHI-amplitude, but the means are calculated across type of experiment, with result for the control on the x-axis, and for the transient on the y-axis. In panel (c), we show the results for CHI-ENSO events and in panel (d) we show them for TWC/NPMM-related events. Figure 21 has the same structure as Figure 20, but shows the results for the CHI longitude, while Figure 22 shows an estimate of the CHI-area. Starting with the CHI-amplitude in Figure 20(a,b), we find that all the points are found above the 1-1 line (significant for 9 /10) which indicates an ensemble-wide agreement that ENSO events

initiated by TWC/NPMM are stronger than the average ENSO events, and that this difference holds true both in the control and the transient experiments. Further comparison of CHI amplitude for the controls against those of the transient experiments indicates that there is no trend in the CHI amplitude for either average CHI-ENSO events or TWC-charged ones, indicating that the influence of TWC/NPMM on ENSO amplitude is not enhanced (nor reduced) as a result of anthropogenic forcings.

With regard to the longitude of ENSO events, Figure 21a shows that the TWC/NPMM-related CHI-ENSO events have their center of heat situated more

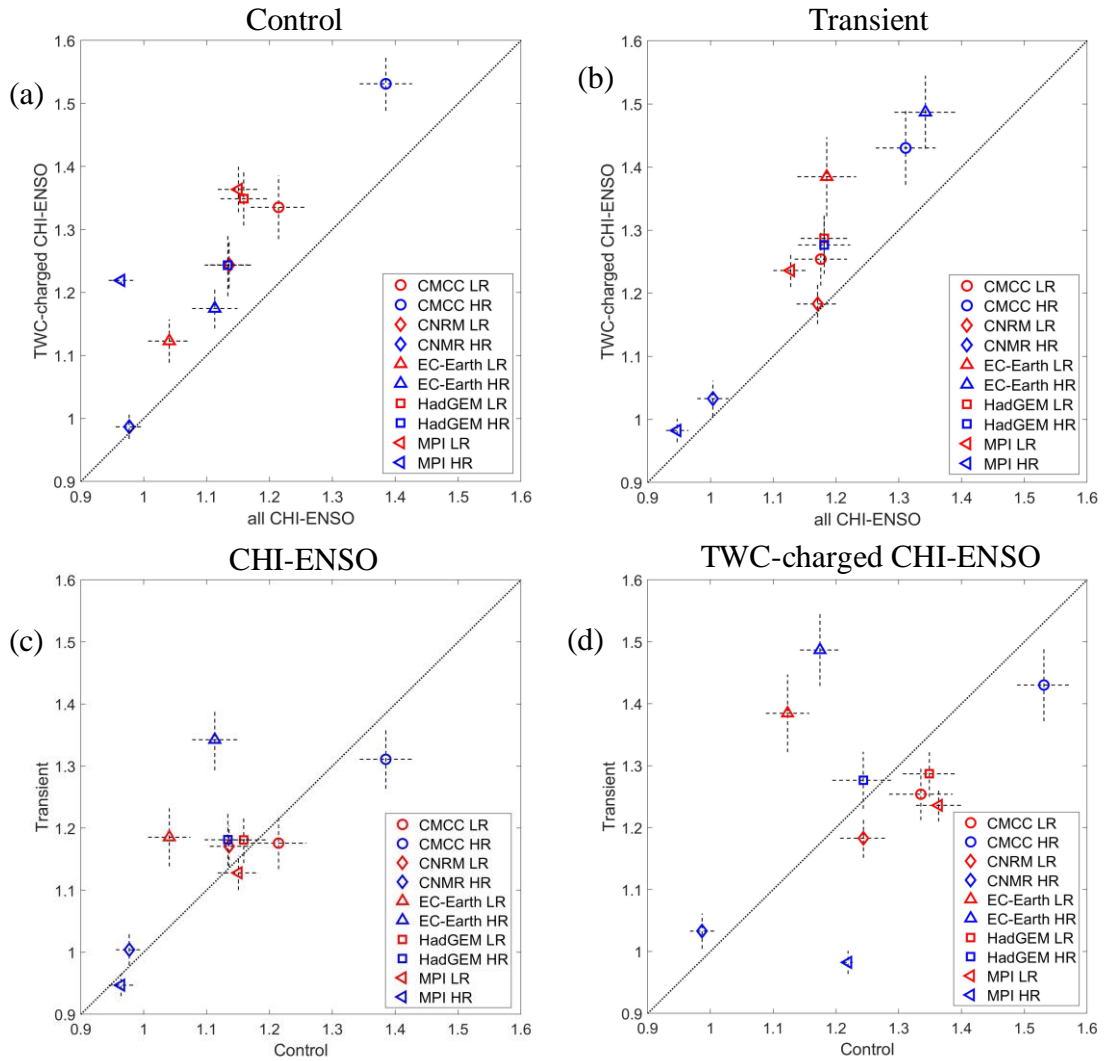


Figure 20 Amplitude of the Center of Heat Index (CHI).

For each model, we calculate the CHI-amplitude of all winter (NDJ) events that satisfy the CHI-criterion (CHI-ENSO) as well as for the CHI-ENSO events that have a strong TWC event the preceding winter (TWC-charged CHI-ENSO). Markers show the average CHI values, and the standard error of the mean is shown by the black dashed lines. Red markers represent LR models and blue represent HR models. The  $y = x$  line is shown in dotted black.

In (a) and (b) the mean CHI-amplitude of the average ENSO events (x-axis) plotted against the mean CHI-amplitude of the TWC-charged CHI-ENSO events (y-axis), for the control runs (a) and the transient runs (b).

In (c) and (d) the mean CHI-amplitude of the ENSO events of the control experiments (x-axis) plotted against the mean CHI-amplitude of the ENSO events of the transient experiments (y-axis), for all CHI-ENSO events (c) and TWC-charged CHI-ENSO events (d).

westward than CHI-ENSO events in the control runs (significant for 8/10 models).

However, this result does not hold true in the case of the transient runs in Figure 21b.

Plotting the control values against transient ones in Figure 21(c,d), we find that the center of heat of CHI-ENSO events moves westwards in the presence of anthropogenic forcings, but remains unaltered for TWC/NPMM-related events. Combining these results suggests

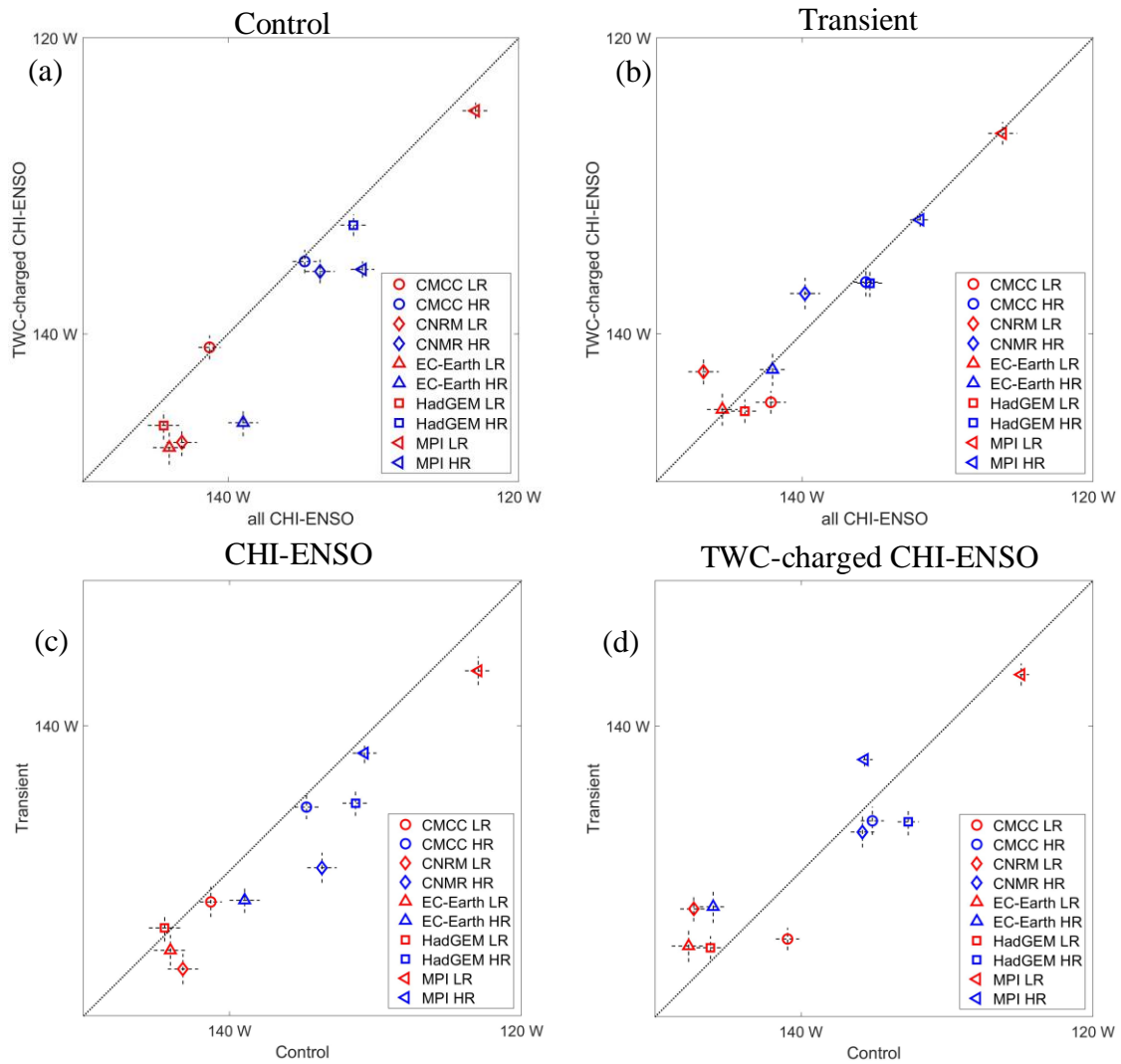


Figure 21 Same as Figure 20, except showing the CHI longitude instead of the amplitude.

that average ENSO events will align westward where the TWC/NPMM-related events already have their center of heat.

Finally, from Figure 22(a,b) we see that the SST anomalies of the TWC/NPMM-related events cover a larger area both in the control runs (significant for 6/10 models) as well as in the transient runs (significant for 9/10 models). Furthermore, CHI-ENSO

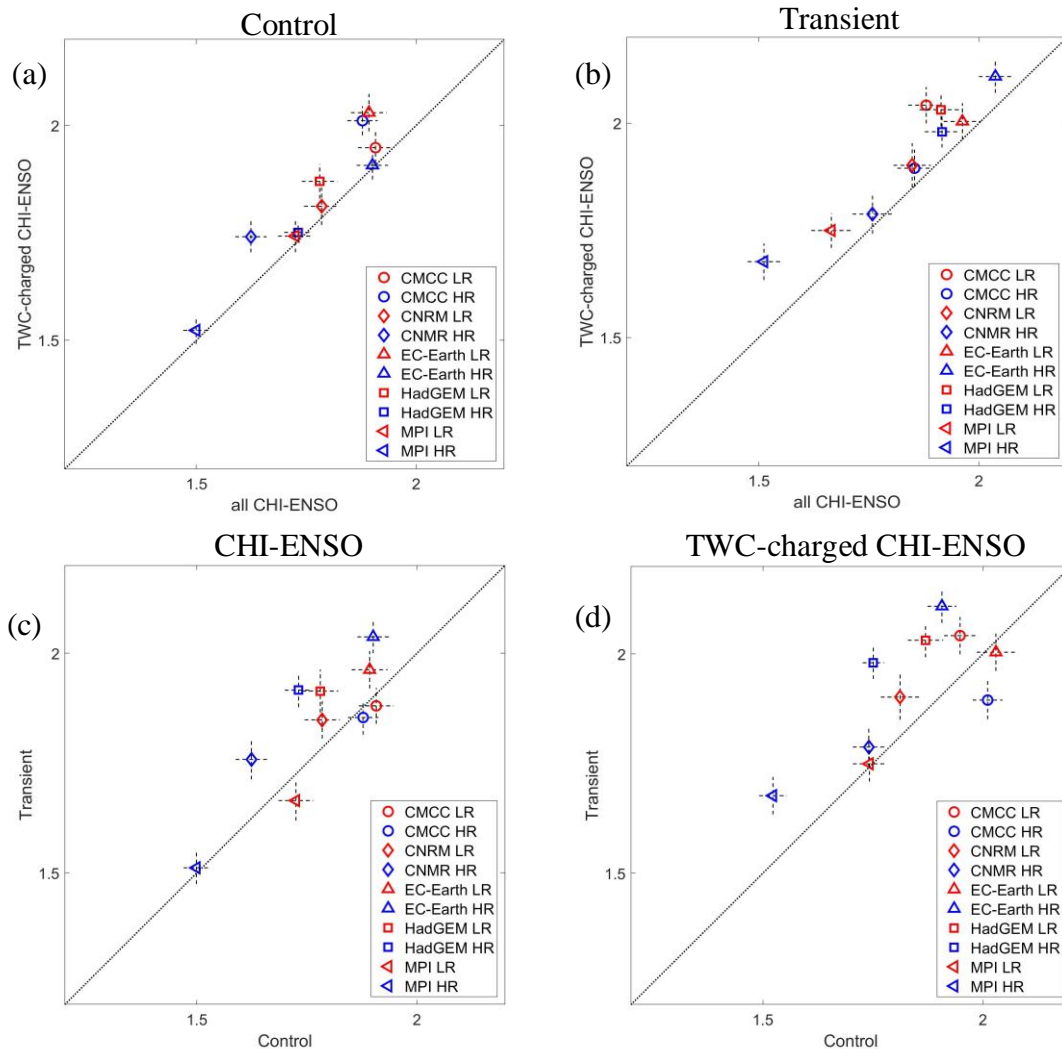


Figure 22 Same as Figure 20 and 21, except showing an estimate of the CHI area. Since the models have different resolutions, we show here the ratio between the extension of the SST anomalies and the extension of the Niño3.4 area. It is important to remember that, because of the CHI requirement, all areas included in the calculation are larger than the Niño3.4 area, which means that all values are greater than 1 by default.



events cover larger areas in the transient experiments compared to the controls, whether they are initiated by TWC/NPMM (Figure 22d) (significant for 7/10 models) or not (Figure 22c) (significant for 6/10 models).

The results of Figure 21 and Figure 22 made us consider whether there was a relationship between the CHI-area and CHI-longitude values. Thus, we plot them for all CHI-ENSO events in Figure 23. We find a significant negative correlation between them suggesting that the westward shift of the center of heat results from the fact that a larger portion of the equatorial Pacific SST is affected by ENSO variability, which consequently moves the center of heat. As such, this apparent shift westward does not result from a shift towards CP-type ENSO events.

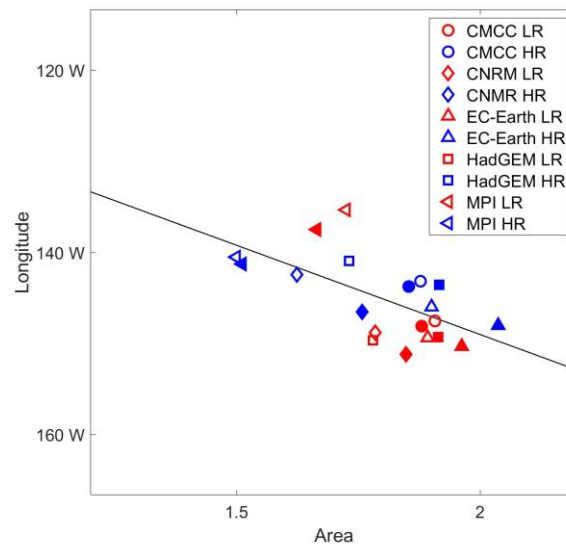


Figure 23 CHI area (x-axis) plotted against the corresponding values of the CHI longitude (y-axis). Markers show the average CHI values. Red markers represent LR models and blue represent HR models; empty markers represent the control runs and filled markers represent the transient ones. In black the fitted regressed line whose coefficients are significant at  $\alpha=0.95$ .

To summarize the results above, the amplitude of TWC/NPMM-related events remains consistently larger whether under the influence of increasing external forcings or in the control experiments. In addition, the TWC/NPMM-related events have larger area and hence are shifted more westward than standard events in the control run, however this difference disappears as the standard events grow larger and hence shift more westward under the influence of increasing external forcings.

So far, we have analyzed the influence of the TWC/NPMM-ENSO relationship on the spatial characteristics of ENSO. To complete the characterization of the TWC/NPMM-ENSO relationship, we investigate the relative amount of TWC-charged events. In particular, we calculate the ratio between the number of TWC-charged CHI-ENSO events and the total amount of CHI-ENSO events for control and transient experiments separately. We show the results in Figure 24 where we plot the value for the

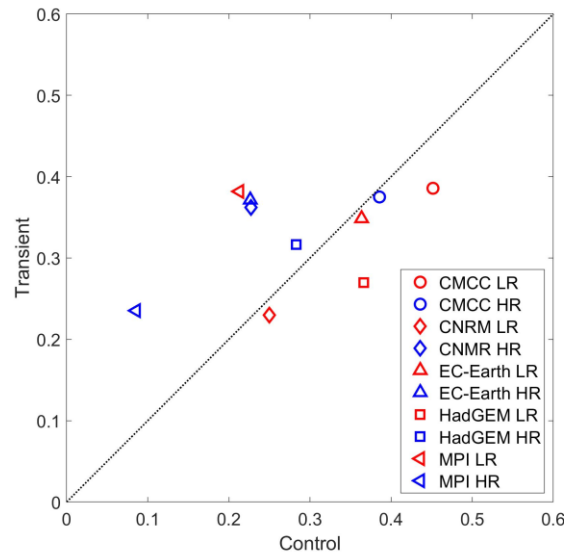


Figure 24 Markers show the ratio between the number of TWC-charged CHI-ENSO events and CHI-ENSO events. On the x-axis the value for the control runs, on the y-axis for the transient ones. Red markers represent LR models and blue represent HR models. The  $y = x$  line is shown in dotted black.

control simulation on the x-axis, against the value for the transient one on the y-axis. There, we see a lack of inter-model agreement as the models are evenly split on whether the frequency of TWC-charged events are increasing or decreasing in the presence of increasing forcings. In both sets of runs, the TWC-charged events represent approximately 30% of the total CHI-ENSO events (mean of the relative amount of TWC-charged events calculated over all of the experiments), but can be as many as 40% in some simulations and as little as 10% in others (as shown in Figure 24).

In the second portion of our analysis, we now turn to the oscillatory behavior of ENSO, as previous results indicate that the strength of the TWC/NPMM-ENSO coupling can influence the stochasticity of ENSO variability in both historical data (Pivotti and Anderson 2021) and model simulations (Pivotti et al.1 – in review). To capture potential future changes in the oscillatory behavior of ENSO variability, we look at how the power of the ENSO signal is spread across frequencies by calculating the Continuous Wavelet Transform (CWT) of the leading principal component of Tropical SST anomalies ( $PC_1$ ). We use  $PC_1$  to isolate ENSO, because it is more representative of a model's specific equatorial variability than a geographically fixed index like Niño3.4 would be, as

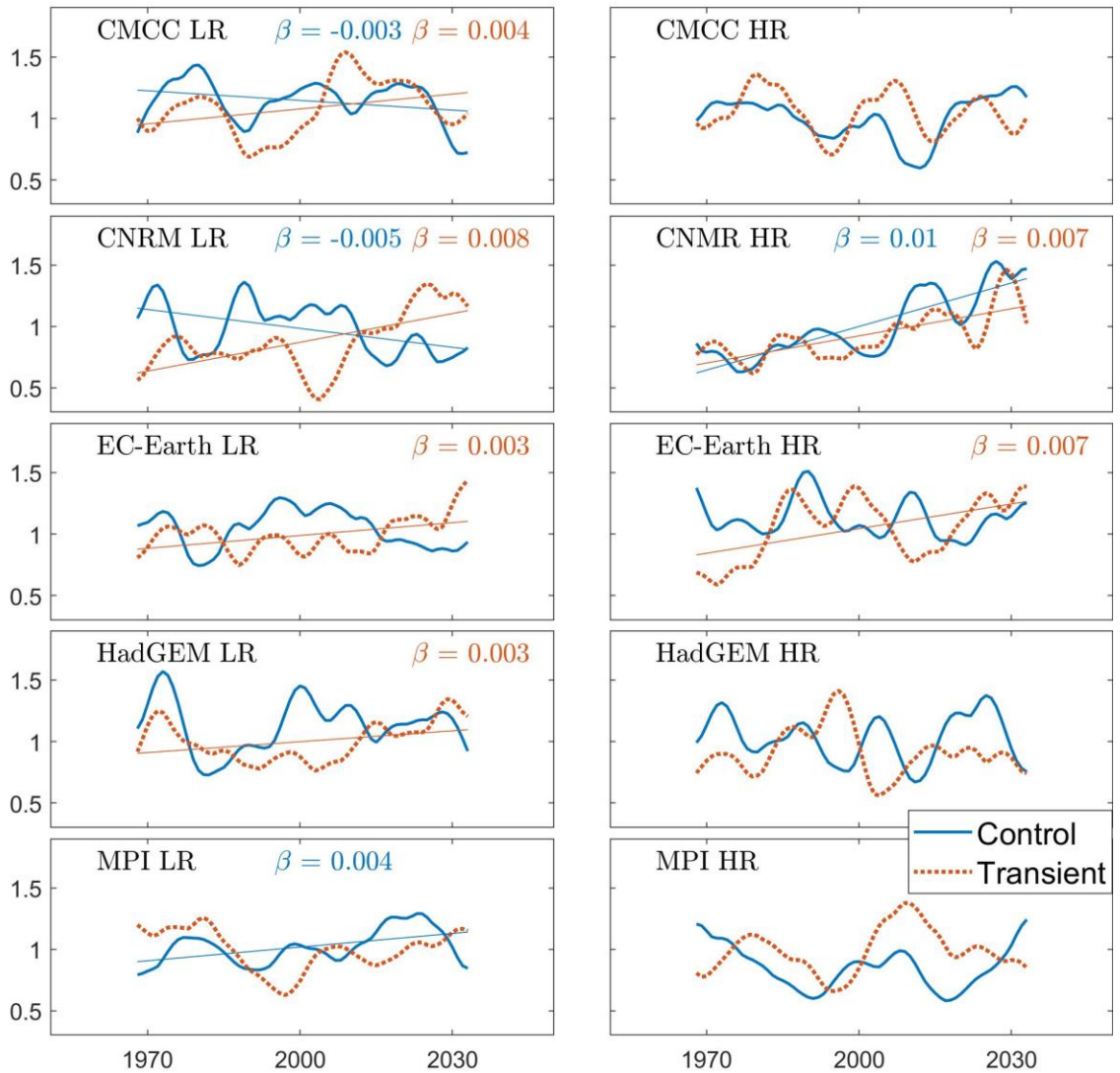


Figure 25 Time-series of the power  $P(t)$  of the Continuous Wavelet Transform (CWT) – see text for details. Results from the control runs are in blue and those for the transient in dashed red. The thin lines represent trends, when significant at  $\alpha=0.90$ , of the slope, whose value is written at the top of each panel.

evidenced by the intra-model spatial variability in ENSO reconstructions shown in Figure 19. Furthermore, the  $PC_1$  time series is more consistent with the previous portion of our analysis, where we utilize principal components in the CCA.

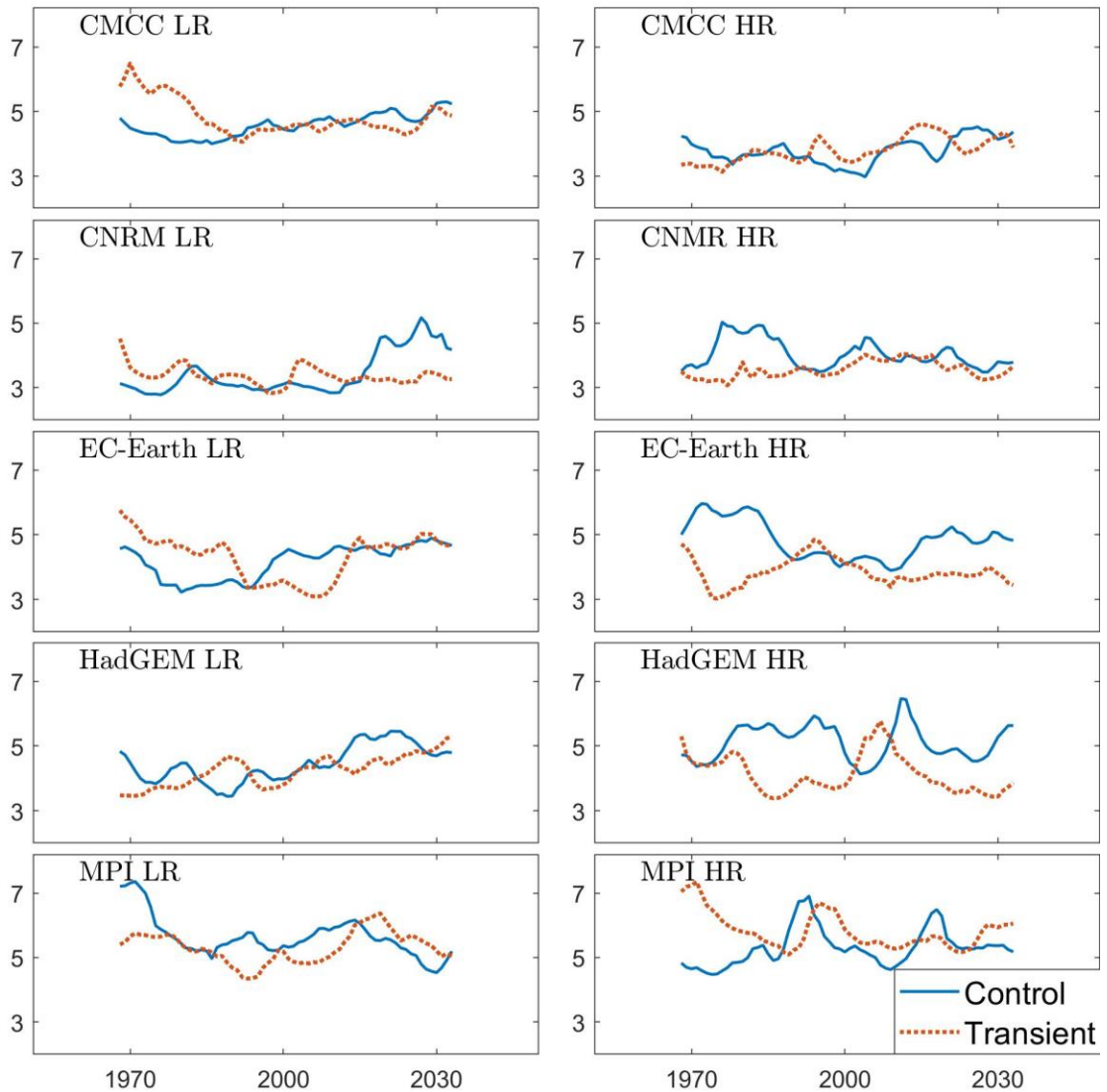


Figure 26 Same as Figure 25 except for the center of periodicity  $C(t)$  of the Continuous Wavelet Transform (CWT) – see text for details.

To study the time-frequency CWT matrices obtained for both control (CWTC) and transient (CWTT) experiment, we calculate the power of the signal  $P(t)$ , the center of periodicity  $C(t)$ , and the spread around  $C(t)$ ,  $S(t)$  (details in the Method subsection). First, we show  $P(t)$  in Figure 25, along with any slope that is significant at  $\alpha=0.90$ . Looking at the slopes, 6 out of 10 models indicate a future increase in the mean power of ENSO, and

only one among them shows a trend of the same sign in the control run, suggesting that for at least 5 models such an increase is not a result of the model's internal variability as opposed to increasing forcings. We compare the trends of this estimate of the power with another one, namely the standard deviation of the Niño3.4 index, in Table 4, and we see that, when the values are significant, the two estimates agree on the sign of the trend.

Name	Experiment	std(Niño3.4)	$\overline{CWT}$
CMCC	C	-	-
	LR	+	+
CMCC	C	+	
	HR	-	
CNRM	C	-	-
	LR	+	+
CNRM	C	+	+
	HR	+	+
EC-Earth	C		
	LR	+	+
EC-Earth	C		
	HR	+	+
HadGEM3	C		
	LR	+	+
HadGEM3	C	+	
	HR	+	
MPI	C	+	+
	LR	-	
MPI	C		
	HR		

Table 4 Signs of the trends in ENSO variability as measured by the standard deviation of the Niño3.4 index (std(Niño3.4)) and the average power of the Continuous Wavelet Transform of the of the leading principal component of Tropical SST anomalies ( $\overline{CWT}$ ). The results that are significant at a  $\alpha=0.90$  level are shaded in yellow if they are positive and blue if they are negative. Results that are not significant are not shown and the cell is not shaded. Analysis is performed for all control (C) and transient (T) runs – see text for details.

We then show the center of frequency C(T) in Figure 26 from which we draw two main observations: (1) the center of ENSO frequency for a given model remains

consistent between control and transient runs, with the only exception of HadGEM HR where ENSO oscillates at slightly lower periodicities during the transient experiment; and (2) there are no ensemble-wide trends towards higher or lower periodicities as the external forcings increase. Finally, in Figure 27 we show  $S(T)$  and see how ENSO periodicity spreads around  $C(T)$  across the ensemble. In some cases, the periodicity of the signal is narrowly constrained around  $C(T)$  (e.g. CNMR LR transient) – indicative of a more oscillatory behaviour – and in other cases it is spread over a wider range (e.g. HadGEM HR control) – indicative of a more stochastic behaviour – and sometimes the system transitions between these two kinds of behaviour (e.g. CMCC HR control). Once again, we see signs of internal variability, but no ensemble-wide indication of a trend that predicts the system will move towards either a more stochastic and/or oscillatory behaviour. Given that previous results have shown enhanced TWC/NPMM-ENSO coupling leads to more stochastic ENSO variability (Pivotti and Anderson 2021; Pivotti et al.1 – in review), the lack of consistency in the transition of ENSO variability to either more or less stochastic (and hence less or more oscillatory) under the influence of increasing external forcings agrees with the earlier findings in Figure 24. To confirm this

result, we calculate the running 30-years correlation between (1) the time series we have used throughout the analysis to isolate ENSO – the leading principal component of Tropical SST anomalies ( $PC^1_{SST}$ ) – and (2) the time series we built to isolate TWC/NPMM – the first canonical variable of  $\tau_X$  ( $CV^1_{\tau_X}$ ). As above, we find no inter-model agreement regarding the presence of trends in the strength of TWC/NPMM-ENSO coupling under the influence of increasing external radiative forcing (not shown).

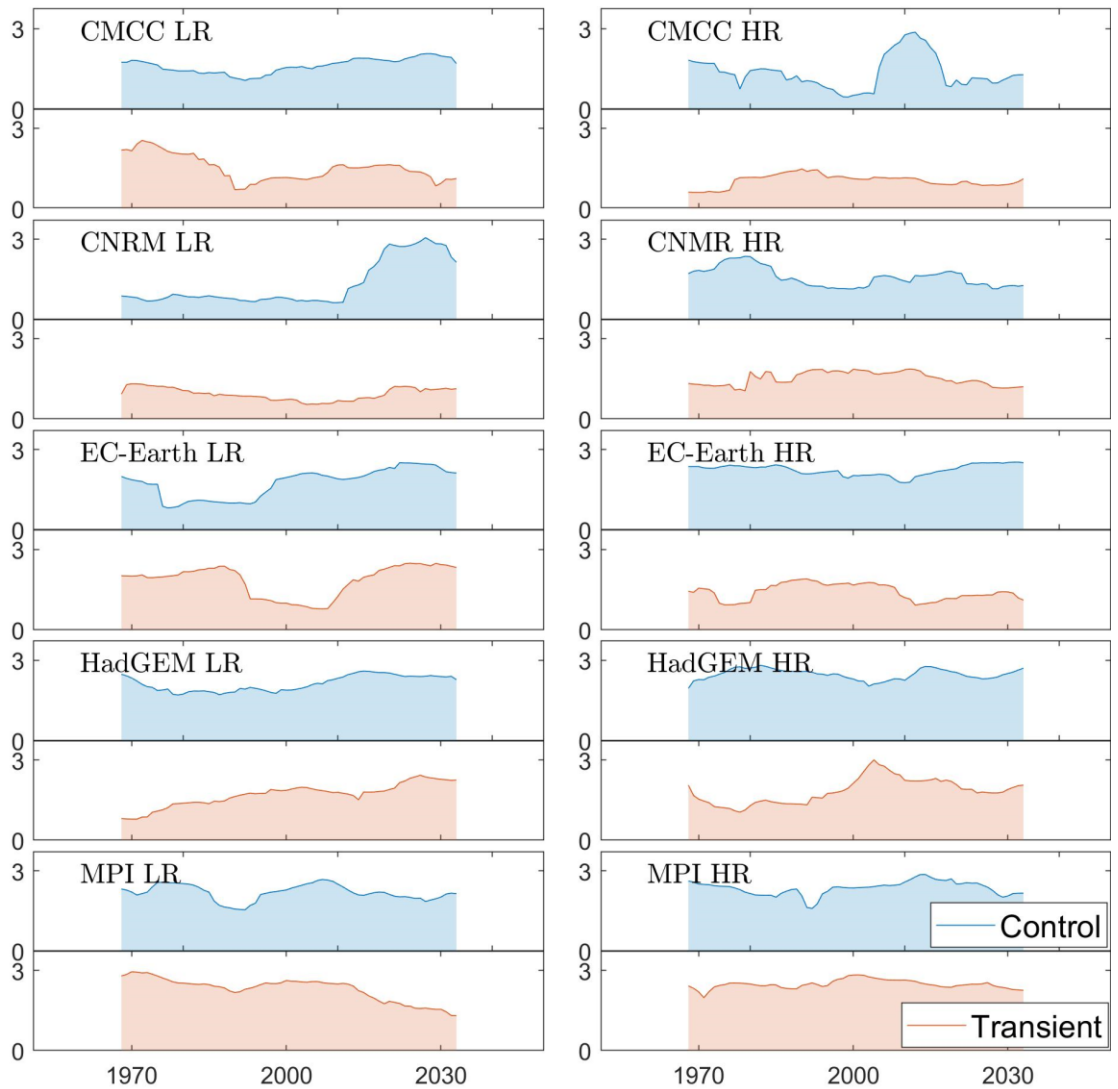


Figure 27 Same as Figure 25 except for the spread of periodicity  $S(t)$  of the Continuous Wavelet Transform (CWT) – see text for details.



## Summary and Conclusion

In this chapter, we study how the models participating in the HighResMIP protocol reconstruct the relationship between ENSO and its extra-tropical precursor TWC/NPMM.

In our spatial characterization of the reconstruction of the TWC/NPMM-ENSO relationship, we show that the ENSO events initiated by TWC/NPMM are consistently stronger and cover a larger area than average ENSO events, and that this relation holds true both with constant and increasing external forcings. As far as the area influenced by SST anomalies, we identified a projected increase in all ENSO events. This increase is accompanied by a subsequent westward shift of the center of heat, such that in the transient experiments the center of heat for average ENSO events aligns with the position of TWC/NPMM-related ones. At the same time, we see a lack of agreement on whether the relative amount of TWC-charged events – which represent on average the 30% of all ENSO events – is increasing or decreasing in the presence of increasing forcings.

Given the known relation between TWC/NPMM-ENSO variability and the oscillatory behavior of ENSO itself, we then study how the power of ENSO spreads across different periodicities. We find that the majority of models agree on an increase of the overall power of ENSO, which confirms our CHI analysis above. However, this power trend is not due to specific trends in how the ENSO system oscillates. In particular, we see no clear trends in the frequency of ENSO variability under warmer conditions; and, similarly, we see no clear trends towards more oscillatory or stochastic ENSO variability. Furthermore, this ensemble does not predict a shift in the strength of

the TWC/NPMM-ENSO relationship, which agrees with a previous results (Pivotti and Anderson 2021) that shows that these two features vary jointly over multi-decadal time-scales. The results further suggests that the strength of the TWC/NPMM-ENSO relationship changes as a result of internal variability in the system and not anthropogenic warming.

## CONCLUSION

In this thesis, I have investigated and unveiled different aspects of the relationship between ENSO and the TWC/NPMM driving mechanism. My first major contribution to its characterization is the correlation between the strength of the TWC/NPMM-ENSO relationship and the way in which ENSO oscillates. Specifically, when the relationship is strong, ENSO exhibits a stochastic behavior, while, when the relationship weakens, ENSO enters a regular oscillatory phase. In particular, historically, the TWC/NPMM-ENSO relationship has been strong during the last 60 years, and before 1920, but has faded in the intervening decades 1920-1960. The robustness of these results was tested on different reanalysis datasets. To further the investigation of this correlation, I turned to model simulations, and showed how the TWC/NPMM mechanism is a consistent precursor of ENSO across the ensemble, both with constant and increasing external forcings, albeit with some inter-model variations. On a subset of control experiments whose reconstruction of TWC/NPMM best approximated the results from the reanalyses, I was able to confirm that the connection between the TWC/NPMM-ENSO relationship and ENSO oscillatory behavior holds true in these state-of-the-art models.

These results, both in reanalyses and model simulations, refine earlier findings. Historically, they align with identified shifts in the frequency of the SO Index in the 1910's (Wang and Wang 1996) and 1960's (Wang and Wang 1996; Yiou, et al., 2000). As previously mentioned, ENSO can be interpreted either as a self-sustained oscillation, or as a mode triggered by stochastic forcing (Wang, et al., 2017). I show that there is a multi-decadal modulation in the way ENSO shifts between these two underlying

dynamics, that this modulation is connected to the influence of the TWC/NPMM, and that this feature can be found both in reanalysis data, as well as in coupled model simulations. This contribution confirms and frames within a broader perspective previous findings, like the ones from Yu and Fang (2018) and earlier results from Kirtman and Schopf (1998). In the first study, the authors show that the SF mechanism - equivalent to TWC/NPMM characterized here - is responsible for a stochastic evolution of the ENSO system, and identify in the interval 1958-2014 an enhanced influence of the TWC/NPMM upon ENSO (Yu and Fang 2018). In the second study, by running simulations on a simple coupled model the authors are able to show that an “undisturbed ENSO” oscillated regularly, while, when atmospheric noise is introduced in the system, ENSO behaves more stochastically and its main frequency changes (Kirtman and Schopf 1998).

These findings add a piece of the puzzle to further understand and characterize the dynamic of ENSO, and they contribute to an increased predictability of its events, which is one of the main motivations for this research project. In particular, as the system oscillated between these two behaviors, once ENSO enters a phase of self-sustained oscillation, its dynamic can be tracked within that framework and its predictability gets higher. A conclusion further supported by the study Yu and Fang (2018). Alternatively, as the system enters a stochastic phase, ENSO is strongly correlated to 1-year prior TWC/NPMM anomalies.

In addition to these results, since the institutions taking part in the HighResMIP ensemble ran experiments at varying horizontal resolutions, I showed that within this

ensemble, a change in horizontal resolution does not affect the ability to reconstruct the TWC/NPMM-ENSO relationship.

Finally, as I compared experiments with constant and increasing forcings, I found an ensemble-wide agreement on the system moving towards larger ENSO events, as well as a consistency in TWC/NPMM-related events being stronger than the average ones. Then, I analyzed whether the ensemble showed trends in the way ENSO oscillates, and I showed there is no inter-model agreement on whether the ENSO system is heading towards more oscillatory or stochastic behavior under the influence of increasing external forcing. Further, there is no inter-model agreement on whether the TWC/NPMM-ENSO relationship becomes more or less robust under the influence of increasing external forcing. This final result suggests that the TWC/NPMM-ENSO relationship, its strength and subsequent impact on ENSO oscillation are a result of internal multi-decadal modulation and not of anthropogenic forcings.

Over the course of my research, I have worked with two principle sets of variables – Sea Surface Temperature (SST), and horizontal wind stress ( $\tau_x$  and  $\tau_y$ ) – across numerous datasets, including both reanalyses and model experiments. Methodologically, the main tools I have utilized are the Canonical Correlation Analysis (CCA) in the basis of Principal Components (PC's) and the Continuous Wavelet Transform (CWT). The CCA in the basis of PC's was the tool I employed in repeated instances to isolate the time series (or identify the absence) of the modes of variability I focus on, namely ENSO and TWC/NPMM. Whereas, to study the oscillatory nature of the signals, I turned to the CWT, and tried different ways to interpret and present the

results. In particular, in the first analyses, the interpretations have been more visual-based, while in the fourth chapter I calculated three Center of Heat Index (CHI)-inspired indicators across the CWT matrices to quantitatively capture the kind of oscillatory behavior the signal showed.

Where do I intend to go from here? Following suggestions from reviewers as well as my personal interest, I intend to continue the investigation of the TWC/NPMM-ENSO relationship on larger CMIP6 model ensembles to gather a more telling image of how this connection is projected to evolve under increasingly warmer conditions. I am particularly interested in continuing the exploration of trends in oscillatory behavior of ENSO, as well as its relationship to the efficacy of the TWC/NPMM precursor. Along these lines, I would like to further utilize current and develop new methodologies to better isolate the shifts between stochastic and more oscillatory behaviors of the ENSO system, as well to better characterize the range of oscillatory ENSO behavior within model systems.

Over the longer term, my primary interest in ENSO as a climate mode is centered on its impact, more than on its mechanisms, therefore I intend to pursue research in this direction. I want to study both current and future ENSO teleconnections, its interactions with other climate modes and their combined impacts. As I have yet to work with these topics, this means I will need to learn new methodologies and datasets. These will of course be closely related to the ones I have been using during my PhD, making the transition challenging, but in my opinion feasible and rewarding. Furthermore, since much of the research around ENSO argues that the more we know about this climate mode, the better affected communities can prepare for its impacts, I want to dedicate time

assessing how well this communication is happening. For instance, in earlier stages of my research, I had started working on an assessment of early warning systems connected to ENSO impacts on extreme weather events as well as precipitation patterns in connection to agriculture. I would like to return to and finalize that project. After these initial assessments, I would like to join the endeavor of easing the fruition of research results on this specific topic from stakeholders and affected communities.

## BIBLIOGRAPHY

- Alexander, Michael A., Ileana Bladé, Matthew Newman, John R. Lanzante, Ngar-Cheung Lau, and James D. Scott. 2002. "The Atmospheric Bridge: The Influence of ENSO Teleconnections on Air–Sea Interaction over the Global Oceans." *Journal of Climate* 15: 2205-2231. doi:10.1175/1520-0442(2002)015<2205:TABTIO>2.0.CO;2.
- Alexander, Michael A., Ileana Bladé, Matthew Newman, John R. Lanzante, Ngar-Cheung Lau, and James D. Scott. 2002. "The Atmospheric Bridge: The Influence of ENSO Teleconnections on Air–Sea Interaction over the Global Oceans." *Journal of Climate* 2205-2231.
- Amaya, Dillon J. 2019. "The Pacific Meridional Mode and ENSO: a Review." *Current Climate Change Reports* 5: 296–307. doi:10.1007/s40641-019-00142-x.
- Amaya, Dillon J., Yu Kosaka, Wenyu Zhou, Yu Zhang, Shang-Ping Xie, and Arthur J. Miller. 2019. "The North Pacific Pacemaker Effect on Historical ENSO and Its Mechanisms." *Journal of Climate* 32: 7643-7661. doi:10.1175/JCLI-D-19-0040.1.
- Anderson, Bruce T. 2003. "Tropical Pacific sea-surface temperatures and preceding sea level pressure anomalies in the subtropical North Pacific." *Journal of Geophysical Research: Atmospheres* 108. doi:10.1029/2003JD003805.
- Anderson, Bruce T. 2003. "Tropical Pacific sea-surface temperatures and preceding sea level pressure anomalies in the subtropical North Pacific." *Journal of Geophysical Research: Atmospheres*.
- Anderson, Bruce T., and Renellys C. Perez. 2015. "ENSO and non-ENSO induced charging and discharging." *Climate Dynamics* 45: 2309–2327. doi:10.1007/s00382-015-2472-x.
- Anderson, Bruce T., and Renellys C. Perez. 2015. "ENSO and non-ENSO induced charging and discharging." *Climate Dynamics* 45: 2309–2327.
- Anderson, Bruce T., Renellys C. Perez, and Alicia Karspeck. 2013. "Triggering of El Niño onset through trade wind–induced charging of the equatorial Pacific." *Geophysical Research Letters* 40: 1212-1216. doi:10.1002/grl.50200.
- Ashok, Karumuri, Zhaoyong Guan, N. H. Saji, and Toshio Yamagata. 2004. "Individual and Combined Influences of ENSO and the Indian Ocean Dipole on the Indian



Summer Monsoon." *Journal of Climate* 17: 3141-3155. doi:10.1175/1520-0442(2004)017<3141:IACIOE>2.0.CO;2.

Bellenger, H., E. Guilyardi, J. Leloup, M. Lengaigne, and J. Vialard. 2014. "ENSO representation in climate models: from CMIP3 to CMIP5." *Climate Dynamics* 42: 1999–2018. doi:10.1007/s00382-013-1783-z.

Bretherton, Christopher S., Catherine Smith, and John M. Wallace. 1992. "An Intercomparison of Methods for Finding Coupled Patterns in Climate Data." *Journal of Climate* 5: 541-560. doi:10.1175/1520-0442(1992)005<0541:AIOMFF>2.0.CO;2.

Bretherton, Christopher S., Catherine Smith, and John M. Wallace. 1992. "An Intercomparison of Methods for Finding Coupled Patterns in Climate Data." *Journal of Climate* 541-560.

Cai, Wenju, Agus Santoso, Guojian Wang, Sang-Wook Yeh, Soon-Il An, Kim M. Cobb, Mat Collins, et al. 2015. "ENSO and greenhouse warming." *Nature Climate Change* 849–859.

Cai, Wenju, Peter van Rensch, Tim Cowan, and Harry H. Hendon. 2011. "Teleconnection Pathways of ENSO and the IOD and the Mechanisms for Impacts on Australian Rainfall." *Journal of Climate* 24: 3910-3923. doi:10.1175/2011JCLI4129.1.

Chakravorty, Soumi, Renellys C. Perez, Bruce T. Anderson, Benjamin S. Giese, Sarah M. Larson, and Valentina Pivotti. 2020. "Testing the trade wind charging mechanism and its influence on ENSO variability." *Journal of Climate*. doi:10.1175/JCLI-D-19-0727.1.

Chen, Shangfeng, Wen Chen, and Bin Yu. 2014. "Asymmetric influence of boreal spring Arctic Oscillation on subsequent ENSO." *Journal of Geophysical Research: Atmospheres* 119: 11,135 -11,150. doi:10.1002/2014JD021831.

Chen, Shangfeng, Wen Chen, Renguang Wu, Bin Yu, and Hans-F Graf. 2020. "Potential Impact of Preceding Aleutian Low Variation on El Niño–Southern Oscillation during the Following Winter." *Journal of Climate* 33: 3061-3077. doi:10.1175/JCLI-D-19-0717.1.

Collins, Mat, Soon-Il An, Wenju Cai, Alexandre Ganachaud, Eric Guilyardi, Fei-Fei Jin, Markus Jochum, Matthieu Lengaigne, and et al. 2010. "The impact of global warming on the tropical Pacific Ocean and El Niño." *Nature Geoscience* 391-397. doi:10.1038/ngeo868.

- Dai, Aiguo, and T. M. L. Wigley. 2000. "Global patterns of ENSO-induced precipitation." *Geophysical Research Letters* 27: 1283-1286. doi:10.1029/1999GL011140.
- Dai, Aiguo, and T. M. L. Wigley. 2000. "Global patterns of ENSO-induced precipitation." *Geophysical Research Letters* 1283-1286.
- EC-Earth Consortium. 2019. "EC-Earth-Consortium EC-Earth3P model output prepared for CMIP6 HighResMIP control-1950." Earth System Grid Federation. doi:10.22033/ESGF/CMIP6.4547.
- . 2018. "EC-Earth-Consortium EC-Earth3P-HR model output prepared for CMIP6 HighResMIP control-1950." Earth System Grid Federation. doi:10.22033/ESGF/CMIP6.4548.
- Eyring, V., S. Bony, G. A. Meehl, C. A. Senior, B. Stevens, R. J. Stouffer, and K. E. Taylor. 2016. "Overview of the Coupled Model Intercomparison Project Phase 6 (CMIP6)." *Geoscientific Model Development* 9: 1937-1958. doi:10.5194/gmd-9-1937-2016.
- Feng, Juan, Wen Chen, and Yanjie Li. 2017. "Asymmetry of the winter extra-tropical teleconnections in the Northern Hemisphere associated with two types of ENSO." *Climate Dynamics* 2135-2151.
- Giese, Benjamin S., and Sulagna Ray. 2011. "El Niño variability in simple ocean data assimilation (SODA), 1871–2008." *Journal of Geophysical Research: Oceans*.
- Giese, Benjamin S., Howard F. Seidel, Gilbert P. Compo, and Prashant D. Sardeshmukh. 2016. "An ensemble of ocean reanalyses for 1815–2013 with sparse observational input." *Journal of Geophysical Research: Oceans* 121: 6891-6910. doi:10.1002/2016JC012079. .
- Graham, Nicholas E., Joel Michaelsen, and Tim P. Barnett. 1987. "An investigation of the El Niño-Southern Oscillation cycle With statistical models: 1. Predictor field characteristics." *Journal of Geophysical Research: Oceans* 92: 14251-14270. doi:10.1029/JC092iC13p14251.
- Haarsma, R. J., M. J. Roberts, P. L. Vidale, C. A. Senior, A. Bellucci, Q. Bao, P. Chang, and S. et al. Corti. 2016. "High Resolution Model Intercomparison Project (HighResMIP v1.0) for CMIP6." *Geoscientific Model Development* 9: 4185-4208. doi:10.5194/gmd-9-4185-2016.

- Hendon, Harry H., and Matthew C. and Zhang, Chidong Wheeler. 2007. "Seasonal Dependence of the MJO-ENSO Relationship." *Journal of Climate* 20: 531-543. doi:10.1175/JCLI4003.1.
- Jin, Fei-Fei. 1997. "An Equatorial Ocean Recharge Paradigm for ENSO. Part I: Conceptual Model." *Journal of the Atmospheric Sciences* 54: 811-829. doi:10.1175/1520-0469(1997)054<0811:AEORPF>2.0.CO;2.
- Kapur, Atul, and Chidong Zhang. 2012. "Multiplicative MJO Forcing of ENSO." *Journal of Climate* 25: 8132-8147. doi:10.1175/JCLI-D-11-00609.1.
- Kirtman, Ben P., and Paul S. Schopf. 1998. "Decadal variability in ENSO predictability and prediction." *Journal of Climate* 11: 2804-2822. doi:10.1175/1520-0442(1998)011<2804:DVIEPA>2.0.CO;2.
- Larson, Sarah M., and Ben P. Kirtman. 2014. "The Pacific Meridional Mode as an ENSO Precursor and Predictor in the North American Multimodel Ensemble." *Journal of Climate* 7018-7032.
- Larson, Sarah, and Ben Kirtman. 2013. "The Pacific Meridional Mode as a trigger for ENSO in a high-resolution coupled model." *Geophysical Research Letters* 40: 3189-3194. doi:10.1002/grl.50571.
- Lian, Tao, Dake Chen, and Youmin and Wu, Qiaoyan Tang. 2014. "Effects of westerly wind bursts on El Niño: A new perspective." *Geophysical Research Letters* 41: 3522-3527. doi:10.1002/2014GL059989.
- Liu, Bo, Guijie Zhao, Gang Huang, Pengfei Wang, and Bangliang Yan. 2018. "The dependence on atmospheric resolution of ENSO and related East Asian-western North Pacific summer climate variability in a coupled model." *Theoretical and Applied Climatology* 133: 1207-1217. doi:10.1007/s00704-017-2254-y.
- Liu, Fei, Tim Li, Hui Wang, Li Deng, and Yuanwen Zhang. 2016. "Modulation of Boreal Summer Intraseasonal Oscillations over the Western North Pacific by ENSO." *Journal of Climate* 29. doi:10.1175/JCLI-D-15-0831.1.
- Liu, Zhengyu, and Shangping Xie. 1994. "Equatorward Propagation of Coupled Air-Sea Disturbances with Application to the Annual Cycle of the Eastern Tropical Pacific." *Journal of the Atmospheric Sciences* 51: 3807-3822. doi:10.1175/1520-0469(1994)051<3807:EPOCAD>2.0.CO;2.

- Myhre, G., D. Shindell, F.-M. Bréon, W. Collins, J. Fuglestedt, J. Huang, D Koch, J.-F. Lamarque, and et al. 2013. *Anthropogenic and Natural Radiative Forcing*. Climate Change 2013: The Physical Science Basis. Contribution of Working Group I to the Fifth Assessment Report of the Intergovernmental Panel on Climate Change, Cambridge, United Kingdom and New York, NY, USA: Cambridge University Pre.
- Pachauri, Rajendra K., and Myles R. et al. Alle. 2014. "Climate Change 2014: Synthesis Report. Contribution of Working Groups I, II and III to the Fifth Assessment Report of the Intergovernmental Panel on Climate Change." IPCC, Geneva, Switzerland, 151.
- Pegion, Kathy V., and Christopher Selman. 2017. "Extratropical precursors of the El Niño–southern oscillation." In *Climate Extremes: Patterns and Mechanisms*, by S.-Y. Simon Wang, Jin-Ho Yoon, Christopher C. Funk and Robert R. Gillies. Wiley.
- Picaut, Joël, François Masia, and Yves du Penhoat. 1997. "An Advective-Reflective Conceptual Model for the Oscillatory Nature of the ENSO." *Science* 277: 663-666. doi:10.1126/science.277.5326.663.
- Pivotti, Valentina, and Bruce T. Anderson. 2021. "Transition between Forced and Oscillatory ENSO Behavior over the last Century." *JGR Atmospheres*. doi:10.1029/2020JD034116.
- Planton, Yann Y., Eric Guilyardi, Andrew T. Wittenberg, Jiwoo Lee, Peter J. Gleckler, Tobias Bayr, Shayne McGregor, et al. 2021. "Evaluating Climate Models with the CLIVAR 2020 ENSO Metrics Package." *Bulletin of the American Meteorological Society* E193–E217. doi:10.1175/BAMS-D-19-0337.1.
- Puy, M., J. Vialard, M. Lengaigne, E. Guilyardi, A. Voldoire, and G. Madec. 2019. "Modulation of equatorial Pacific sea surface temperature response to Westerly Wind Events by the oceanic background state." *Climate Dynamics* 52: 7267-7291. doi:10.1007/s00382-016-3480-1.
- Rasmusson, Eugene M., and Thomas H. Carpenter. 1982. "Variations in Tropical Sea Surface Temperature and Surface Wind Fields Associated with the Southern Oscillation/El Niño." *Monthly Weather Review* 354-384.
- Riahi, Keywan, Shilpa Rao, Volker Krey, Cheolhung Cho, Vadim Chirkov, Guenther Fischer, Georg Kindermann, Nebojsa Nakicenovic, and Peter Rafaj. 2011. "RCP8.5-A scenario of comparatively high greenhouse gas emissions." *Climatic Change* 33. doi:10.1007/s10584-011-0149-y.

- Roberts, Christopher David, Retish Senan, Franco Molteni, Souhail Boussetta, and Sarah Keeley. 2017. "ECMWF ECMWF-IFS-HR model output prepared for CMIP6 HighResMIP control-1950." Earth System Grid Federation. doi:10.22033/ESGF/CMIP6.4945.
- . 2018. "ECMWF ECMWF-IFS-LR model output prepared for CMIP6 HighResMIP control-1950." Earth System Grid Federation. doi:10.22033/ESGF/CMIP6.4946.
- . 2018. "ECMWF ECMWF-IFS-MR model output prepared for CMIP6 HighResMIP control-1950." Earth System Grid Federation. doi:10.22033/ESGF/CMIP6.4947.
- Roberts, Malcolm J., Laura C. Jackson, Christopher D. Roberts, Virna Meccia, Davi Docquier, Torben Koenigk, Pablo Ortega, and Eduardo et al. Moreno-Chamarro. 2020. "Sensitivity of the Atlantic Meridional Overturning Circulation to Model Resolution in CMIP6 HighResMIP Simulations and Implications for Future Changes." *Journal of Advances in Modeling Earth Systems* 12. doi:10.1029/2019MS002014.
- Roberts, Malcolm John, Joanne Camp, Jon Seddon, Pier Luigi Vidale, Kevin Hodges, Benoit Vanniere, Jenny Mecking, and Rein et al. Haarsma. 2020. "Impact of Model Resolution on Tropical Cyclone Simulation Using the HighResMIP-PRIMAVERA Multimodel Ensemble." *Journal of Climate* 33: 2557-2583. doi:10.1175/JCLI-D-19-0639.1.
- Roberts, Malcolm. 2017. "MOHC HadGEM3-GC31-HM model output prepared for CMIP6 HighResMIP." Earth System Grid Federation. doi:10.22033/ESGF/CMIP6.446.
- . 2017. "MOHC HadGEM3-GC31-LL model output prepared for CMIP6 HighResMIP." Earth System Grid Federation. doi:10.22033/ESGF/CMIP6.1901.
- Santoso, Agus, Michael J. Mcphaden, and Wenju Cai. 2017. "The Defining Characteristics of ENSO Extremes and the Strong 2015/2016 El Niño." *Reviews of Geophysics* 1079-1129. doi:10.1002/2017RG000560.
- Scoccimarro, Enrico, Alessio Bellucci, and Daniele Peano. 2018. "CMCC CMCC-CM2-HR4 model output prepared for CMIP6 HighResMIP control-1950." Earth System Grid Federation. doi:10.22033/ESGF/CMIP6.3748.

- . 2018. "CMCC CMCC-CM2-VHR4 model output prepared for CMIP6 HighResMIP control-1950." Earth System Grid Federation.  
doi:10.22033/ESGF/CMIP6.3749.
- Small, R. Justin, Frank Bryan, Stuart Bishop, Larson Sarah, and Tomas Robert A. 2020. "What Drives Upper-Ocean Temperature Variability in Coupled Climate." *Journal of Climate* 577–596 . doi:10.1175/JCLI-D-19-0295.1.
- Suarez, Max J., and Paul S. Schopf. 1988. "A Delayed Action Oscillator for ENSO." *Journal of the Atmospheric Sciences* 45: 3283-3287. doi:10.1175/1520-0469(1988)045<3283:ADAOFE>2.0.CO;2.
- Tang, Youmin, and Bin Yu. 2008. "MJO and its relationship to ENSO." *Journal of Geophysical Research: Atmospheres* 113. doi:10.1029/2007JD009230.
- Taschetto, Andréa S., Caroline C. Ummenhofer, Malte F. Stuecker, Dietmar Dommenges, Karumuri Ashok, Regina R. Rodrigues, and Sang-Wook Yeh. 2020. "ENSO Atmospheric Teleconnections." In *El Niño Southern Oscillation in a Changing Climate*, 309-335. doi:10.1002/9781119548164.ch14.
- Taylor, Karl E. 2001. "Summarizing multiple aspects of model performance in a single diagram." *Journal of Geophysical Research* 106: 7183-7192.  
doi:10.1029/2000JD900719.
- Trenberth, Kevin E. 1997. "The Definition of El Niño." *Bulletin of the American Meteorological Society* 78: 2771-2778.
- Ummenhofer, Caroline C., Franziska U. Schwarzkopf, Gary Meyers, Erik Behrens, and Arne and Böning, Claus W. Biastoch. 2012. "Pacific Ocean Contribution to the Asymmetry in Eastern Indian Ocean Variability." *Journal of Climate* 26: 1152-1171. doi:10.1175/JCLI-D-11-00673.1.
- Voldoire, Aurore. 2019. "CNRM-CERFACS CNRM-CM6-1 model output prepared for CMIP6 HighResMIP control-1950." System Grid Federation.  
doi:10.22033/ESGF/CMIP6.3946.
- . 2019. "CNRM-CERFACS CNRM-CM6-1-HR model output prepared for CMIP6 HighResMIP control-1950." Earth System Grid Federation.  
doi:10.22033/ESGF/CMIP6.3947.
- von Storch, Jin-Song, Dian Putrasahan, Katja Lohmann, Oliver Gutjahr, Johann Jungclaus, Matthias Bittner, Helmuth Haak, and Karl-Hermann et al. Wieners. 2018. "MPI-M MPI-ESM1.2-HR model output prepared for CMIP6

HighResMIP control-1950." Earth System Grid Federation.  
doi:10.22033/ESGF/CMIP6.6485.

- von Storch, Jin-Song, Dian Putrasahan, Katja Lohmann, Oliver Gutjahr, Johann Jungclaus, Matthias Bittner, Helmuth Haak, and Karl-Hermann Wieners. 2018. "MPI-M MPI-ESM1.2-XR model output prepared for CMIP6 HighResMIP control-1950." Earth System Grid Federation.  
doi:10.22033/ESGF/CMIP6.10295.
- Wang, Bin, and Yan Wang. 1996. "Temporal Structure of the Southern Oscillation as Revealed by Waveform and Wavelet Analysis." *Journal of Climate* 9: 1586-1598. doi:10.1175/1520-0442(1996)009<1586:TSOTSO>2.0.CO;2.
- Wang, Chunzai. 2001. "A Unified Oscillator Model for the El Niño–Southern Oscillation." *Journal of Climate* 14: 98-115. doi:10.1175/1520-0442(2001)014<0098:AUOMFT>2.0.CO;2.
- Wang, Chunzai, Clara Deser, Jin-Yi Yu, Pedro N. DiNezio, and Amy Clement. 2017. *El Niño and Southern Oscillation (ENSO): A Review*. Vol. 8, in *Coral Reefs of the Eastern Tropical Pacific: Persistence and Loss in a Dynamic Environment*, 85-106. doi:10.1007/978-94-017-7499-4\_4.
- Weisberg, Robert H., and Chunzai Wang. 1997. "A Western Pacific Oscillator Paradigm for the El Niño-Southern Oscillation." *Geophysical Research Letters* 24: 779-782. doi:10.1029/97GL00689.
- Wengel, Christian, Sun-Seon Lee, Malte F. Stuecker, Axel Timmermann, Jung-Eun Chu, and Fabian Schloesser. 2021. "Future high-resolution El Niño/Southern Oscillation dynamics." *Nature Climate Change* 758-765.
- Wengel, Christian, Sun-Seon Lee, Malte F. Stuecker, Axel Timmermann, Jung-Eun Chu, and Fabian Schloesser. 2021. "Future high-resolution El Niño/Southern Oscillation dynamics." *Nature Climate Change* 11: 758-765.  
doi:10.1038/s41558-021-01132-4.
- Zuidema, Paquita, Ping Chang, Brian Medeiros, Ben P. Kirtman, Roberto Mechoso, Edwin K. Schneider, Thomas Toniazzo, Ingo Richter, and et al. 2016. "Challenges and Prospects for Reducing Coupled Climate Model SST Biases in the Eastern Tropical Atlantic and Pacific Oceans: The U.S. CLIVAR Eastern Tropical Oceans Synthesis Working Group." *Bulletin of the American Meteorological Society* 2305–2328 .

**CURRICULUM VITAE**

